

NAG5-740
IN-46 CR
49609
1568.

MECHANICS OF SHEAR RUPTURE
APPLIED TO EARTHQUAKE ZONES

by

Victor C. Li

Department of Civil Engineering
Massachusetts Institute of Technology
Cambridge, MA 02139

To appear in

Rock Fracture Mechanics
B. Atkinson, Editor
Academic Press Inc.
1986

V.2 May, 1986

(NASA-CR-180070) MECHANICS OF SHEAR RUPTURE
APPLIED TO EARTHQUAKE ZONES (Massachusetts
Inst. of Tech.) 156 p

CSCI 08K

N87-15663

Unclas
40349

G3/46

TABLE OF CONTENTS

I.	INTRODUCTION	4
II.	SHEAR FRACTURE MECHANICS	9
2.1	Elastic Brittle Crack Mechanics	12
2.1.1	Asymptotic Crack Tip Stress Field	12
2.1.2	Energy Release Rate G	17
2.2	The J-Integral	22
III.	SLIP-WEAKENING MODEL OF SHEAR RUPTURE	27
3.1	Slip-weakening Constitutive Model	29
3.2	Stability Analysis of a Single-Degree-of-Freedom System ..	31
3.2.1	Sliding of a Spring-Block/Spring-Dashpot-Block System	31
3.2.2	Application to Fault Stability Analysis	36
3.3	Slip-weakening Model, J-integral and Elastic brittle crack model	42
3.3.1	Relationship Between the Energy Release Rate G and the Slip-Weakening Model Parameters	44
3.3.2	Estimating the Breakdown Zone Size	47
3.3.3	Crustal Scale Applications	49
3.4	Laboratory and Field Estimates of Shear Fracture Parameters in Rocks	52
3.4.1	Laboratory Estimates of Shear Fracture Parameters ..	52
3.4.2	Field Estimates of Shear Fracture Parameters	56
3.4.3	Variations in Fracture Parameters	60
IV.	SLIP DISTRIBUTIONS AND INTERACTIONS	62
4.1	Integral Representation and Physical Interpretations ..	63
4.2	Structure of Green's Functions	69
4.3	Applications to Dip-slip Faulting	75
4.4	Application to Slip-stress Interaction along an Inhomogeneous Fault	79
V.	CONCLUSIONS	87
VI.	ACKNOWLEDGEMENTS	89

VII. REFERENCES	91
TABLE CAPTIONS	101
FIGURE CAPTIONS	102
TABLES	110
FIGURES	123

INTRODUCTION

This chapter reviews the mechanics of shear slippage and rupture in rock masses. The physical problem often arises because of the presence of a plane or thin zone of weakness - sometimes a joint or a fault - in a body under applied load. Discussion of the formation of such a plane of weakness is not within the scope of this article. Rather we shall focus on the slip response under increasing gross shear load transmitted across a pre-existing weak plane. The slip response may be stable initially, then becomes unstable, leading to a dynamic shear rupture at higher applied loads. When the slip distribution is very non-uniform with slip confined to a finite segment of the plane of weakness, a Griffith crack type failure may result. In contrast, the whole plane may cut through the body and slip occurs more or less uniformly. The former type of crack failure is usually described by fracture mechanics, and the latter by classical strength theory. A more general concept, known as the slip-weakening model (and tension-softening model in the corresponding tensile failure mode) recognizes the elastic brittle crack description and the simple strength description as limiting cases. The connection between these concepts forms a major focus of this review article.

While the applications and examples chosen to illustrate the theories presented are heavily slanted towards earthquake faults, the concepts are equally valid and applicable in many other fields

of research, such as in geotechnical engineering where failure of jointed rock masses or failure in overconsolidated clay slopes are of major concern. The relevance of the mechanics of slip rupture to understanding the physics of the earthquake source process is obvious. For an appreciation of the physical context of slip rupture representation of earthquakes, the reader is referred to the text (especially Chapter 7) by Kasahara (1981) on the relation between tectonics and earthquakes.

Elastic dislocation theory has proved to be very useful in describing displacement discontinuities (slip) in otherwise continuous bodies. A convenient way of thinking about a dislocation is to imagine a planar cut in a body. The two faces of this cut are slid uniformly and then are glued back together. This operation introduces dislocation stress and displacement fields in the body. A non-uniform slip distribution can be constructed by putting a number of such dislocations at logistic locations, and the resulting stress and displacement fields are obtained by superimposing the stress and displacement fields of each discrete dislocation. This construction is sometimes referred to as a continuously distributed or smeared dislocation. Geophysicists have taken advantage of such a procedure to estimate the seismic slip distributions on earthquake faults by inverting the measured displacement field on the ground surface (see, e.g. Chinnery, 1961, 1970; Savage and Hastie, 1966; Walsh, 1969 and Rybicki, 1986). More recently, post-seismic leveling measurements

have also been used to estimate rheological properties based on dislocation displacement fields derived from layered elastic/viscoelastic half-space models (see, e.g. Thatcher et al, 1980). Such kinematic models occupy an important place in using measurable quantities of surface deformation to deduce (directly) unmeasurable quantities of fault slip and material properties of the earth. However, a shortcoming of kinematic modelling is that it provides limited insight into the physical processes leading to an instability. Such insights are important, for example, to forecast an earthquake rupture, since it would provide a rational basis to interpret seismic (such as foreshocks) and aseismic (such as surface displacement rate and strain rate changes) precursory signals. The study of non-kinematic models of slip rupture, of which elastic brittle crack theory is a special case, is another major theme in this article.

To reach beyond kinematic modelling, it is necessary to prescribe some kind of constitutive law which relates fault slip to stress. In order for a seismic event to radiate energy from the source, the stress is expected to drop with increasing slip. This implies that natural faults can be described by a slip-weakening model. In the laboratory slip-weakening behavior is directly observable in a variety of specimens, including overconsolidated clay samples, and in intact, sawcut and jointed rock specimens. Extrapolations of material parameters obtained from the laboratory to the real Earth has always been a difficult

task, and those related to the slip-weakening model are no exception. Even so, some recent non-kinematic models (e.g. Stuart, et al 1985) have generated results consistent with available geodetic data covering a period of time. Moreover, such models project into the future how slip continues to develop until instability.

This article is organized in three sections. The first deals with a summary of essential ideas in fracture mechanics, emphasizing the interpretation and relation among the fracture parameters K , G and J in shear cracks. This section is concise because of the widely available literature on this subject and several recent review articles on their applications to geophysical problems (Rudnicki, 1980; Rice, 1980; Dmowska and Rice, 1986). The second section describes the slip-weakening model. The physical interpretation of the slip-weakening model and connections to G and J are emphasized. The model is used to illustrate the loss of stability of a simple slip system. This section also summarizes fracture resistance properties deduced from laboratory tests and from observations of earthquake faulting. The third and last section deals with the general formulation of the problem of non-uniform slip distribution in a continuum. There are two focuses in the section: the structure of the stress transmission Green's function which incorporates information about the rheology (elasticity, viscoelasticity, and poro-elasticity) and geometry of the continuum containing the slip

plane; and the formulation of non-kinematic problems. Several examples from recent geophysical literature are discussed.

The coverage in this article is necessarily incomplete, even as far as the mechanics of shear rupture applied to earthquake faults is concerned. For example, the dynamic rupture process important to seismology is not included. Excellent review of this subject could be found in Dmowska and Rice (1986), and in the text by Aki and Richards (1980) on quantitative seismology. With few exceptions, most of our discussions will focus on 2-D problems. This should not be construed as an indication that shear rupture problems are inherently 2-D, although in many circumstances they could be approximated as such. In section 4, we do describe a line-spring procedure which reduces a 3-D problem into a 2-D one. Within limitations, such a technique appears to be quite powerful and provides a computationally economical alternative to solving full-scale 3-D fault problems.

Apart from the references mentioned above, the reader will find the following publications of particular interest: Journal of Geophysical Research special issue on Fault Mechanics and its Relation to Earthquake Prediction (Vol 84, May, 1979), Pure and Applied Geophysics special issue on Earthquake Prediction (Vol 122, No. 6, 1984/5), and an American Geophysical Union publication Earthquake Source Mechanics published for the 5th Maurice Ewing Symposium (1986).

II SHEAR FRACTURE MECHANICS

In contrast to applications to technological materials which deal mostly with tensile fracture, application of fracture mechanics to the earth's crust involves mainly shear cracks. This is due to a number of reasons, notably the presence of lithostatic pressure which reduces the tendency of tensile cracking on a large scale. Repeated ruptures on the same plane also prevents fracture propagation from deviating markedly from the pre-existing weakened fault plane. Pre-existing fault zones must act as guides to shear rupture since without such a weakened plane, shear cracks in brittle laboratory specimens often tend to develop kinking or wing cracks from the ends of a shear sliding plane. While tensile cracking is not usually seen on a scale of tens or hundreds of km, it can still form on a more local scale, sometimes in the form of en-echelon tensile cracks which are joined together by the through-running main shear rupture. As an example, soil cracking at an angle to the main rupture was observed in the 1966 Parkfield earthquake (Allen and Smith, 1966). Recent work on compression failure of brittle material by Nemat-Nasser and Horii (1982) and Ashby and Hallam (1986) may shed some light on this phenomenon. However, our focus in this article will be on a much larger scale than that of the en-echelon tensile cracks.

In general, there is not much difference between the analysis of shear and tensile cracks. Two points which play an important role in understanding earthquake ruptures, however, should be

noted. The first is that unlike tensile cracks, shear crack faces are not stress-free even if the surfaces have been well slid. However, the residual frictional resistance may be regarded as a reference stress level, as will be explained further in section 2.1. In any case it is useful to keep in mind that the frictional work acts as an additional energy sink, reducing the amount of energy available to drive the crack tip. The other characteristic in shear cracks is that the fracture energy release rate, at least for laboratory rocks, is often two orders of magnitude higher than that for tensile cracks (Wong, 1982a). This is presumably related to the difference in the physical break-down processes at the crack tip of a shear and a tensile crack. The shear breakdown process may involve the extension and linking of smaller scale en-echelon tensile cracks as described earlier. Laboratory measurements of the critical energy release rates in rocks must therefore be made in the fracture mode appropriate to the field conditions, although we shall see in section 3 that even this does not fully account for the discrepancy between measured magnitudes in the laboratory and magnitudes estimated from field observations. Other than the differences pointed out above, the analysis of shear and tensile cracks are rather similar. In the rest of this article, the discussions will focus mainly on shear cracks.

Two well-known approaches have been used in the study of elastic brittle cracks. The first is based on the work of Irwin

(1960) who characterized the intensity of the crack tip stress field by a stress intensity factor K_i ($i = I, II, III$ denoting the 3 modes of deformation). It is hypothesized that when K_i reaches a certain value, K_{ic} , crack extension occurs. This fracture criterion $K_i = K_{ic}$ represents a balance of the crack driving stress intensity with a critical stress intensity (fracture toughness) that the material can sustain. The second approach is an extension of the idea of Griffith (1920) by characterizing fracture as a balance between available energy G to drive the crack and the energy absorbed by the inelastic-breakdown processes of the material at the crack tip G_c . This fracture criterion $G = G_c$ may be shown to be consistent with $K_i = K_{ic}$ quasistatic crack propagation analysis in a linear elastic body. These single-parameter fracture characterizations are analogous to the classical strength concept which relates the shear stress σ to the shear strength σ_t at failure of a specimen deforming uniformly. There is, however, a major difference between fracture mechanics and the strength concept: The strength concept in general cannot characterize objectively the crack driving force and therefore fails to predict the load level a structure with flaws can carry. In section 3, it will be seen that the strength concept and brittle elastic crack mechanics may be regarded as two opposite limiting conditions of a more general slip-weakening model.

In the following, we shall summarize the essentials of

elastic brittle crack mechanics with particular focus on the relationships between the various fracture parameters K , G and the path-independent J -integral. The J -integral extends the realm of linear elastic fracture mechanics (LEFM) to situations where the small scale yielding condition (to be explained) of LEFM is violated.

2.1 Elastic Brittle Crack Mechanics

2.1.1 Asymptotic Crack Tip Stress Field: Near a sharp crack such as that shown in Fig. 1, the stress field based on a linear elastic analysis may be expressed in the asymptotic form (see, e.g., Rice, 1968a).

For mode II deformation,

$$\sigma_{12} = K_{II} (2\pi r)^{-1/2} \cos(\theta/2) [1 - \sin(\theta/2) \sin(3\theta/2)] + \sigma^f + o(r^{1/2})$$

$$\sigma_{22} = K_{II} (2\pi r)^{-1/2} \sin(\theta/2) \cos(3\theta/2) + \sigma_n + o(r^{1/2}) \quad (1a)$$

$$\sigma_{11} = K_{II} (2\pi r)^{-1/2} \sin(\theta/2) [2 + \cos(\theta/2) \cos(3\theta/2)] + o(1)$$

and the near tip crack face shear slip (for plane strain) is given by

$$\delta_1 = u_1^+ - u_1^- = \frac{(1 - \nu)}{\mu} K_{II} (8r/\pi)^{1/2} + o(r^{3/2}) \quad (1b)$$

where u_1^+ and u_1^- are the displacements in the x_1 direction for the

upper and lower crack faces, and μ and ν are the shear modulus and Poisson's ratio respectively. For plane stress deformation, the factor $(1-\nu)$ should be replaced by $1/(1+\nu)$.

For mode III deformation,

$$\begin{aligned}\sigma_{13} &= -K_{III} (2\pi r)^{-1/2} \sin(\theta/2) + o(1) \\ \sigma_{23} &= K_{III} (2\pi r)^{-1/2} \cos(\theta/2) + \sigma^f + o(r^{1/2})\end{aligned}\quad (2a)$$

and the near tip crack face shear slip is given by

$$\delta_3 = u_3^+ - u_3^- = (K_{III}/\mu) (8r/\pi)^{1/2} + o(r^{3/2}) \quad (2b)$$

The first terms in the stress expressions are $1/\sqrt{r}$ singular, dominating the behavior of the stress field near the crack tip, with singularity strength given by the stress intensity factor K . (For brevity, K will stand for K_{II} and K_{III} and δ will stand for δ_1 or δ_3 , and should be clear from the context of discussion). The constant terms σ^f and σ_n are retained to show explicitly the possibility of non-zero tractions on the crack faces and these terms represent limits of shear and normal tractions as the tip is approached from within the crack. Clearly no real material can withstand infinite stresses so that at the crack tip, the material behaves inelastically (shown schematically as the lightly shaded region at crack tip, Fig. 1). The continuously rising σ_{ij} as

$r \rightarrow 0$ is therefore an artifact of the assumption of elastic behavior in the analysis from which (1) and (2) are derived. At larger distances the terms left out in the asymptotic expansion become significant and should not be ignored. The stress field (1a) and (2a) are therefore valid in an annular region (shown as shaded in Fig. 1) surrounding the crack tip. This is often described as the K-dominated region.

Equation (1) and (2) completely describes the spatial distribution of the near-tip stress field and the crack face displacement. This form is independent of the geometry of the body containing the crack, and does not depend on the particular manner in which the body is loaded. This information is contained in K , which is indeed the utility of (1): For any geometry and loading where K is known, the near tip stress field and crack face displacement are completely specified. Since K defines the strength of the stress singularity at the crack tip, it is the parameter which is used in Irwin's fracture criterion mentioned earlier.

Many solutions have been obtained for elastostatic crack problems. For a summary of solution methods, see Parker (1981). Solutions for the stress intensity factor K are tabulated in Tada et al (1973) and Paris & Sih (1965). It is useful to recognize

(by dimensional considerations) that K must have the form

$$K = \sigma \sqrt{L} F(\text{geometry, loading}) \quad (3)$$

where σ is a generalized loading stress and L is a characteristic length in the geometry of the body (often the crack length or half crack length). The non-dimensional function F depends on the details of geometry and loading. For example, for a center crack with half crack length ℓ in a plate loaded remotely by σ^0 and with uniform shear resistance σ^f (Fig. 2),

$$K_{II} = (\sigma^0 - \sigma^f) \sqrt{\ell} \sqrt{\pi} \quad \text{or} \quad (4a)$$

$$= \Delta\sigma \sqrt{\pi\ell} \quad \text{where } \Delta\sigma \equiv (\sigma^0 - \sigma^f) \quad (4b)$$

showing that F is a constant ($\sqrt{\pi}$) in this simple case. The second form (4b) suggests the usual interpretation of stress drops $\Delta\sigma$ in seismological literature. In that case, σ^0 is the shear stress prior to seismic rupture and σ^f is the residual friction on the ruptured fault segment. The in-situ absolute values of the stress states σ^0 and σ^f are not readily determinable. However, it is usually the stress (or strain) change that is of interest. Hence σ^f may be regarded as a reference stress state.

Another example is a semi-infinite crack in an infinite body whose crack faces are loaded by line forces P at a distance b from the crack tip (in force/unit thickness) as shown in Fig. 3. The

stress intensity factor is given by

$$K_{II} = \frac{P}{b} \sqrt{b} \sqrt{\pi} \quad \text{or} \quad (5a)$$

$$= \sqrt{\frac{2}{\pi b}} P \quad (5b)$$

This result may be used to generate (by superposition) the stress intensity factor for an arbitrarily loaded crack face.

A popular model for representing the anti-plane deformation field of a strike-slip plate boundary (uniform along strike) with a shear zone sliding under a locked seismogenic layer is shown in Fig. 4. The quasi-plastic shear zone is modelled as the lower edge crack of length a while the upper edge crack with length b has been used to simulate shallow creep by Tse et al (1985). Of course, putting $b=0$ is equivalent to locking the shallow crust, a model first employed by Turcotte & Spence (1974) in analyzing surface strain profiles along a line perpendicular to the plate boundary. The stress intensity factors at the lower and upper edge crack tips are given by (Tse et al, 1985).

$$K_{III}^{(a)} = \sigma \sqrt{H} \sqrt{2 \sin(\pi a/H) / (\alpha + \beta)} \quad (6a)$$

and

$$K_{III}^{(b)} = \sigma \sqrt{H} \sqrt{2 \sin(\pi b/H) / (\alpha + \beta)} \quad (6b)$$

where $\alpha = \cos(\pi a/H)$ and $\beta = \cos(\pi b/H)$. In section 4.4 this model

is used in a more detailed analysis of plate boundary deformations.

2.1.2 Energy Release Rate G

The energy release rate G is defined to be the energy flux to the crack tip zone per unit crack length advance (per unit width along crack front). For mode II shearing, this definition affords a connection between G and K_{II} (see e.g. Irwin, 1960). Referring to Fig. 5 and by recognizing that the process of crack extension is to cause the material in a small zone $\Delta\ell$ to slip an amount $\delta_1 = \frac{(1-\nu)}{\mu} K_{II} \sqrt{8(\Delta\ell-x_1)/\pi}$ (1b) with stress reduction $\Delta\sigma_{21}$ from $\frac{K_{II}}{\sqrt{2\pi x_1}} + \sigma^f$ (1a) to the residual friction σ^f , the work absorption per unit crack advance and hence the energy release rate may then be calculated as

$$\begin{aligned}
 G &= \lim_{\Delta\ell \rightarrow 0} \frac{1}{2\Delta\ell} \int_0^{\Delta\ell} \Delta\sigma_{21}(x_1) \delta_1(\Delta\ell-x_1) dx_1 \\
 &= \lim_{\Delta\ell \rightarrow 0} \frac{1}{\Delta\ell} \frac{(1-\nu)}{\mu\pi} K_{II}^2 \int_0^{\Delta\ell} \sqrt{\frac{\Delta\ell-x_1}{x_1}} dx_1 \\
 &= \frac{(1-\nu)}{2\mu} K_{II}^2
 \end{aligned} \tag{7}$$

If other modes of deformations are involved, the additional work absorbed into the crack tip has to be accounted for and in that

case (following the same line of reasoning as above)

$$G = \frac{1}{2\mu} \left[(1-\nu)(K_I^2 + K_{II}^2) + K_{III}^2 \right] \quad (8)$$

For generalized plane stress deformation in mode I or II, $(1-\nu)$ should be replaced by $1/(1+\nu)$ in (8). The linear superposition is appropriate here because the three deformation modes are independent of one another directly ahead of the crack tip. This same form is obtained by Dmowska and Rice (1986) in an elegant presentation starting with an infinitesimal growth of a general three-dimensional crack front and considering the associated energy changes in the body containing such a crack. For a given mode of fracture, (8) explains why the Griffith's fracture criterion based on G is equivalent to Irwin's fracture criterion based on K .

The critical energy release rate G_c of the earth's crust may be estimated by various means, which we shall discuss in some detail in section 3. For now we would like to illustrate a use of elastic brittle crack mechanics with a simple example. Consider the creeping segment of the San Andreas fault in central California as a large crack of length $2l$ in an elastic plate (the lithosphere) under mode II generalized plane stress deformation (Fig 2). This is of course a crude approximation only, although the currently locked segments of the 1857 and 1906 ruptures and the enhanced background seismicity near San Juan Bautista and near

Parkfield lend credence to such a representation. The enhanced seismicity and the short cycle (approximately 21 years) of moderate Parkfield earthquakes may be considered as local slip instabilities in the breakdown zones of the megascale crack. With an effective length ℓ and a driving stress $\Delta\sigma$, the crack face slip displacement is given by (see, e.g. Muskhelishvili, 1953)

$$\delta = \frac{2\Delta\sigma}{\mu(1+\nu)} \sqrt{\ell^2 - x_1^2} \quad (9)$$

Equation (9) is used to generate a curve fit for field data of fault creep in Fig. 6, which shows four sets of fault slip rate measurements (after Burford and Harsh, 1980; Lisowski and Prescott, 1981; Schulz et al, 1982) and slip rate prediction based on (9). (Since we have a linear problem, the slip rate $\dot{\delta}$ is related to the stressing rate $\dot{\Delta\sigma}$ in the same manner as δ is related to $\Delta\sigma$ in (9)). The geodolite data set should be weighted more than the other sets because it reflects relative displacement further out (up to 5 km) on each side of the fault trace than the other data sets and is therefore more suitable for the two dimensionality of the present crack model.

The energy release rate may be estimated from

$$G_c = \frac{\pi}{8} \mu(1+\nu) \frac{\delta_{\max}^2}{\ell} \quad (10)$$

Equation (10) has been obtained by combining (4), the plane stress

version of (7) and (9) with $\delta_{\max} = \delta(x_1=0)$. The field data show a maximum slip rate of 3.4 cm/yr near Monarch Peak. If an average repeat time of 160 years is assumed for great ruptures of the 1857 or 1906 type, then $\delta_{\max} \approx 5.44$ m. Equation (10) then gives $G_c = 6.3 \times 10^6 \text{ Jm}^{-2}$ for $\nu=0.25$, $\mu = 35 \text{ GPa}$ and $l = 80 \text{ km}$. The estimated value of G_c may yet be higher if one considers that seismic ruptures occur in the shallow crust of say, 10 km in a 50 km thick lithosphere. In that case, the (thickness-averaged) G_c should be weighted by a factor of 5 which then results in $G_c = 3.2 \times 10^7 \text{ Jm}^{-2}$.

Rice and Simons (1976) also used (10) to calculate G_c for a fault creep event on the San Andreas which occurred on July 17, 1971 and was reported by King et al (1973). The maximum slip value δ_{\max} recorded by the four creep stations was 9 mm and the length of the creep zone was reported to be 6 km. Using $\nu=0.2$ and $\mu=20 \text{ GPa}$, Rice and Simons calculated a $G_c = 2.6 \times 10^2 \text{ Jm}^{-2}$. This is one of the lowest values for G_c reported based on field observations. Presumably the episodic creep events involve extension of slip zones in clay gouges with low strength (see section 3 and Tables 3 and 4) or small confining pressure at shallow depth, whereas seismic ruptures of the 1857 or the 1906 types involve the breaking of both fissured and competent rocks.

An alternative more fundamental view of the energy release rate, based on its basic definition but without referring to the linear elastic stress and deformation fields given by (1) or (2),

is the following: Suppose a tube of material bounded by the contour Γ surrounding the crack tip is cut, as shown in Fig. 7. The energy flux going into this tube of material is used up in elastic straining of the material in A, in frictional work on the crack face L, and in supplying energy to drive the extension of the crack. If the crack extends at a steady speed $v = da/dt$, then for unit thickness in direction x_3 ,

$$\int_{\Gamma} T_i (du_i/dt) d\Gamma = \frac{d}{dt} \int_A W dA + \int_L \sigma^f (d\delta_i/dt) dx_1 + G(da/dt) \quad (11)$$

where $T = \sigma \cdot n$ is the traction vector acting on Γ , and W is the elastic strain energy density, defined as $\int_0^{\epsilon_{mm}} \sigma_{ij} d\epsilon_{ij}$. This statement of energy balance presumes that any energy absorbed by inelastic deformation apart from frictional work, can be lumped into G . For steady state extension where self similarity is preserved (i.e., an observer riding with the moving crack tip always observes the same view) one can replace the time derivative $\partial/\partial t$ by $-v\partial/\partial x_1$ since in that case $x_1 = x_1 - vt$ where x_1 refers to a coordinate system fixed in space. Also if the contour Γ is shrunk onto the crack tip, the frictional work term can be eliminated. Thus (11) becomes

$$G = \lim_{\Gamma \rightarrow 0} \int_{\Gamma} \left[n_1 W - T_i \frac{\partial u_i}{\partial x_1} \right] d\Gamma \quad (12)$$

For dynamic crack propagation, an additional term involving kinetic energy dissipation must be added inside the integral (Cherepanov, 1968; Dmowska and Rice, 1986; Freund, 1976; Kostrov and Nikitin, 1970).

2.2 The J-integral

The J-integral is defined by (Rice, 1968a)

$$J = \int_{\Gamma} \left[n_1 W - T_i \frac{\partial u_i}{\partial x_1} \right] d\Gamma \quad (13)$$

for two-dimensional quasi-static deformation fields in elastic solids. Comparison with (12) shows that G is equivalent to J in the limit that the contour Γ shrinks onto the crack tip and when the self-similarity condition leading to (12) holds. In general J may be interpreted as the excess of energy flux through Γ over the elastic strain energy absorption by the material inside Γ .

The J integral has been shown to vanish on a closed contour containing no singularity, for an elastic material which is homogeneous, at least in the x_1 direction (Rice, 1968a). The J -integral is one component of a set of three conservation integrals noted by Eshelby (1957) as characterizing energetic (or configurational) forces on localized inhomogeneities in elastic solids, and its exploitation in treating crack problems was first pointed out by Rice (1968a,b). An energy release interpretation as in (12) was published by Cherepanov in 1967, (in Russian). (He

did not seem to realize that the J-integral was path-independent at that time.).

For a mode II shear crack with shear traction σ on the crack face (Fig. 8), the conservative property implies that

$$J_Q + J_{Q^+P^+} - J_P + J_{P^-Q^-} = 0 \quad (14)$$

J_Q is the J-integral on a contour starting from a point Q^+ on the upper face of the crack, surrounding the crack tip and ending on the point Q^- on the lower side of the crack face; $J_{Q^+P^+}$ is the J-integral on a short contour from Q^+ to P^+ along the upper crack face, etc. Equation (14) may be reduced to

$$J_Q + \int_Q^O \sigma(\partial\delta/\partial x_1) dx_1 = J_P + \int_P^O \sigma(\partial\delta/\partial x_1) dx_1 \quad (15)$$

where each integral already incorporates contributions from both the upper and lower crack faces on which $n_1=0$ and $\delta = u_1^+ - u_1^-$. In the case where the crack faces are traction-free, i.e. $\sigma=0$, then $J_Q=J_P$, resulting in the path-independent property of J. In shear cracks, however, σ is usually non-zero. The statement (15) is valid for any points P and Q. If we allow the point P to approach the crack tip O, the integral term on the right hand side of (15) vanishes and the remaining part $\lim_{P \rightarrow O} J_P$ is just the energy release

rate G , by (12) and (13). Thus for mode II shear cracks

$$G = J_Q + \int_Q^0 \sigma (\partial \delta / \partial x_1) dx_1 \quad (16a)$$

Obviously the right hand side of (16a) cannot depend on the specific point Q . For uniform $\sigma = \sigma^f$, the integral term in (16a) is simply $-\sigma^f \delta_Q$, i.e.,

$$G = J_Q - \sigma^f \delta_Q \quad (16b)$$

Equation (16b) is a result of the small scale yielding condition for a shear crack, and affords another interpretation of J : It is the energy sum of crack driving force and frictional dissipation.

Equation (16b) may be exploited to obtain estimates of the crack driving force by choosing contours on which the terms in (13) can be easily evaluated. As an illustration, Rudnicki (1980) estimated the G_c for initiation of the 1857 California rupture using (16b) and the contour shown in Fig. 9. The contour is chosen such that the left vertical branch cuts across the San Andreas where it has been locked and the material there is assumed to deform uniformly with shear strain γ_0 . Similarly the point Q is located well inside the creep zone in central California such that uniform shear straining γ_r may again be assumed. On both of the vertical contours, a pure shear state assumption implies that

$\partial u_i / \partial x_1 = 0$. (The origin and the crack tip are located approximately at Cholame). The quantity δ_Q represents the creep magnitude at point Q. The horizontal contours are chosen at $x_2 = \pm h/2$ where loading is essentially imposed by displacement. There $n_1 = 0$ and $\partial u_i / \partial x_1 = 0$ (due to uniform imposed displacement) so that no contribution is made to the J-integral. The only contributions come from the strain energy of the vertical branches. Thus

$$\begin{aligned} J_Q &= W(\gamma_o)h + 2W(\gamma_r) (-h/2) \\ &= h \int_{\gamma_r}^{\gamma_o} \sigma(\gamma) d\gamma \end{aligned}$$

The fault creep δ_Q may be estimated from the difference between the strains well inside the locked segment and well inside the creep zone, i.e.

$$\begin{aligned} \delta_Q &= (\gamma_o - \gamma_r)h \\ &= h \int_{\gamma_r}^{\gamma_o} d\gamma \end{aligned}$$

Thus at rupture initiation the critical energy release rate, using

(16b), is

$$G_c = h \int_{\gamma_r}^{\gamma_o} [\sigma(\gamma) - \sigma^f] d\gamma$$

$$= \frac{\mu}{2h} \delta_Q^2 \quad (17)$$

if it is assumed that $\sigma(\gamma) - \sigma^f = \mu [\gamma - \gamma_r]$ for linear elastic behavior. It is interesting to note that (17) has the same form as (10), with ℓ replaced by h and δ_{\max} by δ_Q . The factor $\pi(1+\nu)/8$ in (10) also is close to $1/2$ as in (17) for $\nu = 0.25$.

For numerical estimates, δ_Q should reflect the part of the relative plate motion accommodated by the San Andreas. Minster and Jordan (1984) suggested a slip rate of 35 mm/yr, which translates to $\delta_Q \approx 0.035 \times 145\text{m} = 5.08\text{m}$ for a repeat time of 145 years (Sieh, 1984). Strain rate profiles based on geodetic measurements (King, N.E., personal communications, 1984) on the Carrizo Plain and San Luis net decay from the fault trace and appear to flatten out at approximately 60 km. Thus 60 km seems to be an appropriate value for h . Using a crustal averaged shear modulus $\mu = 35 \text{ GPa}$, (17) gives G_c to be $7.5 \times 10^6 \text{ Jm}^{-2}$. Again this value would be increased to $3.8 \times 10^7 \text{ Jm}^{-2}$ if we consider that seismic ruptures occur to a depth one-fifth the lithospheric thickness. These values are slightly larger than Rudnicki's original estimate because of different values assumed for δ_Q and

for μ . They are consistent with the $6.3 \times 10^6 - 3.2 \times 10^7 \text{ Jm}^{-2}$ estimate using surface creep rate data from central California (section 2.1.2). The calculated value of G_c should be considered as an order of magnitude estimate only because of simplifying assumptions. For example the model shown in Fig. 9 assumes that the creep zone extends indefinitely north of Cholame. This can only be an approximation of the finite length ($\approx 160 \text{ km}$) of the creeping section of the San Andreas.

This section reviews shear fracture mechanics. The fracture parameters K , G and J are introduced, and their relation to one another emphasized. Applications of fracture mechanics to model plate boundary deformation and various techniques in extracting fracture parameters based on seismic and geodetic observations are demonstrated. Elements of this section form the basis for further discussions of the mechanics of shear rupture in sections III and IV.

III. SLIP-WEAKENING MODEL OF SHEAR RUPTURE

Laboratory observations from tri-axial tests in rocks indicate a complex breakdown process in the localized shear band in the post-peak regime. This breakdown process may involve buckling of slender columns in grains segmented by microcrack arrays, kinking in plate-shaped grains and rotation and crushing of joint blocks as seen under SEM (Evans and Wang, 1985). On a larger scale, direct shear testing of rock joints indicates shearing off and crushing of asperities in jointed rock mass, the

micromechanics being sensitive to the normal stress applied across the joint (see, e.g., Coulson, 1972). Both tri-axial rock specimens and direct shear jointed rock specimens in the laboratory show a decreasing shear load carrying capacity as a function of the amount of sliding. Some samples of such experimentally measured slip-weakening curves for initially intact rock specimens are shown in Fig. 10. Slip-weakening curves for jointed rock specimens are shown in Fig. 11. These slip-weakening σ - δ relations define simple constitutive laws governing shear slip behavior. While direct use of experimental results in the field for earthquake faults may not be appropriate because of differences in size scales of fault zone structures in comparison to laboratory scale specimens, one may expect that certain behavior of fault slip may be governed by similar slip-weakening relations. This is so because for a fault to exhibit seismicity, its strength must degrade with on-going slip.

In the following discussion (Section 3.1) a general constitutive model for the slip-weakening process is introduced. The model is an extension to shear faulting by Palmer and Rice (1973) and Ida (1972) of the well-known cohesive zone models of tensile fractures developed by Barenblatt (1962) and Dugdale (1960) for metal. (The cohesive zone model was also used to describe crack extensions in concrete by Hillerborg et al (1976) and Li and Liang (1986). In this case the breakdown process involves the joining of discontinuous microcracks and pull-out of

the aggregates from the cement matrix). The slip-weakening model will then be applied to an analysis of stability of a simple sliding system (Section 3.2). Relationship between the slip-weakening model, the J-integral and the elastic brittle crack model will then be described in Section 3.3. In Section 3.4 we shall discuss some estimates of the parametric values in the slip-weakening σ - δ relations from laboratory tests of rocks, rock joints and overconsolidated clay and from in-situ field observations of natural fault behaviors.

3.1 Slip-Weakening Constitutive Model

A simple general form of the slip-weakening constitutive model may be written as

$$\sigma = f(\delta, \sigma'_n, T) \quad (18)$$

where $\sigma'_n = \sigma_n - p$ is the effective normal compressive stress (normal stress σ_n reduced by pore pressure p) acting across the slip surface, and T is temperature. A schematic plot of (18) is shown in Fig. 12 which indicates a continuous decay of strength from σ^p to σ^f at large slip beyond a critical slip displacement δ^* .

Triaxial tests in rocks by Wong (1986) suggest that σ^p and σ^f both increase in a manner such that $\sigma^p - \sigma^f$ first increases but then decreases with increasing σ_n , indicating a transition from

brittle to ductile deformation. In a separate series of tests at constant normal stress, Wong (1982b) shows that the stress drop $\sigma^P - \sigma^f$ decreases with temperature. The σ_n and T dependence of σ^P and σ^f is illustrated in Fig. 12b,c. These considerations of normal stress and temperature dependence are important when the constitutive law is applied to the earth's crust, as in the work of Stuart & Mavko (1979), Li and Rice (1983a,b) and Li and Fares (1986). It is assumed in the slip-weakening relation that unloading and reloading from the weakening branches occur along vertical paths (Fig. 12a), i.e. no reverse sliding accompanies a load removal.

The model as described has no dependence on slip rate, although recent rock experiments by Dieterich (1978,1979), Ruina (1983) and Tullis and Weeks (1986) indicate that frictional sliding behavior has slip rate and state dependence. An implication of ignoring rate and state dependence is that slip events could not be repeated on the same surface since no mechanism for restrengthening is available. Thus the slip-weakening model is unable to describe transitions from one earthquake cycle to another. Even so, the model is capable of simulating sliding behavior quite adequately in most situations. It is in fact a more general description of shear slip phenomenon than the elastic brittle crack model, which we shall reveal as a limiting case of the slip-weakening model in Section 3.3.1.

3.2 Stability Analysis of a Single-degree-of-freedom System

3.2.1 Sliding of a spring-block system

An earthquake may be regarded as a loss of stability in slip on the fault surface. If the slip weakening σ - δ relation is a fair constitutive description of the fault zone, then it should, in the minimum, allow a sliding surface to initiate a rapid slip event subsequent to some stable slip. It is important to note, however, that whether an unstable event is generated or not depends not only on the constitutive relation of the sliding surface but also on the stiffness of the system (loading system and the body which contains the sliding surface) through which load is transmitted to the surface. To see this more explicitly, consider the mechanical behavior of a simple spring-block system, as shown in Fig. 13a. The block is assumed to be rigid and the sliding surface is governed by a slip-weakening relation (solid line) shown in Fig. 13b, i.e., the shear stress σ acting on the sliding surface and the block movement δ follow such a relationship. The block is loaded through a spring which is pulled forward by the amount δ_0 . The normal stress acting on the block, as well as the temperature on the sliding surface, are assumed to remain constant during the sliding process.

The force equilibrium equation governing the system can be written as

$$T = \sigma \quad (19)$$

where T is the spring force. The load and load point displacement

are related by

$$T = k(\delta_0 - \delta). \quad (20)$$

This incorporates information of the structural stiffness of the medium (the spring) through which loading is applied to the sliding surface. Equations (19) and (20) may be combined and rewritten as

$$\sigma = -k\delta + k\delta_0 \quad (21)$$

which then defines an unloading line of the loading system with a negative slope $-k$ in the σ - δ space (Fig. 13b), and with an intercept $k\delta_0$ on the vertical σ -axis. Equation (21) expresses that equilibrium of the system is satisfied on any point of this unloading line. However, for each unloading line shown, only its intercept with the σ - δ curve can be the true equilibrium point since the sliding surface is governed by the constitutive relation $\sigma = \sigma(\delta)$, i.e.,

$$\sigma(\delta) = -k\delta + k\delta_0 \quad (22)$$

Thus a series of equilibrium points A, B, C, D may be traced as δ_0 is increased by pulling on the spring. The unloading lines illustrated have been drawn at equal (vertical) intervals such

that δ_0 is increased uniformly in time simulating a steady load point displacement. The block displacement ($\delta_A \rightarrow \delta_B \rightarrow \delta_C \rightarrow \delta_D \dots$), however, accelerates with time. For the σ - δ relation and spring stiffness k shown in Fig. 13b, equilibrium could be maintained only up to Point E. In the sequence from A through E the force in the system rises to a peak (at D) and then decreases. At point E the system becomes unstable in the sense that an infinitesimal increase in δ_0 causes a sudden jump in δ (the block shoots forward from δ_E) accompanied by a stress drop. This is schematically illustrated in Fig. 13c. The final equilibrium position can be any one of the states F, G or H. These points are constrained by the fact that unloading of the spring must follow the unloading line E E at instability, and that the sliding surface must still obey the slip-weakening law (including the rigid unloading branches, Fig. 12a). Furthermore, the energy loss from the spring must be converted into work of sliding the surface, which implies that

$$\frac{1}{2} (\sigma_E + \sigma_H) (\delta_H - \delta_E) = \int_{\delta_E}^{\delta_H} \sigma(\delta) d\delta \quad (23)$$

which is how the point H is defined. However, if energy is partially lost through seismic radiation (or heat generation other than that related to the frictional work on the right side in (23)), then the final resting equilibrium position may be at F or

G, and the equal sign in (23) should be replaced by \geq when δ_H is replaced by δ_F or δ_G . As mentioned earlier, the slip weakening constitutive framework do not allow a natural restrengthening of the slipped surface. Hence reloading from G or H would follow first the rigid branches and then along the residual friction plateau. In such a system, a single instability is allowed but no repeated events can be generated.

The question of how much stable sliding and at what load level instability sets in could be addressed by considering springs of different stiffnesses. The case of an infinitely stiff spring (vertical unloading lines) is analogous to applying the load directly onto the rigid block such that the load point and the block move stably together ($\delta=\delta_0$). In the case of an extremely compliant spring ($k \rightarrow 0$), the unloading lines are close to horizontal and the instability point would be at the peak of the slip-weakening curve. In the case of a stiff spring whose stiffness is greater than the negative of the slope at any point of the weakening branch, as shown in Fig. 13d, no instability would occur. The stress and slip development are schematically shown in Fig. 13e for this case. Note that while the slip accelerates, its rate does not approach infinity, as in the case of a true instability (Fig. 13c). This may be a useful conceptual model for what is known as "slow earthquakes" (see, e.g. Sacks et al, 1978).

The considerations of where on the weakening branch

stability is lost explain why it is necessary to use very stiff machines in the laboratory (the loading assemblies act as part of the springs) if one is interested in tracing the weakening branch in a direct shear test. Of course the remarks here apply to tension or compression loaded specimens just as well (see, e.g. Jaeger and Cook, 1969).

Often, in real geophysical systems, the load transmitting medium behaves viscoelastically. A more detailed discussion of such a medium will be given in section 4.2. For now we consider a simple single-degree-of-freedom system, and incorporate the viscoelastic behavior in the form of a standard linear element as shown in Fig. 14a. This element has the property that for long time response, or under $\partial(\delta_0 - \delta)/\partial t \approx 0$ relaxed condition, the system stiffness is given by k_1 . For short time response, or under $\partial(|\delta_0 - \delta|)/\partial t \rightarrow \infty$ unrelaxed condition, the increased stiffness approaches $k_1 + k_2$. In between these two limits, the dashpot modulates the contribution of k_2 to the total stiffness. In reference to Fig. 14b the system undergoes stable deformation up to the point I, where the unloading line associated with a relaxed stiffness k_1 is tangent to the slip-weakening curves. Once rapid acceleration is initiated, the dashpot is activated and effectively stiffens the loading medium. At this point the system is self driven in the sense that the block continues to slide to the right even if the load point has stopped moving, but the motion may still be considered quasi-static, following the path I

to D. At point D where the element stiffness has reached its maximum limit $k_1 + k_2$, dynamic instability sets in, an analogue of an earthquake. The period of deformation corresponding to I to D may represent a precursory period when anomalous activities associated with rapid straining are revealed. The viscoelastic element sets the time scale of this precursory period.

The discussion presented in this sub-section provides a general conceptual framework for stability analysis of any slip-weakening or strain-softening system. The instability delayed mechanism could be associated with viscoelastic stiffening as described above, or it could be associated with drainage responses in a poro-elastic medium.

3.2.2 Application to Fault Stability Analysis

As an illustration of some of the salient points raised in the above instability analysis, we digress from the spring-dashpot slip-weakening model to consider a more realistic time-dependent fault system. Li and Rice (1983a,b) analyzed the stability of stressing of a seismic gap zone in which progressive failure eventually lead to an earthquake at a strike-slip tectonic plate margin. The actual problem involves a seismic gap zone of length 2ℓ in an elastic lithospheric plate underlain by a viscoelastic foundation. The lithosphere is assumed to undergo plane-stress deformation and is coupled to the asthenosphere in the form of a

simple foundation (Fig. 15a). A modified Elsasser model (Rice, 1980, Lehner et al, 1981) is used to include the resistance (to rapid deformation) due to viscoelastic coupling as body forces in the lithosphere. Further, the driving stress $\sigma^0(t) - \sigma(t)$ (averaged over the lithospheric thickness, Fig. 15b) is assumed to be uniform over the gap zone. This causes the thickness-averaged slip displacement to be distributed as in (9) for a crack model. Li and Rice (1983a,b) related the average of this slip over the seismic gap to the driving stress using the representation

$$\delta(t) = \int_{-\infty}^t C(t-t) \frac{d}{dt} [\sigma^0(t) - \sigma(t)] dt \quad (24)$$

which is an extension of (21) to incorporate the viscoelastic effects of the stress transmitting medium. Here the driving displacement $k\delta_0$ has been replaced by the driving load term σ^0 and of course k is the inverse of the compliance $C(t)$ in (24). Indeed this correspondence may be easily seen in the long-time (relaxed) elastic limit, in which case (24) becomes

$$\delta(t) = C(\infty) [\sigma^0(t) - \sigma(t)] \quad (25)$$

and in the short time limit, in which case (24) becomes

$$d\delta = -C(0)d\sigma \quad (26)$$

To further relate σ^0 to the physical driving mechanism - the relative plate velocity V_{pl} - we may consider the time derivative of (25). In that case, the slip rate $d\delta/dt$ averaged over several earthquake cycles must correspond to V_{pl} and the stressing rate $d\sigma/dt$ must average out to zero. Thus $d\sigma^0/dt = V_{pl}/C(\infty)$, consistent with the loading term $k\delta_0$ in (21). This direct interpretation of σ^0 in terms of V_{pl} was noted by Tse and Rice (1986).

The compliance function $C(t)$ is shown in Fig. 16 for $2\ell = H$ and $2\ell = 5H$, obtained from numerical inversion of C from the Laplace transform space (Li and Rice, 1983a, Appendix B). The zero time and infinite time limits of $C(t)$, however, are derivable in analytic forms

$$C(0) = \frac{H^2}{(1+\nu)\ell\mu} \int_0^{2\ell/H} \left[\operatorname{erf} \sqrt{\phi} \right]^2 d\phi \quad (27a)$$

$$C(\infty) = \frac{8L}{\pi(1+\nu)\mu} \quad (27b)$$

Naturally, the compliance at infinite time corresponds to a plate with a completely relaxed foundation and could be obtained directly from (9) by taking the average over $-\ell$ to $+\ell$ in x_1 . (However, (27b) is actually $16/\pi^2$ times the exact result from (9), due to an approximation in representing a finite length crack by a semi-infinite crack with a uniformly loaded finite portion from the crack tip (Lehner et al, 1981). A way to compensate for this

discrepancy is to regard l as an effective crack length equal to $\pi^2/16$ of the actual length). The compliance at time zero corresponds to a fully coupled lithosphere/asthenosphere system so that $C(\infty) > C(0)$. In addition, the compliance may be expected to increase monotonically with seismic gap zone length l and to decrease with shear stiffness μ .

As explained earlier in connection with the standard element, the effect of an increasing stiffness (or decreasing compliance) with increasing slip velocity is to delay the final instability. Li and Rice (1983a,b) analyzed the details of this precursory stage by solving (24) together with a crustal scale (averaged over the lithospheric thickness) σ - δ relation of plate boundary deformation. It should be noted that this σ - δ relation is not a material constitutive law as for the slip-weakening model, even though it exhibits similar behavior of decreasing σ with increasing δ as the slip zone penetrates into the seismogenic zone, as described below.

The crustal scale σ - δ relation is derived based on an anti-plane strain analysis of an edge crack strip (Fig. 15c or Fig. 4 with $b=0$) representing the deformation behavior averaged over the seismic gap zone. In this case σ and δ are related

parametrically through the crack length a

$$\sigma = \left[\mu G_c(a)/H \tan(\pi a/2H) \right]^{1/2} \quad (28a)$$

$$\delta = (4H/\pi\mu) \left[\mu G_c(a)/H \tan(\pi a/2H) \right]^{1/2} \ln \left[1/\cos(\pi a/2H) \right] \quad (28b)$$

by requiring that σ be of magnitude that just meets the fracture criteria at crack depth a . Thus $G_c(a)$ is a prescribed quantity which should reflect the changing fracture property of the shear zone in the Earth. Section 3.4.1 describes experimental observations of the effect on G_c due to changes in temperature and pressure. Li and Rice (1983a,b) choose a Gaussian distribution with depth (Fig 17a), with parameters adjusted to fit typical focal depths and the thickness of the seismogenic layer. Thus, for example, the maximum of G_c , or G_{\max} , lies at the seismogenic depth.

It may be noted that (28a) is consistent with the stress intensity factor calculation (6a) and (8) for an elastic brittle crack model. Indeed (28a) affords an estimation of the critical energy release rate in the earth's seismogenic zone. Based on an average stress drop of 30 bars reported to be typical of great plate boundary ruptures (Kanamori and Anderson (1975)) and a focal depth of about 10 km appropriate for great ruptures on the San Andreas, G_{\max} was constrained to $4 \times 10^6 \text{ J/m}^2$. Li and Rice

(1983a) also suggested that this choice of G_c produced slip magnitudes of 2.5 - 4.5m consistent with observed seismic slip magnitudes of great California ruptures.

The resulting σ - δ relation based on (28) and on the Gaussian distribution of G_c is shown in Fig. 17b. Stability analysis of the plate boundary may follow the graphical analysis of the single-degree-of-freedom system shown in Fig. 13 or 14, at least up to the point of initial instability. This corresponds to the state when the compliance $C(t)$ just drops below that of $C(\infty)$, after which the numerical solution of (24) becomes necessary. Naturally (24) must now be regarded as an integral equation for δ , when σ inside the integral is expressed in terms of δ through (28). Li and Rice gave numerical solutions following through the process from peak stress, through initial and dynamic instability. The time-evolution of a , δ , and σ are shown in Fig. 18, for two different loading rates defined by the parameter $R = t_r \dot{\sigma}^0 / (K_m / \sqrt{H})$, in which t_r is the relaxation time of the asthenosphere (see e.g. Lehner et al, 1981 or Li and Rice, 1983a) and K_m is the fracture toughness corresponding to G_{max} . It may be noted that while the plate boundary stress σ is decreasing, (Fig. 18b) the average a and δ (Fig. 18a,c) are increasing and their time derivative reaches infinity at dynamic instability. The time scale of the self-driven progression from state I to D depends, among other things, on the relaxation time t_r of the asthenosphere.

While the model described above gives a plausible representation of the gross phenomenon of the precursory processes leading to loss of stability, i.e., an earthquake, the single-degree-of-freedom model is obviously an over-simplification of the source mechanism. The earthquake source process may involve a local nucleation followed by subsequent spreading of the fault surface along strike. This is even more likely when one considers the possibility of spatial variation of material properties and geometric features so that α , δ and σ may be highly location dependent on the fault. To include along-strike variation, Tse et al (1985) and Li and Fares (1986) analyzed a multiple-degree-of-freedom system to be described in section 4.4. Another inadequacy is related to the assumption of the elastic brittle edge crack model to represent the slip penetration which leads to the unavoidable necessity of the loss of stability as the slip zone approaches the ground surface; i.e. no stable continuous creep could be simulated. We shall reexamine this issue after introducing the relationship between the crack model and the slip weakening model in the following section.

3.3 Slip-Weakening Model, J-integral and Elastic Brittle Crack Model

The behavior of shear failure as represented by a single-degree-of-freedom system detailed in the section above is perhaps suitable for small surfaces such as in typical laboratory

specimens. However, such representation is plainly inaccurate for a large surface such as a natural fault. This is because the slippage at each position on a fault surface may be quite different: At some position which has undergone extensive sliding, the stress level may be close to σ^f , whereas other positions may still be high up close to σ^P on the slip-weakening curve. This distributed slip situation contributes to the phenomenon of stress concentration, especially at material points where slip has barely begun (e.g. on the positive sloping branch of the slip-weakening curve, Fig. 12a). Indeed the business of fracture mechanics has, to a large extent, to deal with the intensity of such stress concentrations. Thus the elastic brittle crack model may be considered an extreme member of the slip-weakening model: Outside the crack the material remains elastic, whereas inside the crack the material has all slid down to the residual friction level σ^f , with the exception of a small zone at the crack tip. The smallness of this zone corresponds to the so called small scale yielding condition in elastic brittle crack mechanics. This condition may be addressed within the context of the slip-weakening model if we assume that the inelastic deformation within this small zone is governed by the slip-weakening constitutive relation.

3.3.1 Relationship Between Energy Release Rate G and Slip-Weakening Model Parameters

We show in Fig. 19a the stress distribution near the tip of a mode II sliding surface. The zone of size w contains the stress degradation from peak strength σ^P to residual friction σ^f , at which slip δ has reached the critical value δ^* . The weakening branch of the slip-weakening curve is shown in Fig. 19b.

We now apply the J-integral with a contour going along the lower and upper crack faces surrounding the breakdown zone, beginning and ending at a point Q located well beyond $x_1 = -w$ (Fig. 19a). Recognizing that no crack tip singularity exists due to the presence of the breakdown zone, Eq. (16a) implies

$$0 = J_Q + \int_Q^0 \sigma(\partial\delta/\partial x_1) dx_1 \quad (29)$$

where $\sigma = \sigma(\delta)$ according to the slip-weakening relation. The integral term may be rewritten as

$$\int_Q^0 \sigma(\delta) \frac{\partial\delta}{\partial x_1} dx_1 = - \int_0^{\delta^*} [\sigma(\delta) - \sigma^f] d\delta - \sigma^f \delta_Q \quad (30)$$

by realizing that σ is a single valued function of δ (if no unloading occurs) and hence $(\partial\delta/\partial x_1)dx_1 = d\delta$, and that the square bracket on the right hand side of (30) vanishes for $\delta > \delta^*$. Thus

(29) and (30) leads to

$$J_Q - \sigma^f \delta_Q = \int_0^{\delta^*} [\sigma(\delta) - \sigma^f] d\delta \quad (31)$$

which may be interpreted as follows: The excess energy flux (above doing frictional work) made available balances the energy absorption in the breakdown process for slip zone extension. Equation (31), with the left hand side interpreted as a crack driving force and the right hand side interpreted as a fracture resistance, then affords a criterion for propagation of the slip zone. It is useful to note that the quantity $(J_Q - \sigma^f \delta_Q)$ cannot depend on the particular point Q (since the right hand side of (31) is independent of the point Q), which suggests that $(J_Q - \sigma^f \delta_Q)$ is a path-independent parameter for cracks with crack face tractions, with the stipulation that the point Q be outside the breakdown zone. Palmer and Rice (1973) used (31) to evaluate the criterion for the propagation of a shear band in over-consolidated clay in a long shear box and for the extension of a slip surface in a soil slope loaded by gravity in response to a step cut in the slope. Indeed Rudnicki's calculation of G_c for initiation of the 1857 rupture on the San Andreas described in section 2 is an extension of the shear box analysis by Palmer and Rice.

It should be noted that the derivation of (31) makes no

assumptions about the size of the breakdown zone. To make contact with elastic brittle crack models, however, (16b) based on an infinitesimal breakdown zone (consistent with the uniform $\sigma = \sigma^f$ assumption) may be combined with (31) to give

$$G = \int_0^{\delta^*} [\sigma(\delta) - \sigma^f] d\delta \quad (32a)$$

within the context of the slip-weakening model. This integral is just the shaded area under the slip-weakening curve (Fig. 19b) and may be rewritten as

$$G = (\sigma^P - \sigma^f) \bar{\delta} \quad (32b)$$

in which the nominal slip distance $\bar{\delta}$ is defined as

$$\bar{\delta} = \frac{1}{\sigma^P - \sigma^f} \int_0^{\delta^*} [\sigma(\delta) - \sigma^f] d\delta$$

Thus in the limit when the size of w is small, the slip-weakening model is consistent with the elastic brittle crack model with $G_c = (\sigma^P - \sigma^f) \bar{\delta}$. At incipient faulting, the critical energy release rate G_c is now interpretable in terms of the product of the stress drop and the nominal slip, parameters which describe the crack tip breakdown process.

3.3.2 Estimation of the Breakdown Zone Size w :

The breakdown zone size w at crack initiation may be estimated from the fact that the net stress intensity K_{net} must vanish for no stress singularity at 0, i.e.,

$$K_{\text{net}} = K_{\text{applied}} + K_{\text{bdz}} = 0 \quad (33)$$

where K_{applied} is the stress intensity factor due to applied load which is just equal to the critical value K_c at initiation of crack growth, and K_{bdz} is the stress intensity factor due to excess (over friction) shear resistance in the breakdown zone. Clearly, K_{bdz} is a negative quantity and may be calculated if the stress distribution in the breakdown zone is known. In general this information requires the solution of a singular integral equation which we shall describe in section 4.1. As an estimate, Palmer and Rice (1973) used an inverse method in which a linear stress distribution is assumed, and the resulting σ - δ relation is shown to resemble an actual slip-weakening curve (Fig. 20). In this case

$$\sigma(r) - \sigma^f = (\sigma^P - \sigma^f) (1 - r/w) \quad (34)$$

and using (5b) and superposition,

$$K_{bdz} = - \sqrt{\frac{2}{\pi}} \int_0^w \frac{\sigma(r) - \sigma^f}{\sqrt{r}} dr \quad (35)$$

Thus (33) together with (34) and (35) implies

$$w = \frac{9\pi}{32} \left[\frac{K_c}{\sigma^P - \sigma^f} \right]^2 \quad (36)$$

or using (7) and (32b)

$$w = \frac{9\pi(1+\nu)}{16} \frac{\mu \bar{\delta}}{(\sigma^P - \sigma^f)} \quad (37)$$

Full numerical solution of the singular integral equation mentioned earlier indicates that (36) gives a good estimate within 10% error if the slip-weakening curve has a linear decaying shape (Li and Liang, 1986). However, (36) is inadequate for a material with an exponentially decaying slip-weakening curve with a long tail (i.e. large δ^*).

This section summarized the connection of the slip-weakening model with the J-integral in general, and with the elastic brittle crack model in the limit when the breakdown zone size w is small. Indeed in the context of the slip-weakening model, w must be smaller than all other characteristic dimensions (crack length,

distance of crack tip to boundary, etc.) in the geometry of the body in order to satisfy the small scale yielding condition required in the use of the simple elastic brittle crack model. Furthermore, since this length is derived from material properties (37), it creates a problem in geometry scaling in laboratory model studies (e.g. centrifuge studies), a difficulty first noted by Palmer and Rice (1973).

It should be clear now that for most laboratory size specimens, w is generally relatively large and may well exceed the dimensions of the slip surface. In this case the single-degree-of-freedom system (Section 3.2) gives a good description of the slip behavior. In the field, linear elastic fracture mechanics may be used whenever w is small enough. In the following section, we examine the applicability of elastic brittle crack mechanics to a plate-boundary model in light of the discussions presented above.

3.3.3 Crustal Scale Applications

We now take up the question of whether the aseismic shear zone below the seismogenic layer at a plate boundary may be modelled by an anti-plane strain mode III elastic brittle edge crack, as shown in Fig. 4 (with $b=0$), assuming that we accept the shear zone as indeed confined to a narrow width even as it approaches the base of the lithosphere. This question may be addressed in the context of a slip-weakening model of the shear

zone proposed by Stuart (1979a,b) relating the local excess (over friction) shear strength σ to the local anti-plane slip displacement $\delta (=u_3^+ - u_3^-)$ in the form

$$\sigma = \sigma(z, \delta) = S \exp\left[-(z-z_0)^2/d^2\right] \exp\left[-\delta^2/\lambda^2\right] \quad (38)$$

Equation (38) has the same Gaussian variation with depth z as assumed in the crack model (Fig. 17a) with σ reaching peak value at z_0 and a spread measured by d . Furthermore in connection with the slip-weakening terminology introduced earlier, S is the strength drop ($\sigma^P - \sigma^f$) and λ is a measure of the critical slip displacement δ^* . To make further contact with the crack model, (32a) requires

$$G_c(a) = \int_0^\infty \sigma(z=H-a, \delta) d\delta \quad (39)$$

and the maximum value of G_c occurring in the seismogenic zone is given by

$$G_{\max} = S \int_0^\infty \exp[-\delta^2/\lambda^2] d\delta = \sqrt{\pi} S\lambda/2 \quad (40)$$

The size of the breakdown zone w may be estimated by (36) adapted

to the anti-plane mode, i.e.

$$w = \frac{9\pi}{16} \frac{\mu G_{\max}}{S^2} \quad (41)$$

For an estimate, supposing a strength drop S of 500 bars, and using the previously estimated $G_{\max} = 4 \times 10^6 \text{ Jm}^{-2}$, the critical slip distance λ is calculated from (40) to be $\lambda \approx 90 \text{ mm}$ and the breakdown zone size $w \approx 100 \text{ m}$ for $\mu = 35 \text{ GPa}$. This breakdown zone size is much smaller than a , $H-a$ and d which are generally greater than several kilometers such that the use of elastic brittle crack model would seem to be justified. While the strength drop must be greater than earthquake stress drop values averaged over the whole fault plane and its value of 500 bars appears to be consistent with the various other estimates (see Table 4), a lower value of say $S = 100 \text{ bars}$ (Aki's (1979) estimate for the 1966 Parkfield earthquake) would make $\lambda \approx 450 \text{ mm}$ and $w \approx 2.5 \text{ km}$ which is still smaller than the characteristic dimensions in the problem but definitely approaching the limit of validity of the elastic brittle crack model. In this case it may be more suitable to carry out the analysis using the slip-weakening model (38). (See, e.g., Stuart (1979a,b) and Stuart and Mavko (1979)). In the last reference, the authors found that stable sliding can be attained by increasing the critical slip distance λ and hence the size of the breakdown zone (see, e.g. Fig. 4a in Stuart and Mavko (1979),

with large λ corresponding to the lower right hand corner). The stable sliding phenomenon cannot be simulated by an elastic brittle crack model for the plate boundary.

3.4 Laboratory and Field Estimates of Shear Fracture Parameters

3.4.1 Laboratory estimates of shear fracture parameters

Rice (1980) showed that laboratory triaxial test data on rocks could be used to deduce shear fracture parameters. Consider the specimen with a throughgoing fault (pre-existing saw-cut or post-peak localization of shear deformation) at an angle $(\pi/2-\theta)$ to the major loading axis σ_1 (Fig. 21a). The specimen deforms under confining pressure σ_3 . During the test, σ_1 , σ_3 and the axial shortening ΔL is continuously monitored. The resulting curve $(\sigma_1-\sigma_3)$ vs. axial shortening ΔL including the softening branch (Fig. 21b) must be stably measured. A stiff machine (or a cyclic technique as used by Wong (1982a,b)) is required to prevent instability. The stability analysis of a single-degree-of-freedom system described in section 3.2 is applicable to such laboratory tests since the breakdown zone size w is generally much larger than the dimensions of the sliding surface. For example, Rice (1980, 1984) computed w for a series of triaxial tests conducted by Rummel et al (1978) in the range of 0.8 -1.2m (corrected to constant normal stress) for initially intact specimens. Most laboratory specimens have dimensions much smaller than this size.

Thus it may safely be assumed that sliding occurs simultaneously at every point of the fault of the specimen. The method of obtaining the slip-weakening curve from the laboratory data is shown graphically in Fig. 21b,d. The shear stress σ and slip δ may be computed from

$$\sigma = \frac{\sigma_1 - \sigma_3}{2} \sin 2\theta \quad (42a)$$

$$\delta = \Delta L_s / \sin \theta \quad (42b)$$

where ΔL_s is the relative displacement of the sliding surface in the axial direction (Fig. 21c). However, the values of peak stress σ^p and the residual stress σ^f are affected by the normal stress acting across the fault, and the normal stress changes during the test according to

$$\sigma_n = \frac{\sigma_2 - \sigma_3}{2} \cos 2\theta + \frac{\sigma_1 + \sigma_3}{2} \quad (43)$$

Rice (1984) suggested a correction procedure based on the Mohr circle diagram. A similar approximate scheme for reducing the raw data to that corresponding to constant normal stress was detailed by Wong (1986), who found that the constant stress correction reduces the uncorrected value of G_c by approximately a factor of two.

Based on the above technique, Wong (1982a, 1982b, 1986) calculated fracture parameters from several series of tests. His test results (and some from other investigators) are summarized in Table 1a. Wong's studies indicate a decreasing trend in the strength drop $\sigma^P - \sigma^f$ with increasing temperature, suggesting a transition from brittle to ductile deformation. Fig. 22 shows a composite of two series of tests, one for San Marcos gabbro and the other one for Fichtelbirge granite conducted at constant temperature. G_c appears to first increase with confining stress up to 0.55 GPa and then decrease. The G_c and $(\sigma^P - \sigma^f)$ variations with temperature and normal stress are consistent with the observation of seismicity confinement in the shallow crustal layer below which quasi-plastic behavior dominates. Conducted at crustal scale confining pressures, these data, while still incomplete, are perhaps the first experimental qualitative evidence in support of the depth variation of slip-weakening parameters assigned in fault stability analysis by Stuart (1979a,b), Li and Rice (1983a,b) and Li and Fares (1986). See section 3.2.2, equation (18) and section 3.3.3, equation (38) for more details. The data summarized by Tse and Rice (1986), while phrased in terms of instantaneous and long term rate sensitivities, suggest a similar variation of strength drop potential.

Apart from triaxial test results, slip-weakening fracture parameters have also been reported by Okubo and Dieterich (1984)

based on bi-axial tests of large scale 2m long simulated faults. At a normal stress of 0.6-4 MPa, they found that G_c ranges from 0.1-2.4 Jm⁻² for Sierra white granite with prepared surface roughness of 0.2μm and 80μm. The critical slip displacement δ^* is reported to be in the 0.2-10μm range for the smooth samples and 8-40μm in the rough samples. The values for G_c and $\bar{\delta}$ ($\approx 0.5\delta^*$), as well as the strength drop $\sigma^P - \sigma^f$, (Table 1b), are several orders of magnitude smaller than the corresponding values from triaxial tests. This lower G_c and $(\sigma^P - \sigma^f)$ may partly be due to the lower confining pressure under which the biaxial experiments have been carried out, but the smaller δ^* is probably related to the reduced surface roughness. Okubo & Dieterich (1984) reported no dependence of δ^* on normal stress.

Direct shear tests on rock joints have been conducted by a number of investigators (e.g. Coulson, 1972; Goodman, 1970, Barton, 1972). Many of these studies have focused mainly on the effect of normal stress on σ^P and σ^f , with little information on the critical energy release rate or the critical slip displacement reported in the literature. However, Yip (1979) collected data from many rock joint tests and found a wide variation in the value of $\bar{\delta}$, with an average of 0.9 mm. Like Okubo and Dieterich (1984), he found that this average value of $\bar{\delta}$ (or δ^*) does not appear to depend on normal stress. While this value of $\bar{\delta}$ is substantially larger than that for intact or sawcut rocks, the critical energy release rates G_c from these rock joint experiments (based on

$\bar{\delta} = 0.9\text{mm}$) are lower than that for intact rocks. This is presumably partially due to the low stress drop ($\sigma^P - \sigma^f$) associated with low applied normal stress in the direct shear tests. Slip-weakening model parameters for some rock joint tests are summarized in Table 2.

Table 3 contains slip-weakening model parameters for over-consolidated clay from direct shear tests. While the stress drops ($\sigma^P - \sigma^f$) are relatively small, the $\bar{\delta}$ values are quite large, on the order of several mm, as opposed to less than 1 mm for both rocks and rock joints. This observation may have important implications for natural fault behavior when clay gouges are involved in the slip-weakening process.

3.4.2 Field Estimates of Shear Fracture Parameters

We have already discussed three methods of estimating in-situ slip-weakening model and fracture parameters from geodetic observations. The first method is based on the elastic brittle crack model and creep rate data from the San Andreas in central California (Section 2.1.2). There we obtain estimates for G_c of $6.3 \times 10^6 \text{Jm}^{-2}$ to $3.2 \times 10^7 \text{Jm}^{-2}$. The second method based on the J-integral analysis gave an estimate of $G_c = 7.5 \times 10^6 \text{Jm}^{-2}$ to $3.8 \times 10^7 \text{Jm}^{-2}$ for the 1857 Ft. Tejon rupture in California (Section 2.2). The third method is based on the anti-plane strain edge cracked strip model of Li and Rice (Section 3.2.2) which gives an estimate of $G_c = 4 \times 10^6 \text{Jm}^{-2}$. Here we shall introduce another rather general technique for estimating fracture

parameters in the slip-weakening model. In this technique, seismological and other earthquake parameters such as rise time t_r , rupture length 2ℓ and average fault slip $\hat{\delta}$ are needed. Of course the average slip may be obtained from the seismic moment and fault surface area (see, e.g. Aki and Richards, 1980). Still other techniques and estimates for natural faults are summarized in Table 4.

Consider a strike-slip earthquake rupture of length 2ℓ (at least several times the plate thickness) as a mode II shear crack (Fig. 2). The average slip along the length of the rupture $-\ell < x_1 < \ell$ may be obtained by integrating (the plane strain version of) (9) to get

$$\hat{\delta} = \frac{1}{2\ell} \int_{-\ell}^{\ell} \delta(x_1) dx_1 = \sqrt{\frac{\pi}{2} \frac{(1-\nu)}{\mu}} \ell G \quad (44)$$

in which the relations of the stress intensity factor to stress drop (4b) and to energy release rate (7) have been used. The product $(\sigma^P - \sigma^f) \bar{\delta}$ in the slip-weakening model may then be calculated using (32b) and (44) once $\hat{\delta}$ is determined from seismological observations. As an additional constraint, information on the rise time t_r of an earthquake rupture may be used. The slip at each point of the fault $(-\ell, \ell)$ at time t may be

assumed to have the form

$$\delta(t) = \frac{(\sigma^P - \sigma^f)\ell}{\mu} \left[1 - \exp(-\beta t/\ell) \right] \quad (45)$$

during rupture, consistent with Brune's (1970) fault model. The coefficient in front of the square bracket in (45) may be obtained from dimensional considerations and β is the shear velocity. Assume further that the slip displacement reaches the average fault slip $\hat{\delta}$ at $t=t_r$, i.e.

$$\delta(t_r) = \hat{\delta} \quad (46)$$

combining (45) and (46) gives the strength drop in terms of the average slip

$$\sigma^P - \sigma^f = \frac{\mu \hat{\delta}}{\ell} \left[1 - \exp(-\beta t_r/\ell) \right]^{-1} \quad (47)$$

and the critical slip $\bar{\delta}$ may be computed from (32b) after solving for G from (44) and $\sigma^P - \sigma^f$ from (47). Once $\bar{\delta}$ and $\sigma^P - \sigma^f$ are known, the breakdown zone size w may be calculated using (37). As an illustration, for the 1976 Turkish earthquake, Purcaru and Berckhemer (1982) gave the following earthquake parameters:

$2\ell = 55$ km, $\hat{\delta} = 2.45$ m, $t_r = 1.5$ s. For $\mu = 35$ GPa, $\nu = 0.25$ and $\beta = 3.5$ km/s, these earthquake data lead to $G_c = 6.5 \times 10^6 \text{ Jm}^{-2}$,

$\sigma^P - \sigma^f = 180$ bars, $\bar{\delta} = 36$ cm and $w = 1.6$ km. The estimate of G_c is of the same order of magnitude as those obtained by other means mentioned earlier.

A similar technique was employed by Niu (1984/5) to calculate the fracture parameters for 49 earthquakes with data compiled by Purcaru and Berckhemer (1982). However, he used a slip-weakening model which has constant stress σ^P up to $\delta = \delta^*$ beyond which $\sigma = \sigma^f$. Such a model does not seem to be in accord with actual material behavior. It is easy to show (see, e.g. Rice, 1980) that this model reduces the breakdown zone size w in (37) by a factor of 4/9. Another method proposed by Ida (1973) and utilized by Aki (1979) to obtain fracture parameters for the 1966 Parkfield earthquake (Table 4) is also rather similar to the one discussed above. The similarity lies in using a source-time model of fault slip to relate the stress-decay ($\sigma^P - \sigma^f$) to some (indirectly) observable time parameter (rise time t_r described above, and time t_M at which the slip velocity becomes maximum for an in-plane shear crack propagating with a uniform velocity used by Aki) and to use elastic brittle crack theory and the slip-weakening model to estimate G_c , $\bar{\delta}$ and w . While there are some differences in the formulae of this class of estimation methods, they are generally insignificant when one keeps in mind that the deduced fracture parametric values should be regarded as order of magnitude estimates only.

Apart from those described above, Table 4 also summarizes

estimates of slip-weakening model and fracture energy parameters by Kikuchi and Takeuchi (1970), Hussein et al (1975), Das (1976), and a number of other investigators.

3.4.3 Variations in Fracture Parameters

It may be seen from the previous discussions and from Table 1 to 4 that the fracture parameters are quite different between those obtained from laboratory tests and those from field observations. The laboratory tests for intact rocks give G_c on the order 10^4 Jm^{-2} (and even lower for sawcut rocks, rock joints and clay) while the field estimates are in the range of 10^5 to 10^8 Jm^{-2} (with the exception of Rice and Simons and some of Hussein's estimates). Similarly the critical slip displacement for laboratory samples are in the μm to mm range, whereas those for field estimates are in the cm to m range. These orders of magnitude differences are unlikely to be due to temperature or normal stress differences since some of Wong's laboratory tests were carried out at close to inferred crustal conditions. There is reason to believe that natural earthquake faults with en-echelon fissures and discontinuities would have "surface roughness" orders of magnitude larger than that for laboratory specimens, thus contributing to the higher $\bar{\delta}$ and G_c values.

To illustrate the plausible dependence of $\bar{\delta}$ on surface roughness, estimated ranges of $\bar{\delta}$ from laboratory tests including intact and sawcut rocks, jointed rocks and clay, as well as from

natural faults are plotted in Fig. 23a. The suggestion is that the increasing "surface roughness" of rocks, jointed rocks and natural faults are, in addition to normal stress, responsible for the increasingly large values of G_c , also shown in Fig. 23b. In summary, these observations indicate that $(\sigma^P - \sigma^f)$ is sensitive to normal stress, whereas $\bar{\delta}$ is sensitive to surface roughness, and their product $\bar{\delta}(\sigma^P - \sigma^f)$ gives the critical energy release rate.

The laboratory rock data on G_c for mode II sliding are generally of the order 10^4 Jm^{-2} . This compares with the much lower value in tensile tests which give data mostly in the range of $10^1 - 10^2 \text{ Jm}^{-2}$ (see e.g., B. Atkinson, this volume. However, the $10^1 - 10^2$ range may be an underestimation of true values; see discussion below.) Presumably the micromechanism of the breakdown process may be quite different, absorbing much more energy in the shear failure mode.

Lastly, estimation of the size of the breakdown zone w for laboratory specimens are easily obtained from the $\bar{\delta}$ and $(\sigma^P - \sigma^f)$ data and applying (37), and they are also listed in Table 1-4. These values of w give an indication of minimum characteristic dimensions in laboratory specimens for a valid K_{IIc} -test. Wong and Rice's analyses of Rummel et al's test results suggest w to be in the 0.1-lm range for granitic rocks. Since most laboratory specimen sizes are smaller, measurements using standard elastic brittle fracture toughness technique are likely to underestimate the true K_{IIc} -values. For example, the references cited by

Atkinson (Table XX in Chapter YY, this volume) give values of K_{IIc} and K_{IIIc} on the order $1 \text{ MPa } \sqrt{\text{m}}$. For $\mu = 15\text{-}30 \text{ GPa}$, $\nu = 0.25$ as typical shear modulus and Poisson's ratio for most surface rocks, this translates to (using (7)) $25\text{-}50 \text{ Jm}^{-2}$. Comparison with Table 1 shows that this is at least two orders of magnitude lower than that obtained through the slip weakening relation, as described in section 3.4.1.

In general, it would seem advisable to avoid using the conventional fracture toughness test, especially for rocks with large grain size (and surface roughness, for mode II) unless unusually large specimens are used. This statement appears to be applicable even for mode I (tension) fracture toughness testing. Figure 24 (after Ingraffea et al, 1984) for example, shows the underestimation of fracture toughness for small specimens and clearly suggests the size dependence of conventional K_{Ic} -test results. The fitted curves are based on a non-linear analysis to be explained in the following section.

IV. SLIP DISTRIBUTIONS AND INTERACTIONS

This section describes the representation of slip surfaces with generally non-uniform slip in a medium of arbitrary geometry and material behavior. In section 4.1, the effect of slippage in transferring loads is discussed through Green's functions which contain information of the medium material behavior and geometry. The formulation results in integral equations when constitutive

relations are imposed on the slip surfaces to relate the local shear stress to local slippage, as. e.g., in the slip-weakening model discussed in Section 3. Such formalism is superior to a kinematic description of fault slip because the slip magnitudes are part of the solution in solving the problem for a prescribed load. The implication is that further physical insight could be gained by understanding the slip progression process, which is of particular significance in the prediction of slip instabilities. Section 4.2 describes the structure of the Green's functions with respect to spatial dependence and their homogeneous and inhomogeneous parts associated with material boundaries. Selected Green's functions most relevant in applications to studies of earth faulting are collected in Table 5. For full descriptions of such and other Green's functions, the reader should consult the references directly. Sections 4.3 and 4.4 review previous studies of earth faulting which made use of the methodology described in 4.1 and 4.2. They are presented in a manner to best illustrate the theoretical concepts developed in this and earlier sections.

4.1 Integral Representation and Physical Interpretations

For a body of any medium with planes of discontinuities, the most general representation of the stress state σ_{ij} at a point x_p and at time t due to some arbitrary slip δ introduced at points x_Q

and at time t along L (Fig. 25) is

$$\sigma_{ij}(\underline{x}_p, t) = \sigma_{ij}^0(\underline{x}_p, t) - \int_L \int_{-\infty}^t G_{ij}(\underline{x}_p, \underline{x}_Q, t, t') \frac{\partial^2 \delta(\underline{x}_Q, t')}{\partial \underline{x} \partial t} d\underline{x} dt' \quad (48)$$

where $\sigma_{ij}^0(\underline{x}_p, t)$ is to be interpreted as the stress state at point \underline{x}_p if no slipping occurs. The stress induced at \underline{x}_p due to slip at all locations \underline{x}_Q is contained in the integral term, carried out over all planes of slip displacement discontinuities. The time integration is needed in the case of a medium in which memory effects are important. These include time-dependent response in a viscoelastic medium and diffusion in a fluid-infiltrated poro-elastic medium. Indeed the information of the structural geometry and the rheology of the stress transmitting medium are contained in the Green's function $G_{ij}(\underline{x}_p, \underline{x}_Q, t, t')$, sometimes known as the influence function. It is the fundamental solution of the stress σ_{ij} at point \underline{x}_p at time t due to a unit shear dislocation suddenly introduced at point \underline{x}_Q and at time t' . Many elastic and some viscoelastic and poro-elastic solutions for various geometries have been obtained. A selection of Green's functions useful in describing slippage effects in earthquake zones are tabulated in Table 5. There have been numerous interesting applications of these Green's functions, some of which will be described in this section.

To give specific interpretation to (48) and to make contact with shear rupture models described in Sections 2 and 3, we assume here that slip occurs on a single plane (e.g., a boundary between two lithospheric plates) between $-\ell < x < \ell$. The plates are subject to remote shear loading σ^0 (Fig. 26). σ^0 may be interpreted as the shear stress transmitted across a fully locked fault due to tectonic scale plate motions. In this case the shear stress component in (48) reduces to

$$\sigma(x_1) = \sigma^0 - \int_{-\ell}^{\ell} \frac{\mu(1+\nu)}{2\pi} \frac{1}{x_1 - x'_1} \frac{\partial \delta(x'_1)}{\partial x_1} dx_1 \quad (49)$$

In (49) the Green's function for an elastic plate under generalized plane stress deformation is used (Case I.2, Table 5).

This equation has the solution (Muskhelishvili, 1953)

$$\begin{aligned} \frac{d\delta(x_1)}{dx} = & -\frac{2}{\pi} \frac{1}{\mu(1+\nu)\sqrt{\ell^2 - x_1^2}} \int_{-\ell}^{\ell} \frac{\sqrt{\ell^2 - x_1^2}}{x_1 - s} [\sigma^0 - \sigma(s)] ds \\ & + \text{constant} / \sqrt{\ell^2 - x_1^2} \end{aligned} \quad (50)$$

where "constant" can be determined only from some supplemental conditions, e.g. no net dislocation in $-\ell < x_1 < +\ell$, see (52b) below, giving "constant" = 0. As a special situation, suppose we impose the condition that all points which slip have stress reduced to a constant residual strength σ^f , then $\sigma(s) = \sigma^f$ in (50) and the slip

distribution $\delta(x_1)$ may be easily computed in terms of the stress drop $\Delta\sigma = \sigma^0 - \sigma^f$:

$$\delta(x_1) = \frac{2\Delta\sigma}{\mu(1+\nu)} \sqrt{\ell^2 - x_1^2} \quad (51)$$

Equation (51) is, of course, the slip distribution of the shear crack model which we described in Section 2 (Eq. (9)) and which we used to calculate the energy release rate based on the creep displacement rate in central California. The imposition of a uniform stress condition on a slip boundary is a characteristic of the crack model. The uniform stress condition is appropriate, if it is assumed that practically all points on the slip surface have undergone sliding exceeding δ^* , in the context of the slip-weakening model, or if a quasi-plastic mechanism dominates the shear deformation behavior in a narrow shear zone as often postulated in the earth's lower crust where the temperature and pressure are high.

More generally, however, it is appropriate to impose a constitutive relation between stress and slip, such as the slip-weakening model. In this case, (50) becomes a singular integral equation in δ , and

$$\sigma(\delta) = \sigma^0 - \int_{-\ell}^{\ell} \frac{\mu(1+\nu)}{2\pi} \frac{1}{x_1 - x'_1} \frac{\partial \delta(x'_1)}{\partial x'_1} dx_1 \quad (52a)$$

the solution of which often requires special numerical methods.

Some numerical procedures have been described by Erdogan and Gupta (1972), Cleary (1976), Stuart and Mavko (1979) and Fares and Li (1986). The equation (52a) and more generally (48) has a unique solution only if the net dislocation is specified. For an internal discontinuity, a zero net dislocation may be specified as

$$\int_{-\ell}^{\ell} \frac{\partial \delta(x'_1)}{\partial x'_1} = 0 \quad (52b)$$

It should be noted that (52a) may in fact be regarded as a multi-degree-of-freedom system extension of (21) in which the stiffness k is analogous to the Green's function here and the driving force $k\delta_0$ is now represented by σ^0 .

We now consider the maximum value of σ^0 that can be applied to the plate (Fig. 26) before the line of discontinuity $-\ell < x_1 < \ell$ extends. This maximum shear load σ^0 may be predicted from brittle elastic fracture mechanics if the breakdown zone is much smaller than the crack length. Thus from (4a) and (7):

$$(\sigma^0)_{\max} = \sqrt{2\mu(1+\nu)G_c/\pi\ell} + \sigma^f \quad (53)$$

If the breakdown zone occupies the complete fault then (19) (with T identified as σ_0) is applicable, and the maximum allowable load would be just the peak value σ^p in the slip-weakening constitutive relation. These limits are plotted in normalized form as the

slanting and horizontal dashed lines in Fig. 27. The characteristic length ℓ_{ch} for normalization of the horizontal scale, is defined by $\ell_{ch} = 2(1+\nu)\mu G_c / (\sigma^p - \sigma^f)^2$ which is proportional to the breakdown zone size w in (36). For intermediate range of the half crack length ℓ , comparable in size to w , (52) together with a zero net stress intensity condition (33) was solved numerically by Li and Liang (1986) and their result for a linear slip-weakening relation is shown as the solid line in Fig. 27. (Li and Liang actually solved for the maximum tensile load, but the solution coincides with the shear case since the Green's functions for the integral equation (52a) are exactly the same for both modes of deformation). Clearly, the full numerical solution confirms the applicability of the elastic brittle crack model when crack size is large in comparison to the breakdown zone size (lower left corner of Fig. 27), and the applicability of the strength concept at the other extreme (upper right corner of Fig. 27).

Conversely, Fig. 27 shows the inadequacy of the strength criterion which overestimates the maximum failure load when displacement discontinuities exist in the loaded medium. This result is consistent with the observation that over-consolidated clay slopes often fail by progressive failure at loads much under the peak strength of the clay (Bjerrum, 1967). The elastic brittle crack model also overestimates the failure load when the breakdown zone is comparable in size to the crack length. This

observation affords an explanation for the underestimation and size-dependence of fracture toughness measured from small specimens in the laboratory and based on linear elastic brittle crack theory, as described earlier in reference to Fig. 24. Indeed the two curve fits in Fig. 24 are based on the predicted peak loads from the non-linear analysis shown in Fig. 27 and using (4). (These results hold for both mode I (with $\sigma^f = 0$) and mode II). To translate from the non-dimensional plot of Fig. 27 to the dimensional plot of Fig. 24, we have used $\sigma^P = 5 \text{ MPa}$, $K_c = 1000$, $1200 \text{ psi}/\sqrt{\text{in}}$ for the lower and upper curves. They are seen to fit the experimental data reasonably well.

4.2 Green's Functions and Their Structures

In the following, we shall further explore the structure of the Green's function for dislocation in media with different geometries and material properties. The emphasis is to bring out the common features between these Green's functions which may on a superficial inspection, have little resemblance between each other. These common features include the spatial dependence and the homogeneous and inhomogeneous parts of the Green's function associated with material boundaries.

For simplicity, we shall confine our focus to 2-D cases, although much of the discussions may be extended to 3-D cases as well. As further restrictions, we shall limit selected Green's functions in Table 5 to static cases, and for geometries most

relevant to studying earthquake faulting problems, and then only the shear stress component on the line of discontinuity will be given. The reader should consult the original literature for a full description of the fundamental solutions. We have divided the selected Green's functions in Table 5 into three categories: they are those for elastic (Case I), viscoelastic (Case II) and fluid-infiltrated poro-elastic media (Case III). Various geometries are possible, such as infinite space, half space, plate structure, or layered. The dislocation may be of an edge type or of a screw type in shear (i.e. in mode II or in mode III). In geophysical terminology, the edge dislocation may represent a semi-infinite (in length) fault in strike-slip or dip-slip. The screw dislocation may represent slip below locked zones in an infinite strike-slip fault. The Green's functions in Table 5 are given for unit, suddenly introduced dislocations.

The single major characteristic exhibited by the Green's function for all media with different materials and geometries is the $1/r$ singularity (where r is the distance measured from the dislocation front). This singular nature of the Green's function makes the integral term in (48) a Cauchy principal value integral. As mentioned earlier, special numerical techniques are available to handle this type of integral. In most cases, terms other than the $1/r$ term occur in the Green's functions. These non-singular terms arise because of the presence of material boundaries. For example, in a layered medium, these boundaries may divide

horizontal regions into layers of different rigidities. Even in a half-space, the free-surface exists as a boundary dividing the medium into a regular one and one with zero rigidity. The non-singular terms are known as the inhomogeneous part of the Green's function whereas the singular terms form the homogeneous part. In many instances, these inhomogeneous terms have been derived by the method of images (see, e.g. Maruyama, 1966, Rybicki, 1971) with each term in a summation series representing an image point about a plane boundary. As an example, Case I.4 shows a screw dislocation at $z = d$ below a free surface. The homogeneous part of the Green's function is of the form $-\mu/2\pi(z-d)$ with a singularity at $z = d$. The inhomogeneous part is of the form $\mu/2\pi(z+d)$ from an image source at $z = -d$, a reflection of the primary source about the free surface boundary.

The elastic rheology assumed for the various geometries shown in Case I of Table 4 is plainly an idealization of the mechanical behavior of the earth's upper crust. Nevertheless the use of elasticity is often justified for the study of short time response. The plate geometry (e.g. case I.1 plane stress) is also useful to describe the very long time response of the lithosphere when the asthenosphere is fully relaxed, i.e. the lithosphere has negligible basal traction and can be therefore treated as a free floating plate.

The viscoelastic behavior of the asthenosphere has been suggested to be responsible for many observable time-dependent

phenomena. For example, Bott and Dean (1973), Anderson (1975), Toksoz et al (1979), Lehner et al (1981), and Li and Kisslinger (1984/85) have studied the diffusion of stress along a plate boundary as a model for migration of great ruptures and for filling-in of seismic gaps. Nur and Mavko (1974), Rundle and Jackson (1977), Thatcher and Rundle (1979), Thatcher et al (1980), Thatcher (1982, 1983, 1984), Melosh and Fleitout (1982), Melosh and Raefsky (1983), Thatcher and Rundle (1984), Thatcher and Fujita (1984), and Li and Rice (1986) have studied the time-dependent post-seismic reloading of the lithosphere. Li and Rice (1983a,b) have studied the stiffening effect of the lithosphere/asthenosphere system as a model for stabilization against fault instability and for a precursory period during which local plate boundary straining accelerates to failure (see Section 3.2.2). A common thread of these models is the recognition of the coupling between the elastic lithosphere and the viscoelastic asthenosphere, with the latter providing the time-dependent effect. Usually the time scale of the modelled phenomenon provides a rough constraint on the relaxation time and the viscosity parameter of the asthenosphere, although other non-earthquake related phenomena such as isostatic rebound from glacial loading have often been used to estimate the viscosity parameter of the asthenosphere.

Case II.1 in Table 5 shows a screw dislocation in an elastic plate underlain by a Maxwell viscoelastic half-space. Again the

Green's function (Bonafede et al, 1986) has a homogeneous and an inhomogeneous part due to the presence of boundaries. For the short time response, the asthenosphere behaves like an elastic body and the stress expression given in Case II.1 is reduced to that in I.6 with $d < H$ and $\mu_1 = \mu_2$ for a screw dislocation in an elastic half-space. This is the high stiffness limit. (See also the discussion in connection with Fig. 14.). For the long time response, the asthenosphere is completely relaxed and the stress expression given in II.1. is reduced to that in I.3 for a screw dislocation in an elastic strip, which corresponds to the low stiffness limit. As the asthenosphere relaxes between these limits, the fault (modelled by the dislocation or a superposition of them) is reloaded and the deformation field on the ground surface also changes. The time scale for these time-dependent transients is given by $\tau = 2\eta/\mu$ (η = viscosity and μ = shear modulus common to both lithosphere and asthenosphere) in this model.

The above discussion may be extended to case II.2 which shows an edge dislocation suddenly imposed in an elastic plate coupled to a viscoelastic foundation through a modified Elsassner model (Rice, 1980, Lehner et al, 1981). In the long time limit, the system reduces to that of an edge dislocation in a free floating plate (Case I.2, plane stress), as can be shown by taking the limit of the time-dependent part of the Green's function, i.e. $\gamma(x_1, t \rightarrow \infty) = \frac{1}{x_1}$. For this model, the relaxation time is given by

$$\beta/\alpha = (\pi^2 H/32h)(2\eta/\mu).$$

While there have been several viscoelastic solutions reported in the literature, most of them are limited to the time-dependent surface displacements only. This is clearly due to the interest of modelling post-seismic ground movements based on kinematic dislocation models. Unfortunately, Green's functions of the type we discuss here are not widely available.

The time-dependence afforded by a fluid-infiltrated poro-elastic medium comes from the diffusion process associated with pore-fluid flow. Such time-dependence has been used as a means of modelling after-shock distributions (Booker, 1974, Nur and Booker, 1972, Li et al, 1986) and water well level fluctuations (Roeloffs and Rudnicki, 1984/85). The stiffening effect of an undrained medium on stabilization against faulting has been discussed by Rice and Simons (1976) and Rice (1979). Cases III.1 and 2 show the Green's functions for an edge dislocation in such a medium for a permeable (Rice and Cleary, 1976) and an impermeable (Rudnicki, 1986) fault. The time scale for both is controlled by the relaxation time $4c/x_1^2$ where c is a coefficient of consolidation (see Rice and Cleary, 1976). In the long time relaxed limit, the Green's function for Case III.1 reduces to that of Case I.1 (plane strain).

It should be noted that Table 5 represents a small set of available Green's functions in the literature. As an example, the Green's function for edge dislocation near a circular cavity in an

elastic medium has been derived by Dundurs and Mura (1964). Such a Green's function could be used to construct the integral equation to describe the sliding of a joint near a rock tunnel in geotechnical engineering. The possibilities are unlimited, and the reader is urged to read the above discussions as a general framework which may be specialized to particular applications, with the use of the proper Green's function. Many other Green's functions can be found in Mura (1982). For many structural geometries containing displacement discontinuities, the Boundary Element Method coupled with the appropriate Green's function can often provide a powerful tool of analysis superior to the Finite Element Method (Fares and Li, 1986).

4.3 Applications to Dip Slip Faulting

Two dimensional kinematic models have been used by Chinnery and Petrak (1968) and Freund and Barnett (1976) to simulate surface vertical movements due to dip-slip faulting on vertical and dipping faults. The two dimensionality of these models is usually justified on grounds that dip slip faultings occur on fault planes with lengths much longer than the widths (in the dip direction). In this section we describe a non-kinematic model due to Dmowska (1973) and Dmowska and Kostrov (1973) where the fault slip is not preassigned. Instead the fault surface is assumed to have uniform and constant shear resistance. This corresponds to the assumption of the elastic brittle crack model. Our discussion

will begin with the integral representation described in Section 4.1, and making use of the appropriate Green's function.

Using the coordinate system shown in Figure 28, and specializing to the shear component in the plane of the fault surface (48) becomes

$$\sigma(s) = \sigma^0(s) - \int_{s_1}^{s_2} G(s-s) \frac{\partial \delta(s)}{\partial s} ds \quad (54)$$

where the time integral has been dropped for the case when the material is elastic (with no time-dependent behavior). The appropriate Green's function is due to Freund and Barnett (1976) (see also Dmowska (1973)) and is shown in Table 5, Case I.5,

$$G(s-s) = \frac{\mu}{2\pi(1-\nu)} \left[\frac{1}{s-s} - \frac{\sum_{n=0}^5 \lambda_n(s)^n s^{5-n}}{[s^2 + s^2 - 2ss \cos 2\alpha]^3} \right] \quad (55)$$

where λ_n are functions of the dip angle α and are given in Table 5 (I.5). The presence of the traction free ground surface is accounted for by the inhomogeneous part of the Green's function. In (54) σ^0 is interpreted as the preexisting tectonic load if the fault plane is locked. (In most physical situations, only the change in tectonic load is important since only the change, and not the true value, in surface deformation can be measured.) Assuming that the fault plane slips with uniform shear resistance,

the left hand side of (54) is then a constant σ , and (54) reduces to

$$\sigma^o(s) - \sigma^f = \int_{s_1}^{s_2} G(s-s) \frac{\partial \delta(s)}{\partial s} ds \quad (56)$$

The singular integral equation (56) has been solved by Dmowska (1973) using quadrature formula to discretize the integral, which reduces to a set of linear algebraic equations that can be easily handled by a computer. The resulting slip distribution, which scales with $\sigma^o - \sigma^f$, is plotted schematically in Figure 28 along the fault plane. Using a vertical displacement influence function derived by Freund and Barnett, the associated vertical movement on the ground surface can also be predicted and is schematically sketched in Figure 28 as well.

The model described above may be made more realistic by considering a more sophisticated constitutive relation on the fault plane. For example, Dmowska indicated a method of incorporating pressure-sensitive friction effects. In that case, the shear resistance on the fault would depend on the tectonic normal stress acting across the fault and the friction coefficient. In addition, slip on the fault plane (in the presence of the traction-free boundary) would induce normal stress changes and the right hand side of (54) would have an extra term similar to the integral term but with a Green's function relating

normal stress change to shear slip. The inclusion of friction does not cause any more difficulty in the numerical solution of the singular integral equation.

The analysis could be made even more complete when a slip-weakening constitutive law relating shear stress and slip is prescribed on the fault plane, as done by Stuart (1979a). The slip-weakening law employed by Stuart (similar to (38)) reflects not only a gradual degradation of slip resistance with increased amount of slip, but also reflects the increasing ductility (shear flow as opposed to brittle fracture) with increasing depth. Although Stuart used the finite element method, the formulation described above is quite suitable to treat the problem. The only difference introduced is on the left hand sides of (54), where σ is now made to depend on δ through the slip-weakening law. Introduction of such a term makes the singular integral equation non-linear, and the resulting set of non-linear algebraic equations will have to be solved by means of an iterative scheme.

The advantage of such non-kinematic models is that the fault slip can come out as part of the solution, and in general is more realistic than an imposed uniform dislocation or uniform stress. Such non-uniform slip distribution would clearly influence the predicted surface deformation behavior, especially if the tip of the fault plane is relatively close to the ground surface. In addition, it is possible to simulate the progressive failure process in response to increased tectonic loading. The failure

law is inherent in the slip-weakening model, and Stuart used this to calculate the vertical movement at various stages prior to the 1971 San Fernando earthquake. These results are reproduced in Figure 29a and is seen to qualitatively fit the available geodetic data. The fault geometry and the variation of peak stress is shown in Fig. 29b. It is interesting to note that fault slip occurs mostly below 20 km down dip prior to 1969, and a catch up process of rapid slip near the hypocenter occurs from 1969 up to the 1971 rupture (Fig. 29c). Inferences of such non-kinematic models provide a means of studying the failure process leading up to the slip instability, an earthquake analogue. In general, it may be expected that surface deformation may show characteristics associated with the approach of an instability, such as accelerated vertical movement or strain rates. (See, e.g. Stuart and Mavko, 1979 for a detailed discussion of slip instability in the context of a strike-slip fault.) Although present available data on such precursory signals are scant, precursory deformation may nevertheless be useful for assisting future earthquake forecasting efforts.

4.4 Application to Slip-stress Interaction Along an Inhomogeneous Fault

Several directly or indirectly observable fault zone behaviors suggest that fault surface strength (resistance to slip motion) is spatially inhomogeneous. These observations include

seismicity concentrations, and episodic creep and repeated ruptures of different fault segments. A direct result of fault strength inhomogeneity is the non-uniform distribution of fault slip and stress accumulation, which no doubt influence surface deformation behavior. Thus interpretation of geodetic measurements must consider not only depth changes of fault property but also along-strike fault property changes, particularly where measurements are made close to junctures where segments of very different fault behavior occur. In addition, and especially relevant to the discussions in this chapter the stressing of a locked location must be sensitive to the slippage of nearby creeping segments, and such slip-stress interaction must be accounted for when considering the processes leading to the nucleation of a shear rupture.

Based on the integral representation described in Section 4.1, Tse et al (1985) analyzed the stressing of locked patches along a creeping fault. Equation (52a), where the Green's function for a mode II edge dislocation in an elastic plate (Case I.I in Table 5) has been used, describes the mechanics of the two-dimensional lithospheric plate shown in Figure 30a. The plate is loaded by tectonic stresses σ^0 , and the plate boundary responds with a distribution of shear stress $\sigma(x_1)$ and slip $\delta(x_1)$. These parameters must necessarily have quantities averaged over the thickness of the plate, which is treated as undergoing plane stress deformation. It is possible to incorporate the depth-wise

change of fault zone properties at the plate boundary by considering a cross section at x_1 , as shown in Figure 30b. This section is assumed to undergo antiplane strain deformation, the analysis of which provides a spring relationship connecting the thickness averaged stress $\sigma(x_1)$ and the thickness averaged slip $\delta(x_1)$ through a local spring constant $k(x_1)$. It is in this spring constant where the details of the depthwise changes in fault properties are incorporated. This spring relation is used for the left hand side of (52a) which again results in a singular integral equation. The formulation of a quasi-three dimensional problem described above is really a generalization of the powerful line-spring procedure introduced by Rice and Levy (1972) for treatment of part-through surface cracks in tension-loaded elastic plates or shells. Parks (1981) has shown the remarkable accuracy of the approximate procedure in calculating stress intensity factors by comparing it to full scale 3-D finite element calculations. The procedure has been used by Li and Rice (1983a,b) to analyze strike-slip ruptures in tectonic plates as described in section 3.2.2.

As a specific model, Tse et al (1985) approximated the fault zone as sliding under constant stress (taken as zero reference stress) at all depths except for a locked seismogenic zone, as shown schematically in Figure 4. The free sliding to a depth of $b(x_1)$ is meant to represent shallow fault creep, and the free sliding below the seismogenic zone (between $z=b(x_1)$ and $z=H-a(x_1)$)

is meant to represent shear flow under essentially constant stress. It is useful to note that the geometry of the locked patch along-strike is then defined through the dependence of the parameters $a(x_1)$ and $b(x_1)$ on x_1 . The assumptions described above in essence define an anti-plane strain problem of an elastic strip containing two surface edge cracks of depths a and b . The solution was obtained by conformal mapping technique and the resulting spring constant, which relates the local stress $\sigma(x_1)$ to the local slip $\delta(x_1)$ in Fig. 30a by $\sigma(x_1) = k(x_1) \delta(x_1)$, is (Tse et al, 1985)

$$k(x_1) = \left(\frac{\pi\mu}{2H}\right) / \ln \left[2 / \left[\cos \frac{\pi a(x_1)}{H} + \cos \frac{\pi b(x_1)}{H} \right] \right] \quad (57)$$

The stress intensity factors are given in (6). Note that when a and b vanish, the spring constant approaches infinity. This means that the local fault slip $\delta(x_1)$ must be zero for any finitely imposed stress when that local segment is fully locked. In (52a) the integral limits at $-l$ and l imply that $\delta=0$ beyond this range of interest, and this results in a jump in stress σ at this junction due to the displacement discontinuity. To overcome this unnatural artifact, Tse et al modified this assumption to one where the stress falls to the tectonic load level σ^0 beyond the range $-l < x < l$, and the assumed uniform slip there can easily be computed using (57) for a given far field spring constant k_∞ . Thus (52a) has an additional term contributed by such far field

uniform dislocation, resulting in the form

$$\begin{aligned}
 k(x_1)\delta(x_1) + \frac{\mu(1+\nu)}{2\pi} \int_{-\ell}^{\ell} \frac{1}{x_1-x_1'} \frac{\partial \delta(x_1')}{\partial x_1'} dx_1' \\
 = \sigma^0 \left[1 + \frac{\mu(1+\nu)}{\pi k_{\infty}} \frac{\ell}{\ell^2 - x_1^2} \right] \quad (58)
 \end{aligned}$$

Equation (58) is used to study the stressing processes of various fault locking geometries. Figure 31a shows one of these simulations with the lower margin of the locked region chosen from depth of the seismicity considerations. For a loading rate $\dot{\sigma}^0$ of $0.3 \times 10^{-6} \mu/\text{yr}$, the predicted thickness-averaged and surface slip rates are shown in Fig. 31b. Geodetic creep data are shown as the various symbols in the same figure. In Fig. 31c the thickness average stressing rate is shown to vanish in the creep zone and falls to the tectonic level at large x_1 , as required. The stressing rate is very high at the tip of the submerged locked patch at $x_1 = 35\text{km}$, a consequence of interaction between the free slip to its left and the sudden locking to its right. Another interesting result obtained from the analysis of Tse et al is the estimation of the fracture energy release rate of 10^7 Jm^{-2} along the lower margin of the locked 1857 rupture zone, based on required stressing rate to match observed creep data and an assumed earthquake cycle time of 150 yr. This order of magnitude estimation is again consistent with other estimates already

mentioned in section 3 (see also Table 4). Tse et al noted that their attempt to model the locked patch at Parkfield (based on the local seismicity and creep data) was limited by the short wavelength geometric changes along strike and the basic requirement of long wavelength changes in the line-spring formulation.

Stuart et al (1985) solved the same problem using a three dimensional version of (48). A three-dimensional Green's function due to Chinnery (1963) for a rectangular dislocation patch in an elastic half space was employed. Shear resistance on the fault plane again takes the form of a bell-shaped slip-weakening law (38). Their model parameters were constrained by repeated measurements of fault creep. Figure 32 shows one of their computed results compared to creep data near the Parkfield region for more than a decade. While an instability event occurring at Parkfield is placed at around 1987, Stuart et al cautioned that the data would not be sufficient to constrain all the model parameters until the fault creep enters the (nonlinear) accelerating stage.

The model of Stuart et al appears to be more suitable to analyzing the Parkfield region because of the inherent three-dimensional nature of the patch geometry. For elongated patches, such as that recently analyzed by Stuart (1984/5) for the 500 km segment of the San Andreas fault south of Parkfield, the line-spring formulation used by Tse et al should be quite

adequate. A characteristic of Stuart and co-worker's models, as opposed to many of the available kinematic models in the literature, is the ability to analyze the process leading to an instability, which might form the corner stone of any earthquake forecast model. This is not possible for kinematic models even if they are able to simulate available surface deformation data, since no failure criterion (such as in the form of critical energy release rate or slip-weakening law) is employed to track the progression of fault slip.

The line-spring procedure described above in connection with Tse et al's work could track the progressive failure process if a failure criterion is imposed. For the mode III edge crack model (Figure 4) used, the suitable criterion would be a critical energy release rate. Li and Fares (1986) studied the stress accumulation and slip distribution at the junction of a creep segment and an adjacent segment where slip penetration into the seismogenic zone occurs under increasing tectonic load. No shallow creep was simulated in that study (i.e. $b(x)=0$ in Figure 4 and in (57)). In anticipation of future studies of multiple lines of interacting displacement discontinuities, (48) was recast into an indirect Boundary Element formulation (Fares and Li, 1986). Following Stuart (1979a,b), but in terms of energy release rate based on elastic brittle crack mechanics, the failure criterion was a depth-dependent one, as shown in Fig. 17a. An interesting result of that analysis was the prediction of a long-term stable slip

rate distribution of a parabolic shape in the creep zone, decreasing gradually into the adjacent zone which undergoes slip penetration and is capable of seismic rupture. With extensive slip penetration, the slip-softening behavior becomes more evident at this segment, eventually leading to a loss of equilibrium of quasi-static slip. This process is accompanied by slip rate acceleration, which exceeds that inside the creep zone, as shown in Figure 33.

While the models described in this section and in section 4.3 incorporate important elements for the study of the instability process, results from such instability models nevertheless have to be treated with caution. This is because of the assumption of pure elastic behavior in the body containing the planes of slip discontinuities. In the real earth, the elastic lithosphere is underlain by a viscoelastic upper mantle and, possibly, contains a viscoelastic lower crust. Time-dependent phenomena attributed to the viscoelastic relaxation effect has been described in section (4.2). To incorporate the viscoelastic effects, it would be necessary to use one of the Green's functions of the type listed in Table 5 case II, and the singular integral equation (48) requires both a spatial integration and a time integration to account for the memory of past slip events. The full solution of such an equation is presently not available in earthquake instability analyses. A reduced form of (48) where slip is averaged over the length of progressive slip zone penetration

(e.g. in a seismic gap) has been considered by Li and Rice (1983a,b) (see Section 3.2.2). They found that the instability predicted from the models described above corresponds to the onset of a quasi-static self-driven period in which stable sliding is still maintained but slip acceleration would be inevitable even if the tectonic load is kept constant. Physically, this implies that a precursory stage, whose time duration is associated with the viscosity parameter of the asthenosphere, may precede a dynamic instability, or an earthquake rupture. For short term earthquake forecasting of great ruptures, it appears to be important to capture and interpret the seismic and geodetic data in this precursory stage. Future studies of this type of model, with full solution of (48), should provide further insight into the time and spatial redistribution of surface deformation associated with spreading of the softening zone from one or more nucleation points on the eventual fault plane prior to a great rupture.

V. SUMMARY AND CONCLUSION

This article has focused on the fundamentals of theoretical modelling of shear rupture. The slip-weakening model is used as a means to unify the discussion, with the elastic brittle crack model as one limiting case of extreme non-uniform slip and the strength model as the other limiting case of essentially uniform slip. The slip-weakening model is regarded as a general constitutive law for slip surfaces. Implications in stability of

slip systems, and on the extraction of material fracture resistance parameters are discussed. Non-kinematic models of faulting in various geometries are reviewed and Green's functions are described in the context of distributed slip for media of elastic, viscoelastic and poro-elastic behaviors.

Although the available theories of shear rupture have provided much insight into understanding the mechanics of earth faulting, a complete understanding of many phenomena remains out of reach. Recent advances in rate and state dependent constitutive laws based on careful experimental observations appear to provide a rich foundation on which the transition of one earthquake cycle to another could be better understood. There appears to be a need to study non-kinematic models in media with inelastic behavior in order to understand natural phenomena sensitive to the time-dependent rheology of the earth. Finally, natural faults are never ideally straight and with only a single strand, and fault surfaces are likely to have mechanical properties varying along-strike and with depth. These characteristics call for 3-D modelling, in order to describe non-uniform distributed slip on multiple non-linear fault strands. It is likely that the fault constitutive laws, fault geometry and the medium rheology all play important roles in controlling the time and location of the nucleation of a slip instability. Advances in understanding slip rupture behavior will have to come from laboratory and in-situ experimentation and from analytic and

numerical modelling. While progress has been and will continue to be made in the near future in these directions, it may be expected that serious obstacles exist. For example, it is not clear how one might translate experimental observations in the laboratory to the field given the orders of magnitude difference in the values of slip-weakening model parameters obtained in the laboratory and those estimated from field observations. Also, the more sophisticated and complete a model is, even if sufficient computational power is available (which is not necessarily the case for non-linear problems of the type suggested by the rate and state dependent friction laws), the more model parameters will need to be constrained. At the present time, available geophysical data, especially those collected precursory to a large plate boundary rupture, is extremely limited.

VI. ACKNOWLEDGEMENTS

The author acknowledges useful discussions with the following individuals: R. Dmowska, H. Einstein, N. Fares, H.S. Lim, J.R. Rice and W.D. Stuart. H.S. Lim contributed significantly to the preparation of the tables and figures in this text. I thank C. Benoit for typing this manuscript under a very tight schedule. This article was written when my child Dustin was born. I am grateful to my wife, Stella, for her immaculate patience, to my mother-in-law, for her helpful assistance at home, and to my son for sleeping through the night. This work would not have been

completed without the generous cooperation of all the individuals mentioned here.

This article was prepared under support of the NSF Geophysics Program, the USGS Earthquake Hazards Reduction Program, and the NASA Crustal Dynamics Program.

VII. REFERENCES

- Aki, K. (1979). *J. Geophys. Res.* 84, pp. 6140-6148.
- Aki, K. and Richards, P.G. (1980). *Quantitative Seismology Theory and Methods*, Vol I & II, W.H. Freeman, San Francisco.
- Allen, C.R. and Smith, S.W. (1966), *Bull Seism. Soc. Amer.* 56, pp. 966-967.
- Anderson, D.L. (1975). *Science*, 187, pp. 1077-1079.
- Ashby, M. and Hallam, S.D. (1986). *Acta Metall.* 34, 3, pp. 497-510.
- Barenblatt, G.I. (1962). In "Advances in Applied Mechanics", Academic Press Inc., London, V.7, pp. 55-125.
- Barton, N. (1972). *Int. J. Rock Mech. Min. Sci.*, 9, pp. 579-602.
- Bjerrum, L. (1967). *Trans. Am. Soc. Civil Engrs.* SM 93, pp. 3-49.
- Bonafede, M., Boschi, E. and Dragoni, M. (1986). *J. Geophys. Res.*, in press.
- Booker, J.R. (1974). *J. Geophys. Res.* 79, pp. 2037-2044.
- Bott, M.H.P., and Dean, D.S. (1973). *Nature*, 243, pp. 339-341.
- Brune, J.N. (1970). *J. Geophys. Res.* 75, pp. 4997-5009.
- Burford, R.O. and Harsh, P.W. (1980). *Bull. Seism. Soc. Am.* 70, pp. 1233-1261.
- Cherepanov G.P. (1968). *Int. J. Solids Struct.* 4, pp. 811-831.
- Chinnery, M.A. (1961). *Bull. Seismol. Soc. Amer.* 51, pp. 355-372.
- Chinnery, M.A. (1963). *Bull. Seismol. Soc. Amer.* 53, pp. 921-932.

- Chinnery, M.A. (1970). In "Earthquake Displacement Fields and the Rotation of the Earth" (edited by L. Mansinha et al). Dordrecht Reidel, pp. 308.
- Chinnery, M.A. and J.A. Petrak (1967). *Tectonophysics* 5, pp. 513-529.
- Cleary, M.P. (1976), *International J. for Numerical Methods in Engineering*, 10, pp. 679-720.
- Coulson, J.H. (1972). In Proceedings of XIII 1971 U.S. Symposium on Rock Mechanics, (E.J. Cording, ed.), pp. 77-105.
- Das, S. (1976). In "A Numerical Study of Rupture Propagation and Earthquake Source Mechanism", PhD thesis, M.I.T..
- Dieterich, J.H. (1978). *Pure Applied Geophys.* 116, pp. 790-806.
- Dieterich, J.H. (1979). *J. Geophys. Res.* 84, pp. 2161-2168.
- Dmowska, R. (1973). *Publ. Inst. Geophys. Acad. Sci.* 62, pp. 124-139.
- Dmowska, R. and Kostrov, B.V., (1973). *Archives of Mechanics* 25, 3, pp. 421-440, Warszawa.
- Dmowska, R. and Rice, J.R. (1986). In "Continuum Theories in Solid Earth Physics" (R. Teisseyre, ed.) pp. 187-255, Elsevier Publishing.
- Dugdale, D.S. (1960). *J. of Mech. Phys. Solids* 8, pp.100-104.
- Dundurs and Mura (1964). *J. Mech. Phys. Solids* 12, pp. 177-189.
- Erdogan, F. and Gupta, G.D. (1972). *Quarterly Applied Mathematics*, pp. 525-534.

- Eshelby, J.D. (1957). *Proc. Roy. Soc. (London) Ser. A* 241, pp. 376-396.
- Evans, J.B. and Wong, T.F. (1985). In "Mechanics of Geomaterials, Rock Concrete and Soil", (Z. Bazant ed.).pp. 189-210. John Wiley & Sons, Chichester.
- Fares, N. and Li. V.C. (1986), *J. Engineer. Frac Mech.*, in press.
- Freund, L.B. (1976). *Mechanics Today* 3, Nemat-Nasser (ed.) S., Pergamon, N.Y., pp. 55-91.
- Freund, L.B. and Barnett, D.M. (1976a). *Bull. Seism. Soc. Amer.* 66, 3, pp. 667-675.
- Freund L.B. and Barnett, D.M. (1976b). *Bull. Seism. Soc. Amer.* 66, pp. 2083-2084.
- Goodman, R.E. (1970). In "Determination of the In Situ Modulus of Deformation of Rock", ASTM STP 477, pp. 174-196.
- Griffith, A.A. (1920). *Phil. Trans. Roy. Soc. London, Ser. A*221, pp. 163-198.
- Head, A.K. (1953). *Proc. Phys. Soc. (London)* B66, pp. 793-801.
- Hillerborg, A., Modeer, M. and Petersson P.E. (1976). *Cem. and Concr. Res.* 6, pp. 773-782.
- Hirth, J.P. and Lothe, J.L. (1986). *Theory of Dislocations*, McGraw Hill, NY.
- Husseini, M.I., Jovanovich, D.B, Randall, M.J. and Freund, L.B. (1975). *Geophys. J.R. Astr. Soc.* 43, pp. 367-385.
- Ida, Y. (1972). *J Geophys Res.* 77., pp. 3796-3805.
- Ida, Y. (1973). *Bull. Seismol. Soc. Amer.* 83 , pp. 959-968.

- Ingraffea, A.R., Gunsallus, K.L., Beech, J.F. and Nelson, P.P. (1984). ASTM STP 885, pp. 152-166.
- Irwin, G.R. (1960). In "Structural Mechanics: Proc. of 1st Sym. on Nav. Struc. Mech, 1958" (Goodier and Hoff. eds) pp. 557-591, Pergamon Press, NY.
- Jaeger, J.C. and Cook, N.G.W. (1969). "Fundamentals of Rock Mechanics", Methuen and Co., Ltd., London.
- Kanamori, H. and Anderson, D.L. (1975). *Bull Seism Soc. Amer.* 65, pp. 1073-1095.
- Kasahara, K. (1981). "Earthquake Mechanics", Cambridge University Press, Cambridge.
- Kikuchi, M. and Takeuchi, H. (1970). *Zisin*, 23, pp. 304-312.
- King, C.Y., Nason, R.D. and Tocher, D. (1973). *Phil. Trans. Roy. Soc. London, Ser. A*, 274, pp. 255-360.
- Kostrov B.V. and Nikitin L.V. (1970). *Arch. Mech. Stos.*, 22, 750.
- Lehner, F.K., Li, V.C. and Rice, J.R. (1981). *J. Geophys. Res.* 86, pp. 6155-6169.
- Li, V.C. and Fares, N. (1986). In "Earthquake Source Mechanics" 5th Maurice Ewing Symposium, AGU, in press.
- Li, V.C. and Kisslinger, C. (1984/85). *Pure and Applied Geophys.* 122, pp. 812-830.
- Li, V.C. and Liang, E. (1986). *J. of Engineering Mechanics*, ASCE, in press.
- Li, V.C. and Rice, J.R. (1983a). *J. Geophys. Res.* 88, pp. 4231-4246.

- Li, V.C. and Rice, J.R. (1983b) *Bull Seismo. Soc. Amer.* 73
pp. 1415-1434.
- Li, V.C. and Rice, J.R. (1986). In preparation.
- Li, V.C., Seale, S.H. and Cao, T. (1986) *Tectonophysics*.
- Lisowski, M. and Prescott, W.H. (1981). *Bull. Seism. Soc. Am.* 71,
pp. 1607-1624.
- Maruyama, T. (1963). *Bull. Earthq. Res. Inst.*, Tokyo U. 41,
pp. 46-86.
- Maruyama, T. (1964). *Bull. Earthq. Res. Inst.*, Tokyo U. 42,
pp. 289-368.
- Maruyama, T. (1966). *Bull. Earthq. Res. Inst.*, Tokyo U., 44
pp. 811-71.
- Melosh, H.J. and Fleitout, L. (1982). *Geophys. Res. Lett.* 9, pp.
21-24.
- Melosh, H.J. and Raefsky, A. (1983). *J. Geophys. Res.* 88, pp.
515-526.
- Minster J. B. and Jordan, T.H. (1984). in "Tectonics and
Sedimentation along the California Margin" (Crouch, J.K. and
Bachman, S.B., eds), Pacific Section S.E.P.M., vol. 38, pp.
1-16.
- Morgenstern, N.R. and Tchalenko, J.S. (1967). *Geotechnique* 17
pp. 309-328.
- Mura, T. (1982). "Micromechanics of Defects in Solids", Martinus
Nijhoff, London.

- Muskhelishvili, N.I. (1953) "Singular Integral Equations",
translated by J.R.M. Radok, Noordhoff, Groningen.
- Nabarro, F.R. N. (1952). In "Advances in Physics, Vol. 1,
pp. 169-179.
- Nemat-Nasser, S. and Horii, H. (1982). *J. Geophys Res.* 87,
pp. 6805-6821.
- Niu, Z. (1984/5). *Pure and Applied Geophys.* 122, N.5, pp. 645-661.
- Nur, A. and Booker, J.R. (1972). *Science*, 183, pp. 204-206.
- Nur, A. and Mavko, G. (1974). *Science*, 183, pp. 204-206.
- Okubo, P. and Dieterich, J.H. (1984). *J. Geophys. Res.* 89,
pp. 5817-5827.
- Palmer, A.C. and Rice, J.R. (1973). *Proc. Roy. Soc. Lond., Ser. A*
332, 527-548.
- Papageorgiou, A.S. and Aki, K. (1983). *Bull Seis. Soc. Am.* 73,
pp. 953-978.
- Parker, A.P. (1981). "The Mechanics of Fracture and Fatigue",
E. & F.N. Spon Ltd., London.
- Parks, D.M. (1981). *Trans. ASME, J. Pressure Vessel Technol.* 103,
pp. 246-254.
- Paris, P.C. and Sih, G.C. (1965). In "Fracture Toughness Testing
and its Applications", STP 381, pp. 30-76, ASTM, Phila.
- Purcaru, G. and Berckhemer, H. (1982). *Tectonophysics*, 84,
pp. 57-128.
- Rice, J.R. (1968a). In "Fracture, An Advanced Treatise",
Vol. 2, H. Liebowitz (ed.), Academic Press, NY, pp 191-331.

- Rice, J.R. (1968b). *J. Appl. Mech.* 35, pp. 379-386.
- Rice, J.R. (1979). *Gerlands Beitr. Geophysik, Leipzig* 88, 2, S. 91-127.
- Rice, J.R. (1980). In "Physics of the Earth's Interior" (A.M. Dziewonski and E. Boschi, eds), pp. 555-649, Italian Physical Soc., No. Holland.
- Rice, J.R. (1983). *Pure and Applied Geophys.* 121. No. 3, pp. 443-475.
- Rice, J.R. (1984). *Proc. of 1st Inter. Congress on Rockbursts and Seismicity in Mines, Johannesburg, 1982, SAIMM, (Gay, N.C. and Wainwright, eds.),* pp. 57-62.
- Rice, J.R. and Cleary, M.P. (1976). *Rev. Geophys. Space Phys.*, 24, (2), pp. 227-241.
- Rice, J.R. and Levy, N. (1972). *J. Appl. Mech.* 39, 185-194, 1972.
- Rice, J.R. and Simons, D.A. (1976). *J. Geophys. Res.* 81, 5322-5334.
- Roeloffs, E. and Rudnicki, J.W. (1984/85). *Pure and Appl. Geophys.* 122, 2-4, pp. 560-582.
- Rudnicki, J.W. (1980). *Ann. Rev. Earth Planet Sci.* 8, pp. 489-525.
- Rudnicki, J.W. (1986). In "Earthquake Source Mechanics", 5th Maurice Ewing Sym., AGU, in press.
- Ruina, A. (1983). *J. Geophys. Res.* 88, pp. 10359-10370.
- Rummel, F., Alheid, H.J. and Frohn, C. (1978). *Pure and Applied Geophys.* 116, pp. 743-764.
- Rundle, J.B. (1986) *J Geophys. Res.*, Vol. 91, pp. 1947-1959.

- Rundle, J.B. and Jackson, D.D. (1977), *Geophys. J.R. Astro. Soc.* 49, pp. 575-591.
- Rybicki, K. (1971). *Bull Seis. Soc. Amer.*, 61, pp. 79-92.
- Rybicki, K. (1986). In "Continuum Theories in Solid Earth Physics" (R. Teisseyre, ed.) pp. 18-186, Elsevier, NY.
- Sacks, I.S., Suyehino, S. Linde, A.T. and Snoke, J.A. (1978). *Nature* 275, pp. 599-602.
- Sano, O. (1981). In "Fundamental Study on the Mechanisms of Brittle Fracture of Rock", D. Eng. Thesis, Kyoto Univ., Kyoto, Japan.
- Savage, J.C. and L.M. Hastie (1966). *J. Geophys. Res.* 71, pp. 4897-4904.
- Schulz, S.S., Mavko, G.M., Burford, R.O. and Stuart, W.D. (1972). *J. Geophys. Res.* 87, pp. 6977-6982.
- Sieh, K.E. (1984). *J. Geophys. Res.* 89, pp. 7641-7670.
- Skempton, A.W. (1964). *Geotechnique* 14, pp. 77-101.
- Spottiswoode, S.M. (1980). *J. Geophys. Res.*, submitted.
- Steakee, J.A. (1958a). *Can J. Phys.*, 36, pp. 192-205.
- Steakee, J.A. (1958b). *Can J. Phys.*, 36, pp. 1168-98.
- Stuart, W.D. (1979a). *Science*, 203, pp. 907-910.
- Stuart, W.D. (1979b). *J. Geophys. Res.* 84, pp. 1063-1070.
- Stuart, W.D. (1984/5). *Pure and Applied Geophys.* 122, pp. 793-811.
- Stuart, W.D., Archuleta, R.J. and Lindh, A.G. (1985). *J. Geophys. Res.* 90, pp. 592-604.

- Stuart, W.D. and Mavko, G.M. (1979). *J. Geophys. Res.* 84
pp.2153-2160.
- Tada, H., Paris, P.C. and Irwin, G. (1973). In "The Stress
Analysis of Cracks Handbook", Del Research Corp., Hellertown,
Pa.
- Thatcher, W. (1982). *Nature* 299, pp. 12-13.
- Thatcher, W. (1983). *J. Geophys. Res.* 88, pp. 5893-5902.
- Thatcher, W. (1984). *J. Geophys. Res.* 89, pp. 1867-1873.
- Thatcher, W. and Fujita, N. (1984). *J. Geophys. Res.* 89, pp.
3102-3106.
- Thatcher, W., Matsuda, T., Kato, T. and Rundle, J. B. (1980).
J. Geophys. Res. 85, pp. 6429-6439.
- Thatcher, W. and Rundle, G.B. (1979). *J. Geophys. Res.* 84, pp.
5540-5556.
- Thatcher, W. and Rundle, G.B. (1984). *J. Geophys. Res.* 89, pp.
7631-7640.
- "
Toksoz, M.N., Shakal, A.F. and Michael, A.J. (1979). *Pure Appl.
Geophys.*, 117, pp. 1258-1270.
- Tse, S.T., Dmowska, R. and Rice, J.R. (1985). *Bull. Seism. Soc.
Amer* 75, 3, pp. 709-736.
- Tse, S.T. and Rice, J.R. (1986). *J. Geophys. Res.*, in press.
- Tullis, T. and Weeks, J. (1986). In "Earthquake Source
Mechanics", 5th Maurice Ewing Symposium, AGU, in press.
- Turcotte, D. and Spence, D.A. (1974). *J. Geophys. Res.* 79,
pp.4407-4412.

- Volterra, V. (1907). *Ann. Sci. Ecole Norm. Super.*, Paris 24, pp.401-517.
- Walsh, J.B. (1969). *J. Geophys. Res.* 74 (8), pp. 2070-2080.
- Wawersik, W.R. and Brace, W.F. (1971). *Rock Mech.*, pp. 61-85.
- Wong, T.F. (1982a). *J. Geophys Res.* 87, pp. 990-1000.
- Wong, T.F. (1982b). *Mechanics of Materials 1*, pp. 3-17.
- Wong, T.F. (1986). In "Earthquake Source Mechanics", 5th Maurice Ewing Symposium, AGU, in press.
- Yip, C.K. (1979). In "Shear Strength and Deformability of Rock Joints", M.I.T. MS Thesis

TABLE CAPTIONS

- Table 1a: Slip-weakening Model Parameters for Intact Rocks.
- Table 1b: Slip-weakening Model Parameters for Sawcut Rocks.
- Table 2 : Slip-weakening Model Parameters for Rock Joints (all at room temperature).
- Table 3 : Slip-weakening Model Parameters for Over-consolidated Clay.
- Table 4 : Slip-weakening Model Parameters for Natural Faults.
- Table 5 : Green's Functions for Dislocations in Elastic, Viscoelastic and Fluid-infiltrated Poro-elastic Media.

FIGURE CAPTIONS

- Fig. 1 Tip of a shear crack in mode II and mode III deformation. The darker shade denotes an annular region in which the asymptotic crack tip stress fields given by (1) and (2) are valid.
- Fig. 2 Center crack with half crack length in an elastic plate loaded by remote shear stress σ^0 . Crack faces have uniform shear resistance σ^f .
- Fig. 3 Semi-infinite crack in mode II deformation in an elastic infinite body. Crack faces are loaded by line forces P (per unit thickness) at a distance b from crack tip.
- Fig. 4 Double edge cracks with crack lengths a and b in mode III deformation in an elastic strip loaded at the remote boundaries by thickness averaged stress σ . The thickness averaged slip displacement δ is that associated with the presence of the cracks.
- Fig. 5 Schematic illustration of the extension process of the crack tip and the associated work absorbed by relaxing the stress (1a) with simultaneous crack tip displacement (1b).
- Fig. 6 Slip rate data from a 200 km trace of the San Andreas fault in central California (after Burford and Harsh, 1980; Lisowski and Prescott, 1981; Schulz et al, 1972).

The curve fit is from the elastic brittle center-crack model (9), with coordinates origin set at 10 km west of Monarch Peak. The broad-scale geodolite data carries stronger weight because of the 2-D (thickness-averaged) nature of (9).

- Fig. 7 Tube of material cut out by contour Γ near crack tip, to illustrate the balance of energy flux into this tube of material and energy absorbed by elastic work in A, frictional work on L, and energy which drives crack extension, G.
- Fig. 8 The J-integral applied to a mode II shear crack, to relate the energy release rate G to J and the frictional dissipation.
- Fig. 9 Application of the J-integral to the San Andreas fault to extract the critical energy release rate G_c associated with the 1857 Ft. Tejon earthquake $M = 8.3$.
- Fig. 10 (a) Triaxial test results for initially intact granite samples reported in Rummel et al (1978) for three different confining pressures. (b) Slip-weakening branches deduced by Rice (1980, 1984) from raw data in (a).
- Fig. 11 Slip-weakening curves for four types of rock joints (from Goodman, 1970). Note that when slip-hardening occurs as in case 4b, the slip-weakening model and associated theories are not applicable.

Fig. 12 Schematic plot of the constitutive slip-weakening model, with (a) showing the post-peak weakening with δ , and the rigid unloading branches, and (b) showing the increase of peak strength and residual frictional strength as a function of effective normal stress, and (c) showing the decrease of peak strength and residual frictional strength as a function of temperature. Note that (b) and (c) have been drawn to illustrate the general increase followed by decrease of strength drop ($\sigma^P - \sigma^f$) with σ_n and the general decrease in strength drop with T .

Fig. 13 (a) A single-degree-of-freedom spring-block model, with loading through imposed displacement δ_0 , and load transmitted through a spring with stiffness k . (b) Trace of equilibrium loads $\sigma_A, \sigma_B, \dots, \sigma_E$, and corresponding slips $\delta_A, \delta_B, \dots, \delta_E$. Instability sets in at E, when equilibrium cannot be maintained, followed by slip acceleration and rapid stress drop rate approaching infinity, as illustrated in (c). Reestablishment of equilibrium can be at any of the points F, G or H. (d) For a stiffer spring and the same slip-weakening relationship, the unloading lines are steeper and no dynamic instability occurs. The stress may drop and the slip may accelerate as in (e), but their time rate of change do not approach infinity.

Fig. 14 (a) A single-degree-of-freedom system loaded through a standard viscoelastic element. (b) The point I represents initial instability, when the loading system is fully relaxed, with stiffness k_1 . The point D represents dynamic instability when the loading system reaches its maximum stiffness $k_1 + k_2$. Between I and D, the block is self-driven .

Fig. 15 (a) Upward progression of slip in a seismic gap zone in the elastic lithosphere of thickness H underlain by a viscoelastic foundation of thickness h . The lithosphere is treated as undergoing 2-D plane stress deformation as shown in (b) which depicts loading of the plate by σ^0 , and with (thickness averaged) stress σ and slip δ in the seismic gap zone. The σ - δ relation at the plate boundary is derived from the anti-plane strain mode III elastic brittle crack model shown in (c). The resulting 2-D problem is further reduced to a single-degree-of-freedom model by assuming that σ is uniform in the seismic gap zone.

Fig. 16 Time-dependent compliance of the coupled-plate system (solid line), and its approximation by a single parameter standard linear model (dashed line) for two seismic gap lengths.

Fig. 17 (a) Assumed fracture energy variation with depth.
(b) Thickness-averaged stress versus slip (σ - δ) relation

for elastic-brittle crack model of the antiplane rupture progression shown in Fig. 16c. Based on (18) and the fracture energy distribution as in (a). The point P represents the peak stress state and the point M represents the maximum slip possible for the σ - δ relation shown. Instability must occur between P and M.

Fig. 18 Solution of (24) for (a) crack penetration, (b) averaged stress, and (c) averaged slip, as a function of time t . The subscripts P, I, and D for the normalizing parameters denote the peak, initial instability, and dynamic instability states. Each plot shows the solution corresponding to two loading rates R .

Fig. 19 (a) Stress and slip distributions near a crack tip with a breakdown zone in which the deformation behavior is governed by the slip-weakening relation. The weakening branch is shown in (b).

Fig. 20 (a) Assumed linear variation of stress in breakdown zone (34) and (b) the corresponding slip-weakening relation, for estimation of the breakdown zone size w . After Palmer and Rice (1973).

Fig. 21 (a) Rock specimen loaded triaxially. (b) Experimental output of differential stress versus axial shortening. (c) Relation between axial relative movement of sliding surfaces and slip δ . (d) Derived slip-weakening curves from (b). From Rice (1980).

Fig. 22 Composite of critical energy release rate versus normal stress, from two test series on San Marcos gabbro and Fichtelbirge granite. After Wong (1986).

Fig. 23 (a) Nominal slip displacement ranges and (b) critical energy release rates for various geo-materials, from experimental testing and inferences from field observations.

Fig. 24 Size dependence of apparent mode I fracture toughness of various rock types on crack length in laboratory specimens. Data from Ingraffea et al (1984). The curve fits are based on numerical solution of the non-linear singular integral equation (52) by Li and Liang (1986), assuming a linear slip-weakening relation. The upper fit is for a plateau value (large crack length a) of K_{Ic} of 1200 psi $\sqrt{\text{in}}$, and the lower fit is for a plateau value of K_{Ic} of 1000 psi $\sqrt{\text{in}}$. See text for further details and also refer to Fig. 27.

Fig. 25 A general body containing a line of displacement discontinuity L . Slip δ at \underline{x}_q induces stress σ_{ij} at \underline{x}_p .

Fig. 26 Elastic plate containing a single line of displacement discontinuity with stress distribution $\sigma(x_1)$ and slip distribution $\delta(x_1)$. The plate is loaded remotely by σ^0 .

Fig. 27 Prediction of maximum applied load for the center crack plate structure shown as insert, from elastic brittle crack theory (slanted dashed line) and from strength

criteria (horizontal dashed line). The solid line is predicted by including a breakdown zone where material deforms according to a linear slip-weakening relation, and is numerically obtained by solving (52).

Fig. 28 Shear slip distribution and induced vertical ground displacement in dip slip faulting from s_1 to s_2 .

Fig. 29 (a) Comparison of observed and predicted uplift at various times prior and up to the 1971 San Fernando earthquake, based on a slip-weakening fault model with geometry shown in (b). The fault slips for various time periods are shown in (c).

Fig. 30 (a) Elastic model of tectonic plate assumed to undergo plane stress deformation, and loaded by remote stress σ^0 , with stress and slip distributions σ and δ at plate boundary. (b) A local section of the plate boundary, assumed to undergo anti-plane strain deformation. The shaded fault zone can be modelled by any appropriate constitutive law, and the resulting relation between $\sigma(x_1)$ and $\delta(x_1)$ defines the local spring constant $k(x_1)$.

Fig. 31 (a) One of several geometries of locked patches on a fault surface analyzed by Tse et al (1985) for stressing of the Parkfield region of the San Andreas fault. The lower margin of the patch has been chosen from depth of the seismicity consideration. (b) Comparison of model prediction based on the solution of (58) to geodetic slip

rate data. (c) Computed thickness averaged stress distribution along strike. From Tse et al (1985).

Fig. 32 (a) Map view of the San Andreas fault strand near Parkfield. (b) Geometry of locked patches. (c) Comparison of model prediction of fault creep at various locations shown in (a) with creepmeter data. The theoretical creep has been multiplied by 0.8 to compensate for underestimation of fault slip measured by creepmeters. From Stuart et al (1985).

Fig. 33 Computed slip rate as a function of distance along strike at various stages prior to instability, in a creep zone centered at $x_1 = \pm 2H$. Outside the creep zone, upward penetration of the brittle zone occurs with increasing tectonic loading. Note that the parabolic slip rate distribution qualitatively agrees with contemporary data, as shown in Fig. 31b, at the three earlier time steps shown. As instability approaches, the slip rate at the edge of the creep zone accelerates and exceeds that inside the creep zone. From Li and Fares (1986)

Table 1a : Slip-weakening Model Parameters for Intact Rocks

ROCK TYPES	σ_a (MPa)	T (°C)	G_c ($\times 10^4$ J/m ²)	$\sigma^p - \sigma^f$ (MPa)	$\bar{\delta}$ (mm)	w^* (m)	Reference
Witwatersrand Quartzite	14	room	0.8	50	0.15	0.21	Wong (1982) Spottiswoode (1980)
	28	room	1.3	80	0.16	0.14	
Oshima Granite	room	room	1.0	60	0.17	0.20	Wong (1982) Sano (1978)
Westerly Granite	room	room	0.7	80	0.09	0.08	Wong (1982) Wawersik & Brace (1971)
	20	room	0.6	100	0.06	0.04	
	80	room	0.3	80	0.04	0.04	
	80	150	3.3	140	0.24	0.12	Wong (1982)
	80	350	2.3	100	0.23	0.16	
	250	150	5.1	150	0.34	0.16	
	250	350	2.2	100	0.22	0.15	
	250	550	2.3	90	0.26	0.21	
	250	668	2.3	50	0.45	0.64	

ROCK TYPES	σ_3 (MPa)	σ_n (MPa)	T (°C)	G_c ($\times 10^4$ J/m ²)	$\sigma^p - \sigma^f$ (MPa)	$\bar{\delta}$ (mm)	w^* (m)	Reference
San Marcos Gabbro ⁺	250	439-500	room	1.7-1.8	107	0.25	0.17	Wong (1986)
	277	523-588		1.6-1.7	104	0.25	0.17	
	305	563-620		1.8-1.9	95	0.30	0.22	
	325	586-640		1.4-1.5	88	0.24	0.19	
	350	641-702		1.7-1.8	94	0.31	0.23	
	396	672-725		1.2	89	0.22	0.17	
	400	732-784		1.2-1.3	76	0.26	0.24	
	250	531		2.1	77	0.28	0.26	
Fichtelbirge Granite ⁺	7.5	56-100	room	0.4-0.5	25	0.21	0.59	Wong (1986) Rice (1984) Rumme1 et.al. (1978)
	17	69-139		0.5-0.6	40	0.23	0.41	
	33	121-186		0.7-0.8	38	0.23	0.43	
	55	136-243		1.9-2.0	77	0.44	0.40	
	108	253-343		1.7-1.8	123	0.37	0.21	
	157	337-440		2.5-2.6	143	0.50	0.25	
	246	498-595		3.2-3.4	133	0.56	0.30	
	300	608-715		3.0-3.2	148	0.49	0.23	

* $\mu=30$ GPa ; $\nu=0.25$ assumed

+ data corrected for constant normal stress

Table 1b : Slip-weakening Model Parameters for Sawcut Rocks

ROCK TYPES	σ_n (MPa)	T (°C)	G_c (J/m ²)	$\sigma^{p-\sigma^f}$ (MPa)	$\bar{\delta}$ (mm)	w^* (m)	Reference
Sierra White Granite smooth (0.2 μ m) rough (80 μ m)	0.6-4.0	room	0.1-1.2	0.05-0.30	0.0001-0.005	0.14-0.12	Okubo & Dieterich (1984)
	0.6-4.0	room	0.2-2.4	0.02-0.08	0.004-0.02	14-17.7	
Granodiorite Surfaces (lapped with #80 abrasive) roughness = 6 μ in	6	room	0.6	0.06	0.01	11.8	Dieterich (1979)

* $\mu = 30$ GPa ; $\nu = 0.25$ assumed

Table 2 : Slip-weakening Model Parameters for Rock Joints (all at room temp.)

ROCK TYPE	σ_n (MPa)	G_c (J/m ²)	σ^{P-f} (MPa)	$\bar{\delta}$ (nm)	w^* (m)	Reference
Summary of various rock joints experimental data	<8	18-1062	0.01-1.18	0.9 ⁺	154-6362	Yip (1979)
Coarse-grained granite (wet surfaces)	0.1-0.6	40-90	0.02-0.03	2-3 ^②	7000	Coulson (1972) Barton (1972)
Oneota Dolomite (wet surfaces)	0.1-7	18-315	0.02-0.21	0.9 ⁺	303-3180	Coulson (1972)
Bedford Limestone (wet surfaces)	0.1-7	9-428	0.01-0.42	0.9 ⁺	151-6362	
Solenhofen Limestone (wet surfaces)	0.1-8	9-72	0.01-0.08	0.9 ⁺	795-6362	
Berea Sandstone (dry surfaces)	0.1-7	18-306	0.02-0.34	0.9 ⁺	187-3181	
Berea Sandstone (wet surfaces)	0.1-7	9-306	0.01-0.34	0.9 ⁺	187-6362	

* $\mu = 30$ GPa ; $\nu = 0.25$ assumed

② inferred by Rice (1981)

+ averaged value of expt. data collected by Yip (1979)

Table 3 : Slip-weakening Model Parameters for over-consolidated clay

CLAY TYPE	σ_n (MPa)	G_c (J/m ²)	σ^p (MPa)	$\sigma^p - \sigma^f$ (MPa)	$\bar{\delta}$ (mm)	w^* (m)	Reference
Walton's Wood sample Jackfield sample London clay	0.15	69	0.076	0.035	2	0.54	Skempton (1964)
	0.11	55	0.069	0.0276	2	0.62	
	0.09	276	0.062	0.035	8	1.77	
Kaolin	0.22	56	0.083	0.017	3.3	2.01	Morgenstern & Tchalenko (1967)

* $\mu = 50 \sigma^p$ assumed

Table 4 : Slip-weakening Model Parameters for Natural Faults

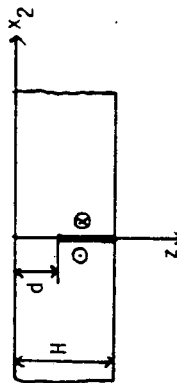
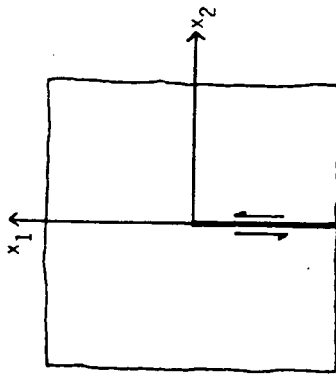
E.O. or Region	G_c (J/m ²)	$\sigma P - \sigma f$ (bars)	δ (cm)	w (km)	Method	Reference
Creep zone in central California	6.3×10^6 - 3.2×10^7	-	-	-	from geodetic slip rate and earthquake repeat time ; based on elastic brittle crack model of creep zone deformation	This study
1857 Ft.: Tejon California	7.5×10^6 - 3.8×10^7	-	-	-	from geodetic data and earthquake repeat time ; based on J-Integral analysis of creep zone deformation	Rudnicki (1981) parameters modified in this study
1976 Turkish	6.5×10^6	180	36	1.6	from seismic slip and rise time based on slip-weakening model of seismic rupture	This study
1966 Parkfield	0.8×10^6	70-105	15-23	0.34-0.77	from strong motion data, aftershock distribution and geologic evidence based on barrier model of seismic source	Aki (1979)
1857 Ft.: Tejon California	10^8	~500-700	~3-4 m	~1-2	from strong motion data, aftershock distribution and geologic evidence based on barrier model of seismic source	Aki (1979)

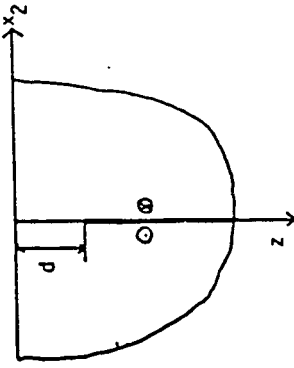
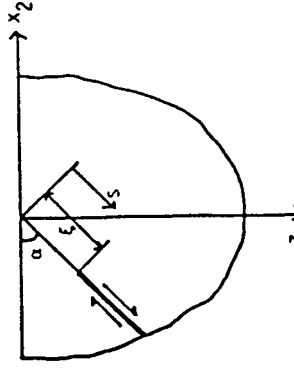
E.Q. or Region	G_c (J/m ²)	$p - \sigma_f$ (bars)	$\bar{\delta}$ (cm)	w (km)	Method	Reference
General	$< 10^7$	-	-	-	from time needed for rupture velocity to approach terminal velocity ; based on model of propagating longitudinal shear cracks	Kikuchi & Takeuchi (1970)
General	10^7	1000	10	-	from strong motion data based on cohesive force model of seismic rupture	Ida (1973)
Earthquakes from S. California & Tonga-Kermadec Arc	$1-10^6$	-	-	-	from stress drop and fault dimension ; based on dynamic shear crack model of arrest of seismic rupture	Hussein et.al. (1975)
General	10^6-10^8	-	-	-	from average rupture velocity of major earthquakes ; based on propagating shear crack model of seismic source	Das (1976)
Creep event	2.6×10^2	-	-	-	from creepmeter data based on elastic brittle crack model of aseismic creep event	Rice & Simons (1976)

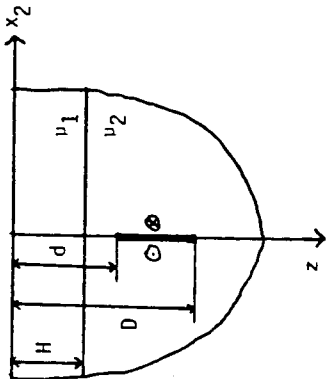
E.Q. or Region	G_c (J/m ²)	$\sigma^P - \sigma^f$ (bars)	$\bar{\delta}$ (cm)	W (km)	Method	Reference
General	4×10^6	500	9	0.1-0.2	from assumed stress drop based on anti-plane edge crack strip model of tectonic scale instability	Li & Rice (1983)
49 E.Q.	$10^5 - 10^8$	several dozen $> 10^3$	$< \text{several}$ hundred	$< \text{several}$ dozen	from seismic slip and rise time based on slip-weakening model of seismic rupture	Niu (1984/5)
1857 California	10^7	66	-	-	from creep rate and earthquake repeat time ; based on part- through crack model of plate boundary deformation	Tse et.al. (1985)
Southern San Andreas	-	100-200	50-100	-	from time and size of repeated ruptures ; based on slip-weakening model of instability sequence	Stuart (1984/85)
Five California E.Q.	$3 - 100 \times 10^6$	200-400	40-400	0.5-2	from strong ground motion observations ; based on circular crack barrier model of seismic source	Papageorgiou & Aki (1983)
S African gold mine	$10^3 - 10^6$	-	-	-	from seismic moment and slip based on cohesive force model of a propagating shear crack	Wong (1982)

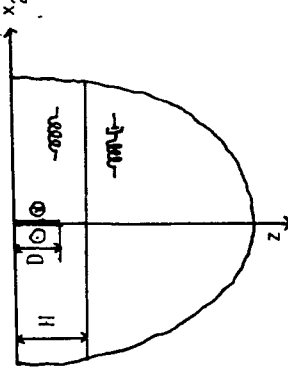
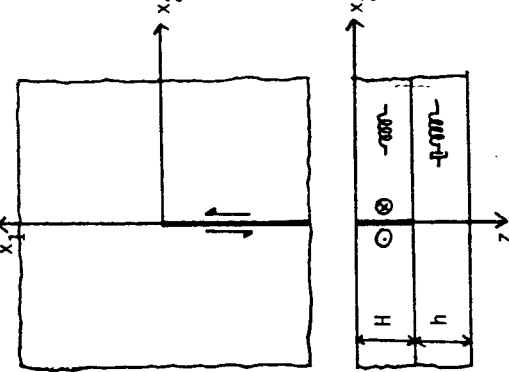
Table 5 : Green's Functions for Dislocations

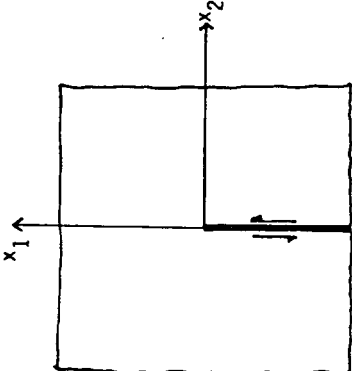
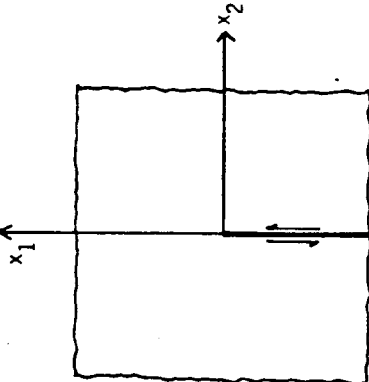
CASE	STRUCTURAL GEOMETRY AND RHEOLOGY	HOMOGENEOUS	INHOMOGENEOUS	REFERENCE
I.1	Elastic Infinite Space Edge Dislocation	<p>Infinite body : plane strain</p> $\frac{\mu}{2\pi(1-\nu)} \cdot \frac{1}{x_1}$ <p>Plate : plane stress</p> $\frac{\mu(1+\nu)}{2\pi} \cdot \frac{1}{x_1}$		Hirth & Lothe (1968) Nabarro (1952)
I.2				
I.3	Elastic Infinite Strip Screw Dislocation	$-\frac{\mu}{2H} \frac{\sin \frac{\pi d}{H}}{\left[\cos \frac{\pi d}{H} - \cos \frac{\pi z}{H} \right]}$	$-\frac{\mu}{2\pi} \frac{1}{z-d}$ $+\frac{\mu}{2\pi} \left[\frac{1}{z+d} + \sum_{m=1}^{\infty} \left[\frac{1}{d-2mH-z} + \frac{1}{d-2mH+z} \right] \right]$	Tse, et al (1985) Derived from Rybicki (1971)



CASE	STRUCTURAL GEOMETRY AND RHEOLOGY	HOMOGENEOUS	INHOMOGENEOUS	REFERENCE
I.4	<p>Elastic Half-space Screw Dislocation</p> 	$-\frac{\mu}{2\pi} \frac{1}{z-d}$	$\frac{\mu}{2\pi} \frac{1}{z+d}$	<p>Derived from Chinnery & Jovanovich (1972)</p>
I.5	<p>Elastic Half-space ... Dip Slip</p> 	$\frac{\mu}{2\pi(1-\nu)} \xi \cdot s$	$-\frac{\mu}{2\pi(1-\nu)} \left[\frac{\sum_{n=0}^5 \lambda_n s^{n-5-n}}{(\xi^2 + s^2 - 2\xi s \cos 2\alpha)^3} \right]$ <p> $\lambda_0 = 1$ $\lambda_1 = -1 - 6\cos 2\alpha + 2\cos^2 2\alpha$ $\lambda_2 = 6 - 2\cos 2\alpha + 6\cos^2 2\alpha$ $\lambda_3 = -6\cos 2\alpha - 4\cos^3 2\alpha$ $\lambda_4 = -3 + 2\cos 2\alpha + 6\cos^2 2\alpha$ $\lambda_5 = 1 - 2\cos^2 2\alpha$ </p>	<p>Freund & Barnett (1976a,b) Dmowska & Kostrov (1973) Head (1953)</p>

CASE	STRUCTURAL GEOMETRY AND RHEOLOGY	HOMOGENEOUS	INHOMOGENEOUS	REFERENCE
I.6	<p data-bbox="284 1344 349 1668">Elastic Layered Half-space Screw Dislocation</p> 	<p data-bbox="251 1052 300 1220">For $d \geq H, D > H$</p> $z \geq H$ $\frac{\nu_2}{2\pi} \left[\frac{1}{z-D} - \frac{1}{z-d} \right]$ <p data-bbox="885 1064 933 1220">For $d < H, D \leq H$</p> $z \leq H$ $\frac{\nu_1}{2\pi} \left[\frac{1}{z-D} - \frac{1}{z-d} \right]$	$\gamma = \frac{\nu_2}{\nu_1}$ $z \leq H$ $\frac{\nu_1 \gamma}{\pi(1+\gamma)} \left[\frac{1}{z-D} - \frac{1}{z-d} - \frac{1}{z+D} + \frac{1}{z+d} \right]$ $+ \sum_{m=1}^{\infty} \left(\frac{1-\gamma}{1+\gamma} \right)^m \left[-\frac{1}{D+2mH+z} + \frac{1}{d+2mH-z} - \frac{1}{D+2mH+z} + \frac{1}{d+2mH+z} \right]$ $z \geq H$ $\frac{\nu_2}{2\pi} \left[\frac{\gamma-1}{\gamma+1} \left[-\frac{1}{D-2H+z} + \frac{1}{d-2H+z} \right] - \frac{4\gamma}{(1+\gamma)^2} \left[-\frac{1}{D+z} + \frac{1}{d+z} \right] \right]$ $+ \sum_{m=1}^{\infty} \left(\frac{1-\gamma}{1+\gamma} \right)^m \left[-\frac{1}{D+2mH+z} + \frac{1}{d+2mH+z} \right]$ $z \leq H$ $\frac{\nu_1}{2\pi} \left[-\frac{1}{z+D} + \frac{1}{z+d} + \sum_{m=1}^{\infty} \left(\frac{1-\gamma}{1+\gamma} \right)^m \left[-\frac{1}{D-2mH-z} + \frac{1}{d-2mH+z} - \frac{1}{D+2mH-z} + \frac{1}{d+2mH+z} \right] \right]$	Derived from Rybicki (1971)

CASE	STRUCTURAL GEOMETRY AND RHEOLOGY	HOMOGENEOUS	INHOMOGENEOUS	REFERENCE
II.1	<p>Elastic Layer Overlying Maxwell Viscoroelastic Half-space. Screw Dislocation (D&H)</p> 	$\frac{\mu}{2\pi} \frac{1}{z-D}$	$\frac{\mu}{2\pi} \left[-\frac{1}{z+D} + \sum_{m=1}^{\infty} \left[1 - \exp\left(-\frac{t}{\tau}\right) \sum_{k=0}^{m-1} \frac{(t/\tau)^k}{k!} \right] \left[\frac{1}{z-2mH-D} - \frac{1}{z-2mH+D} + \frac{1}{z+2mH-D} - \frac{1}{z+2mH+D} \right] \right]$ <p>where $\tau = \frac{2\eta}{\mu}$</p>	Bonafede et al (1986)
II.2	<p>Elastic Layer Overlying Maxwell Viscoroelastic Layer. (modified Eissner Model) Edge Dislocation.</p> 	$\frac{\mu}{2\pi}(1+\nu) \gamma(x_1, t) \text{ where}$ $\gamma(x_1, t) = \lambda_0 \exp\left(-\frac{\alpha t}{\beta}\right) \left[K_1(x_1 \lambda_0) + \sum_{\nu=1}^{\infty} \frac{(x_1 \lambda_0 \alpha t / \beta)^{\nu}}{2^{\nu} (\nu!)^2} K_{\nu+1}(x_1 \lambda_0) \right]$ <p>$\lambda_0 = 1/H$ K_1 = modified Bessel function $\beta = \left(\frac{\pi}{4}\right) H^2$ $\alpha = \frac{hH\mu}{\eta}$</p>	<p>HOMOGENEOUS</p>	Lehner, Li & Rice (1981)

CASE	STRUCTURAL GEOMETRY AND RHEOLOGY	HOMOGENEOUS	REFERENCE
III.1	<p data-bbox="266 1306 341 1685">Poroelastic Infinite Space with Permeable Slip Plane. Edge Dislocation</p> 	$\frac{\mu}{2\pi(1-\nu_u)x_1} \left[1 - \frac{\nu_u - \nu}{1-\nu} \frac{4ct}{x_1^2} \left[1 - \exp\left(-\frac{x_1^2}{4ct}\right) \right] \right]$ <p data-bbox="487 1149 511 1212">where</p> <p data-bbox="519 744 544 1149">c = coefficient of consolidation</p> <p data-bbox="552 829 576 1149">ν = drained Poisson ratio</p> <p data-bbox="584 808 625 1149">ν_u = undrained Poisson ratio</p>	Rice & Cleary (1976)
III.2	<p data-bbox="777 1306 852 1685">Poroelastic Infinite Space with Impermeable Slip Plane. Edge Dislocation</p> 	$\frac{\mu}{2\pi(1-\nu_u)x_1} \left[1 - \frac{\nu_u - \nu}{1-\nu} \left[2 \exp\left(-\frac{x_1^2}{4ct}\right) - \frac{4ct}{x_1^2} \left[1 - \exp\left(-\frac{x_1^2}{4ct}\right) \right] \right] \right]$ <p data-bbox="1031 1159 1055 1223">where</p> <p data-bbox="1063 766 1088 1159">c = coefficient of consolidation</p> <p data-bbox="1096 851 1120 1159">ν = drained Poisson ratio</p> <p data-bbox="1128 829 1169 1159">ν_u = undrained Poisson ratio</p>	Rudnicki (1986)

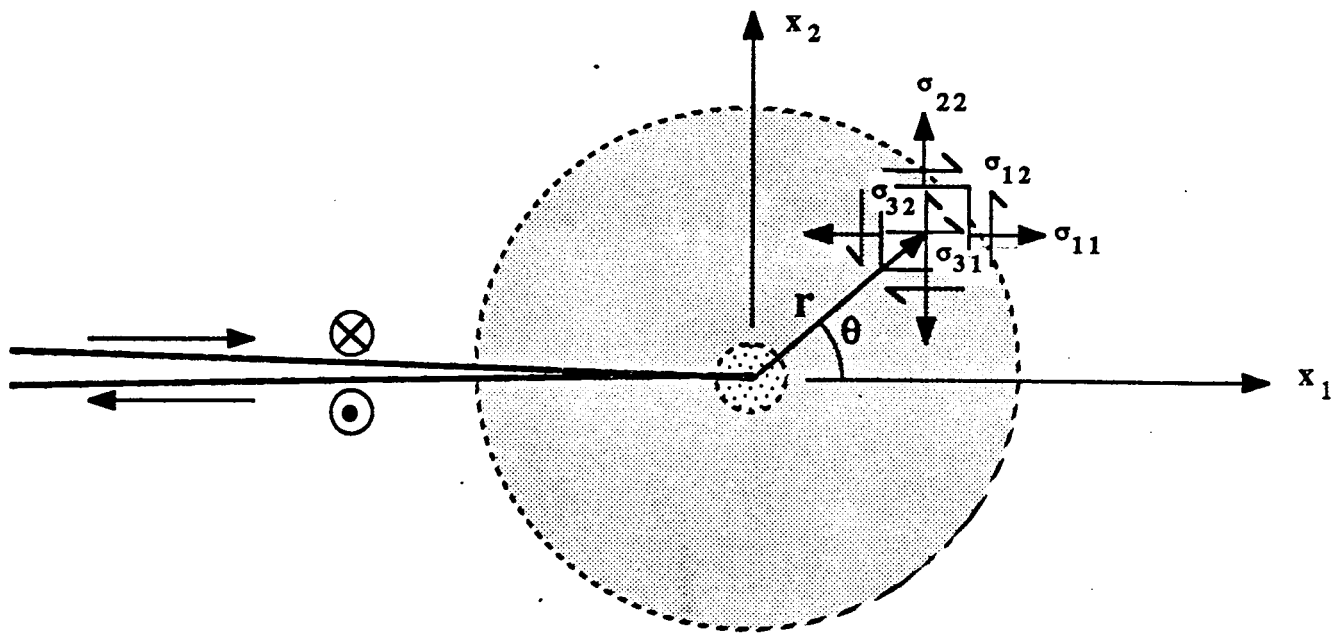


Figure 1

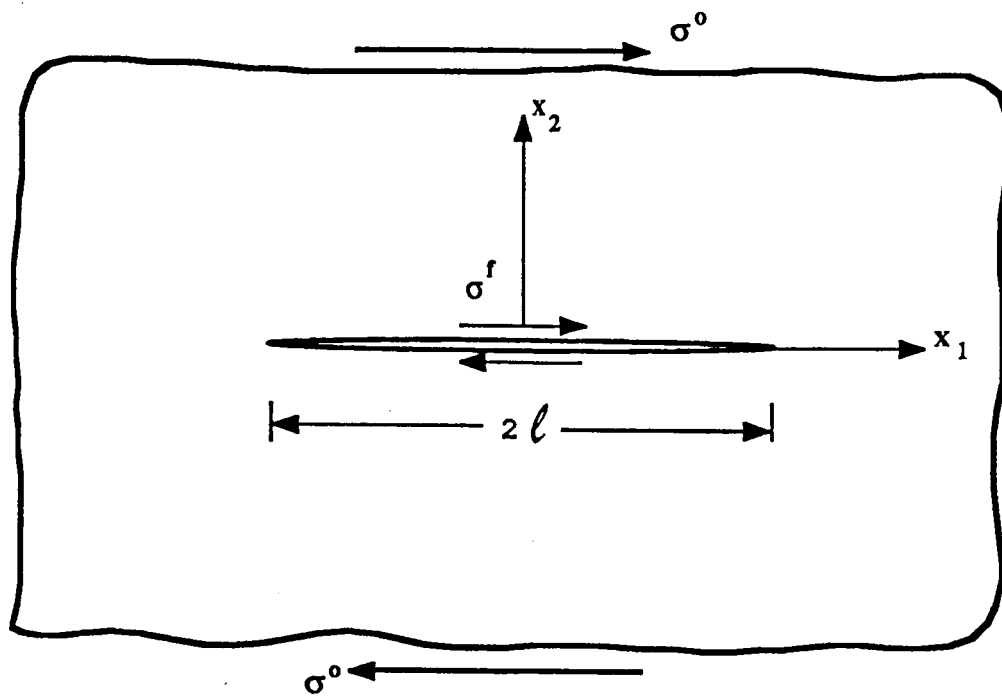


Figure 2

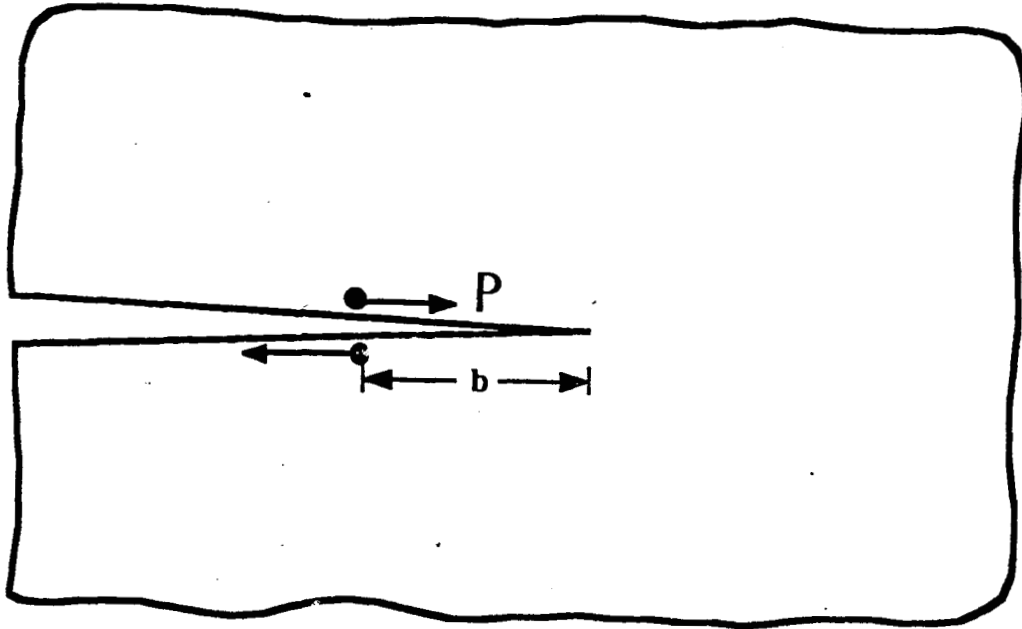


Figure 3

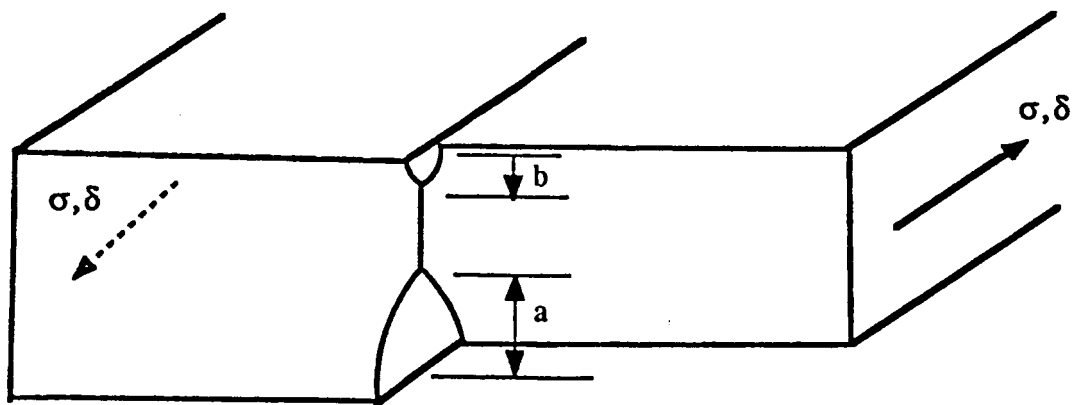


Figure 4

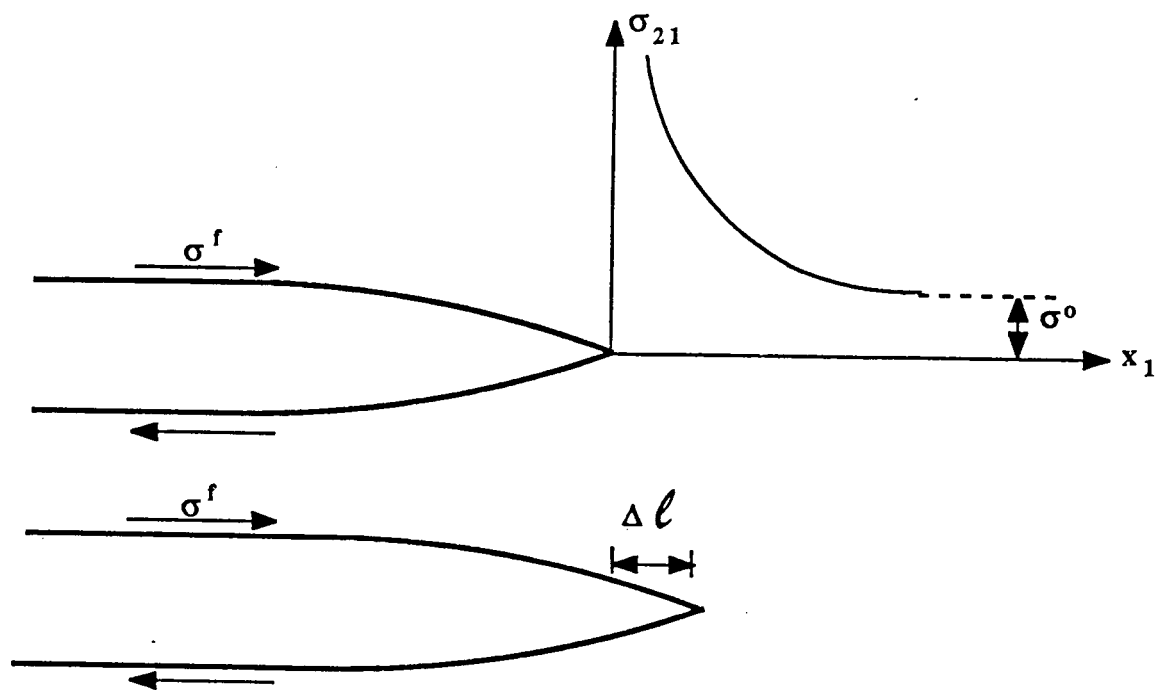


Figure 5

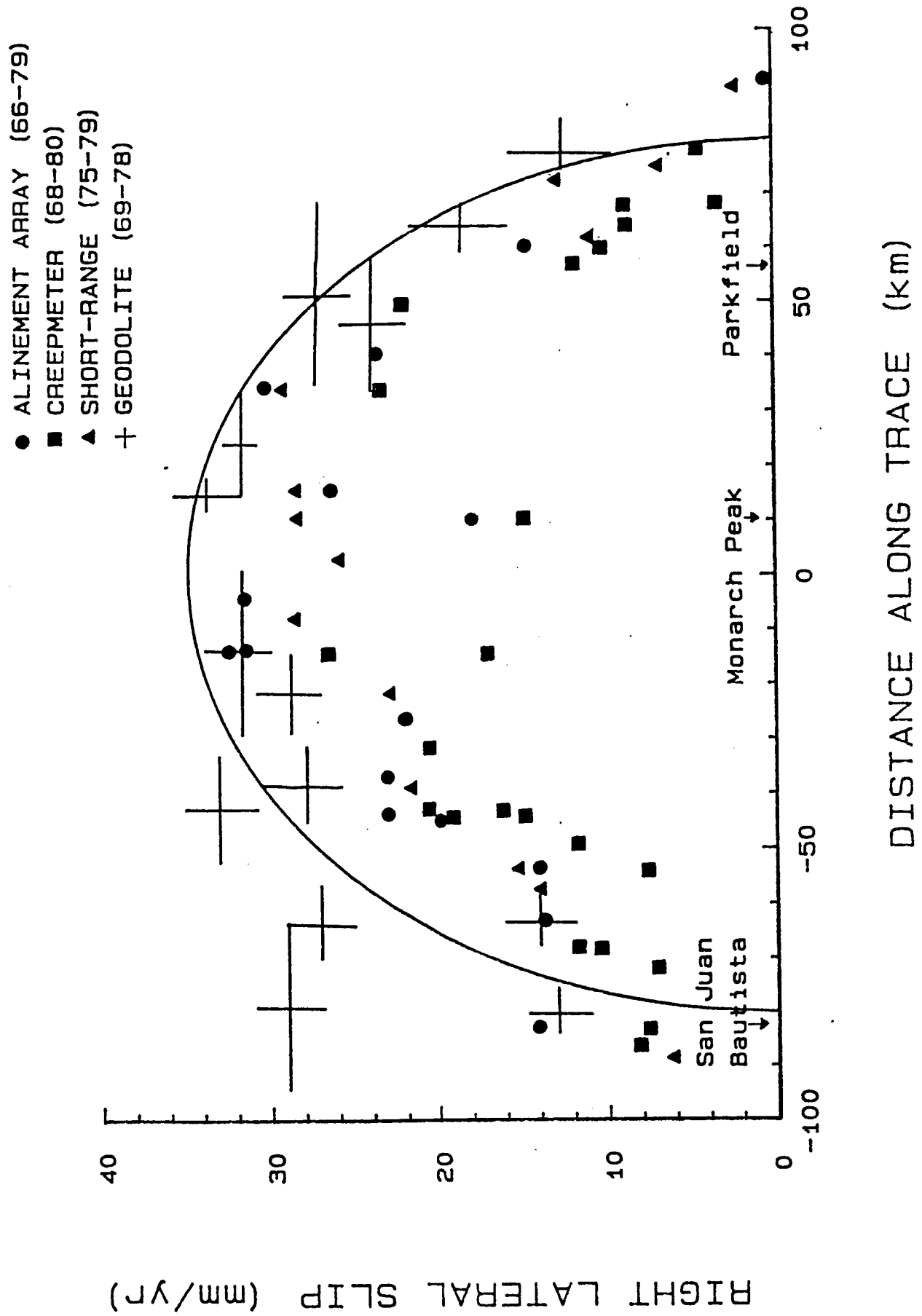


Figure 6

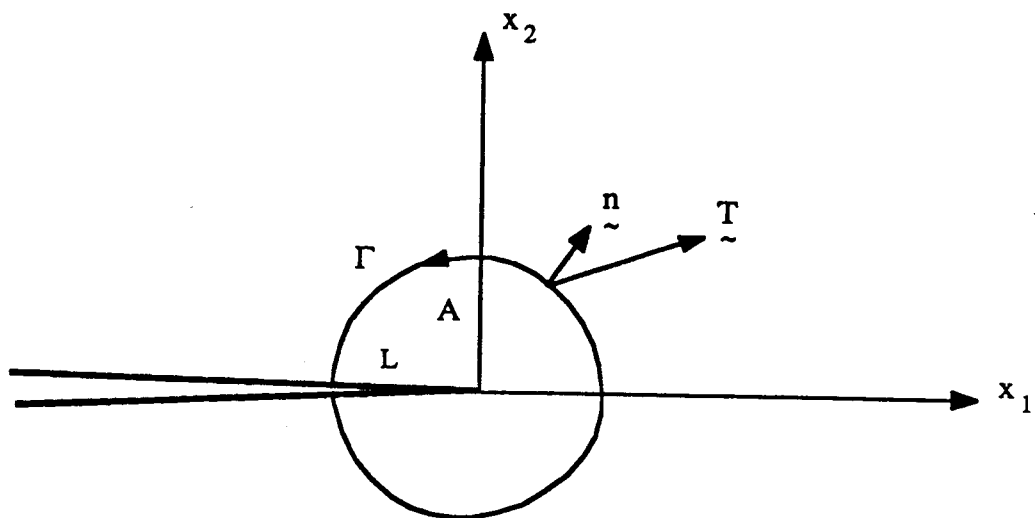


Figure 7

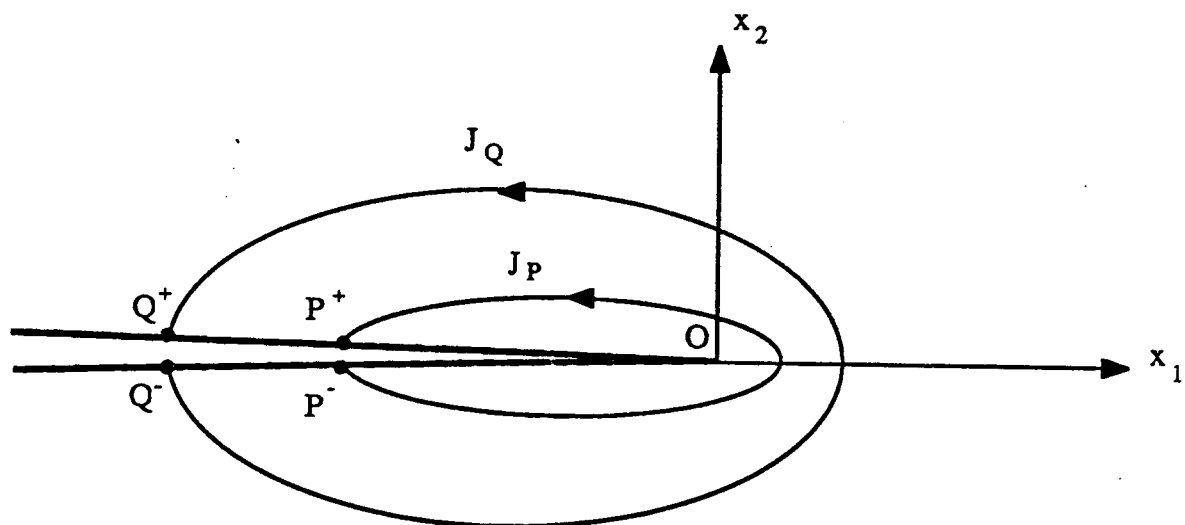


Figure 8

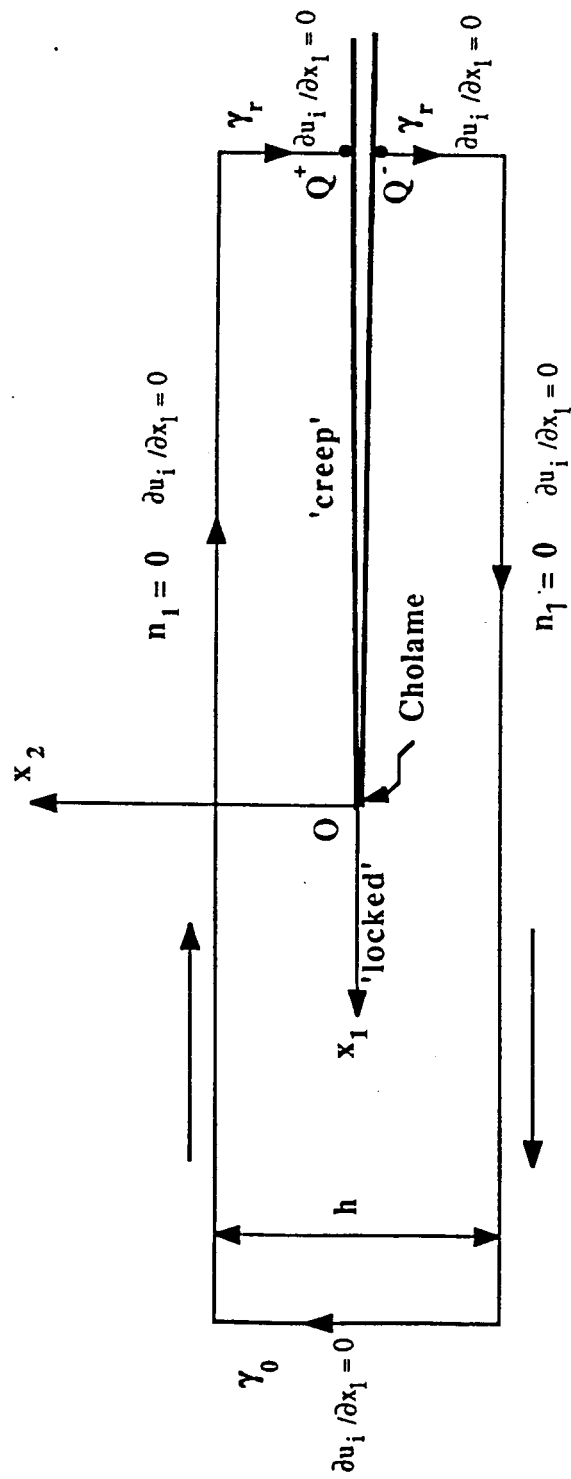


Figure 9

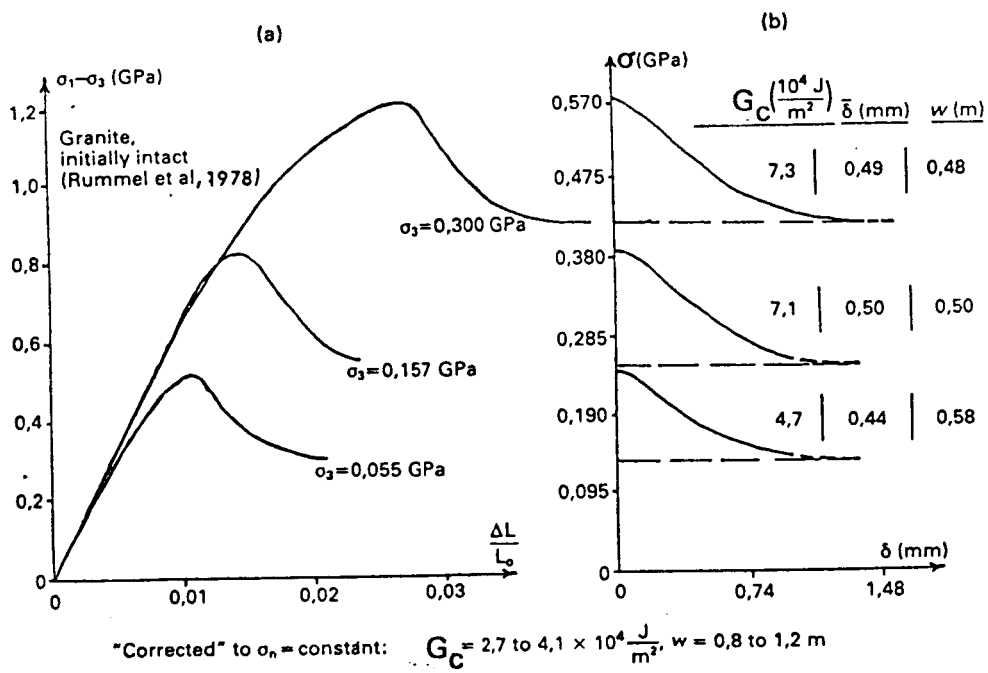
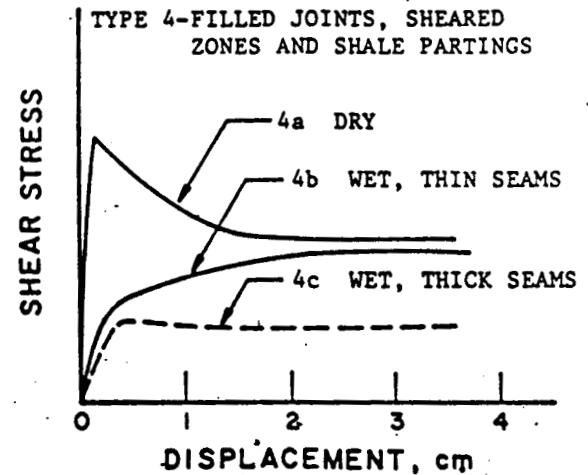
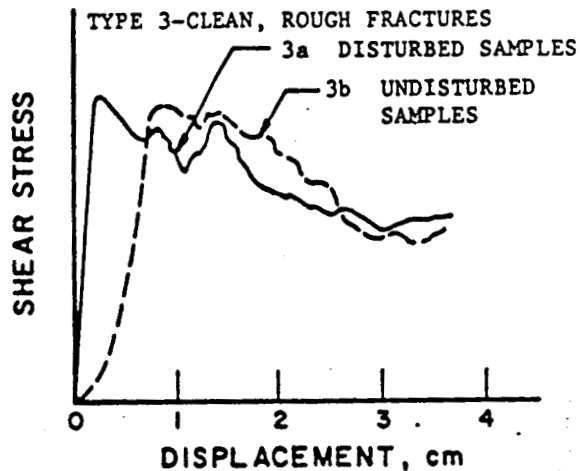
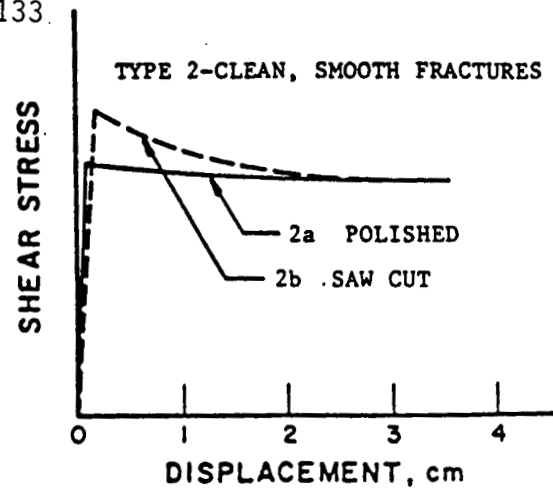
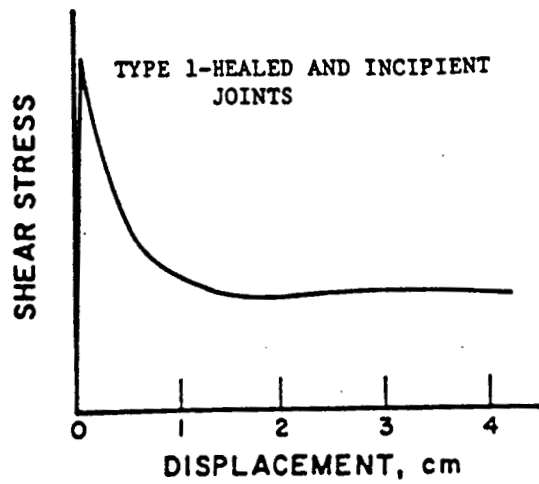


Figure 10



TYPE	TYPE OF SURFACES TYPICALLY EXHIBITING BEHAVIOR IN THIS CLASS
1	HEALED JOINTS AND INCIPIENT JOINTS
2	CLEAN, SMOOTH FRACTURES
	2a POLISHED
	2b UNPOLISHED (ROUGH SAW CUT)
3	CLEAN, ROUGH FRACTURES
	3a ARTIFICIAL EXTENSION FRACTURES AND DISTURBED SAMPLES
	3b UNDISTURBED SAMPLES
4	FILLED JOINTS, SHEARED ZONES, SHALE PARTINGS, AND SMOOTH BEDDING
	4a DRY OR SLIGHTLY MOIST
	4b WET; THIN SEAM
	4c WET; THICK SEAM

Figure 11

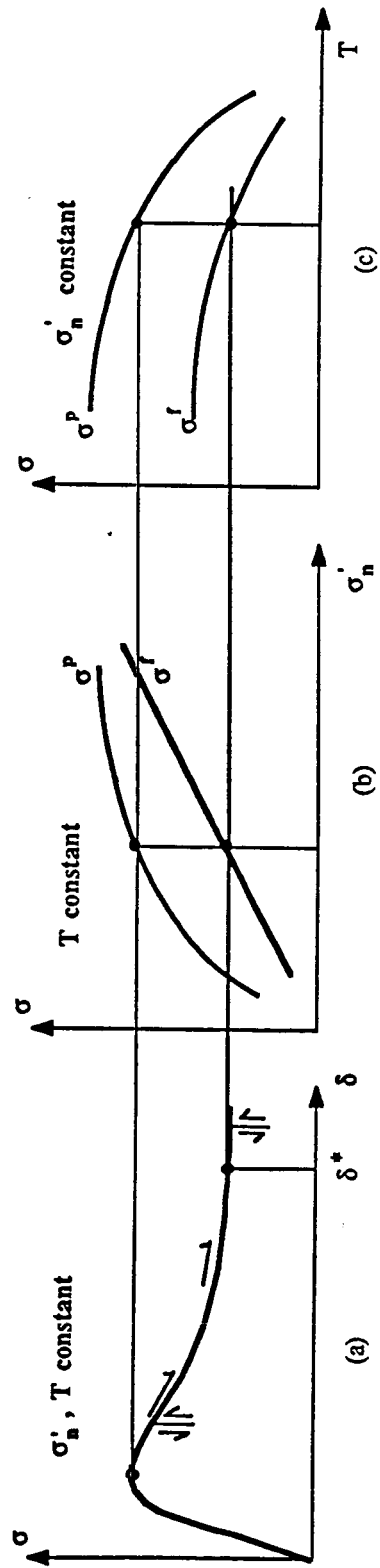


Figure 12

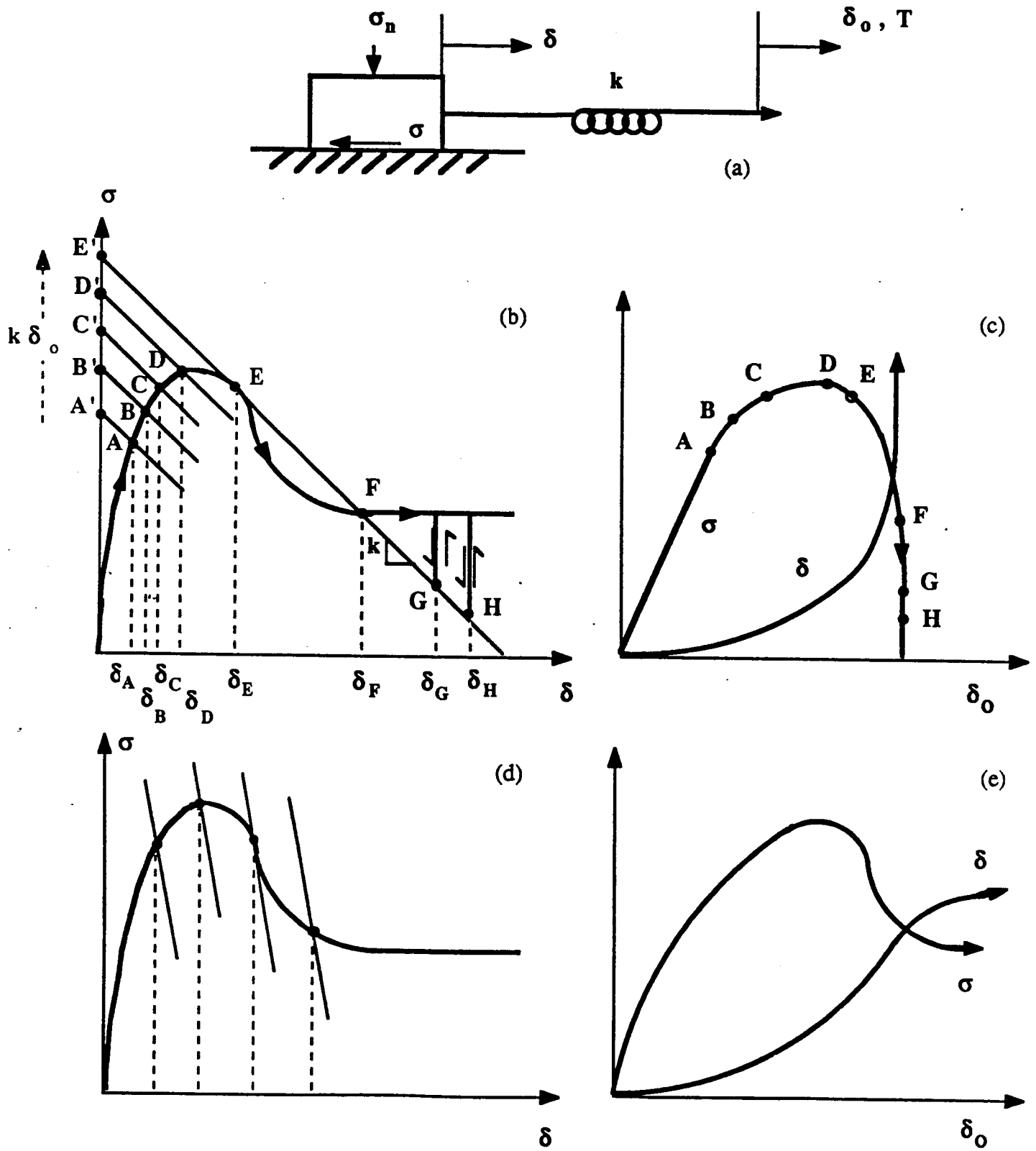


Figure 13

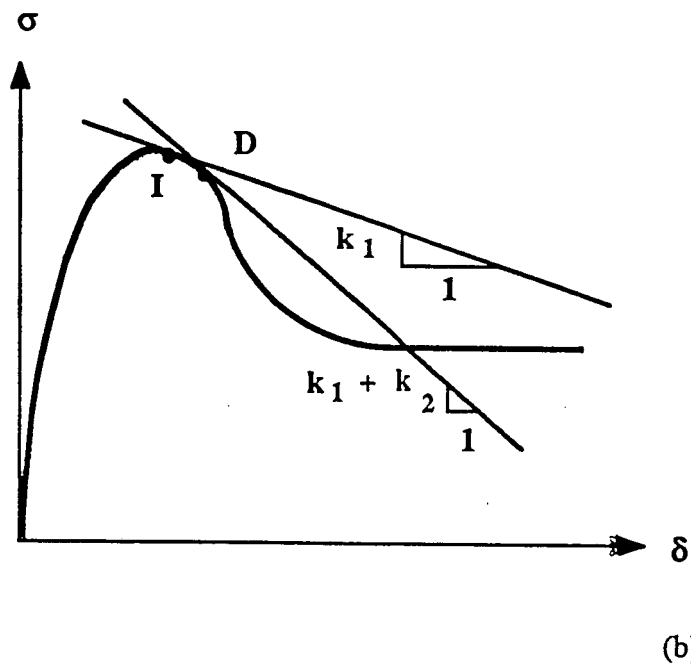
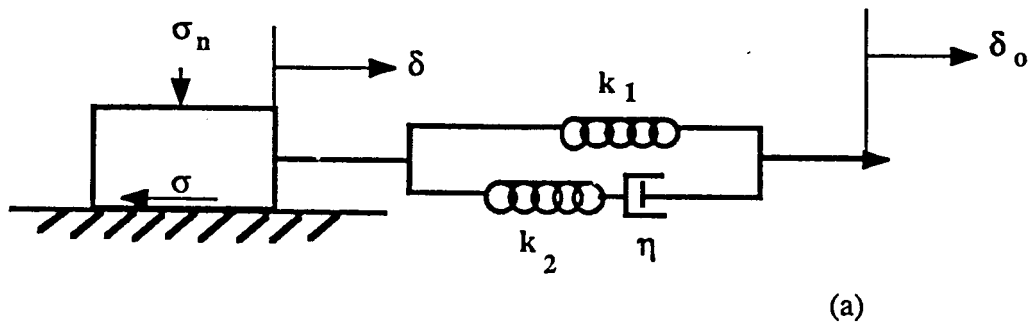


Figure 14

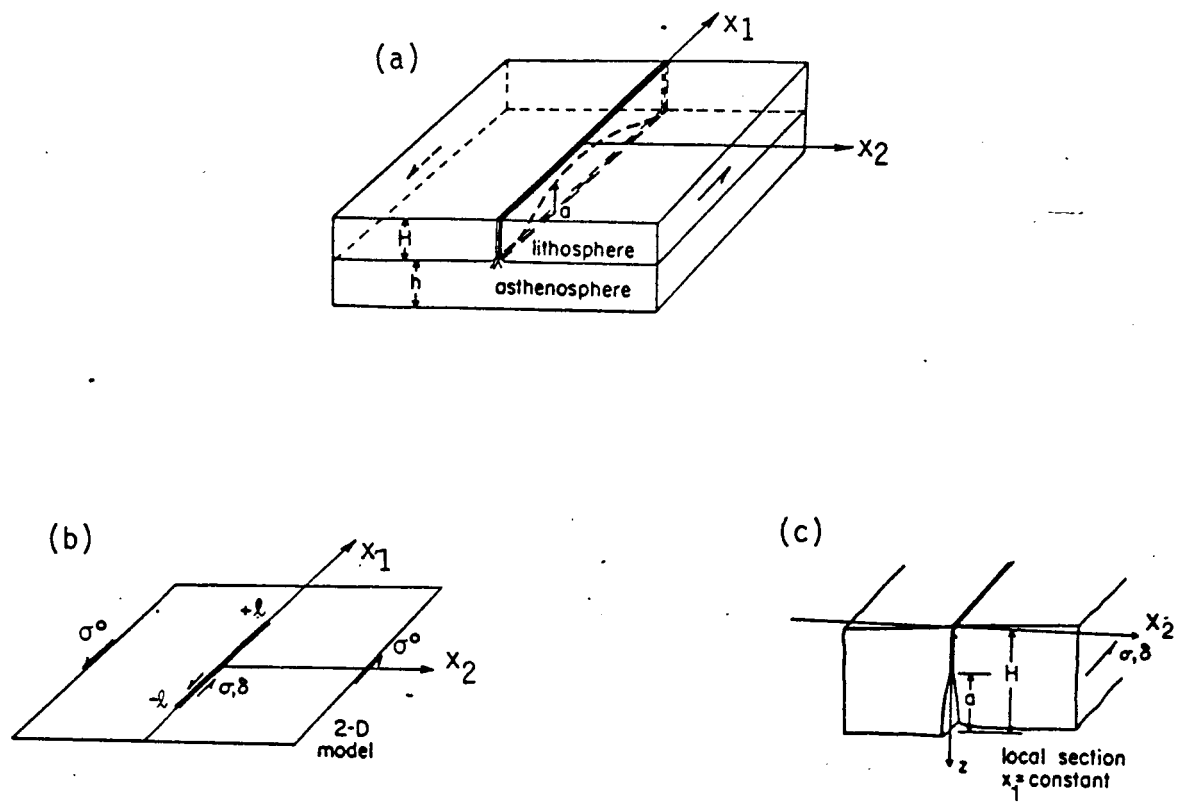


Figure 15

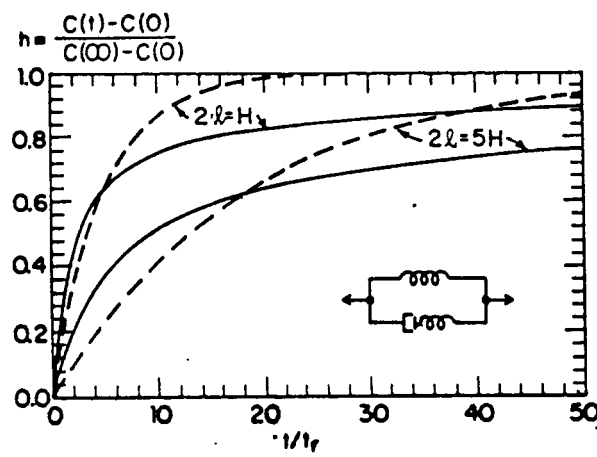
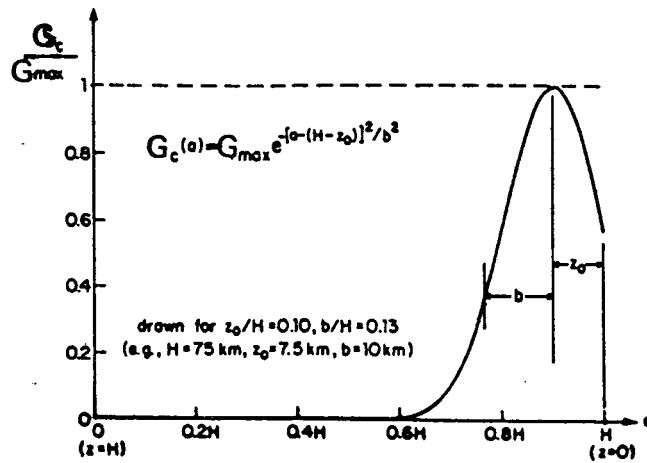
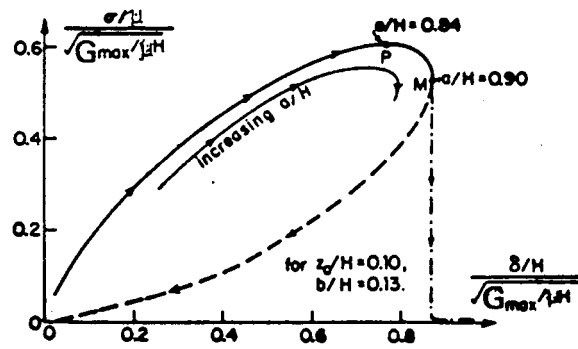


Figure 16

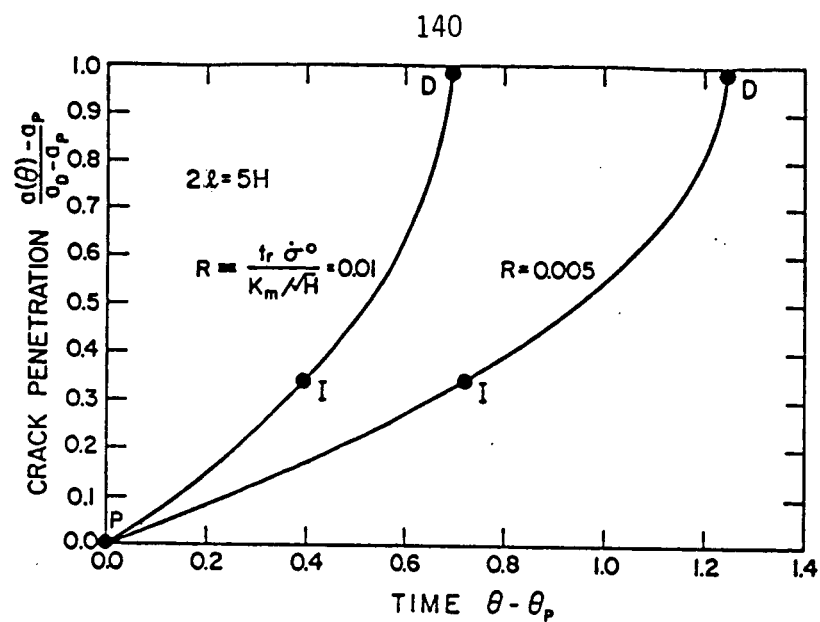


(a)

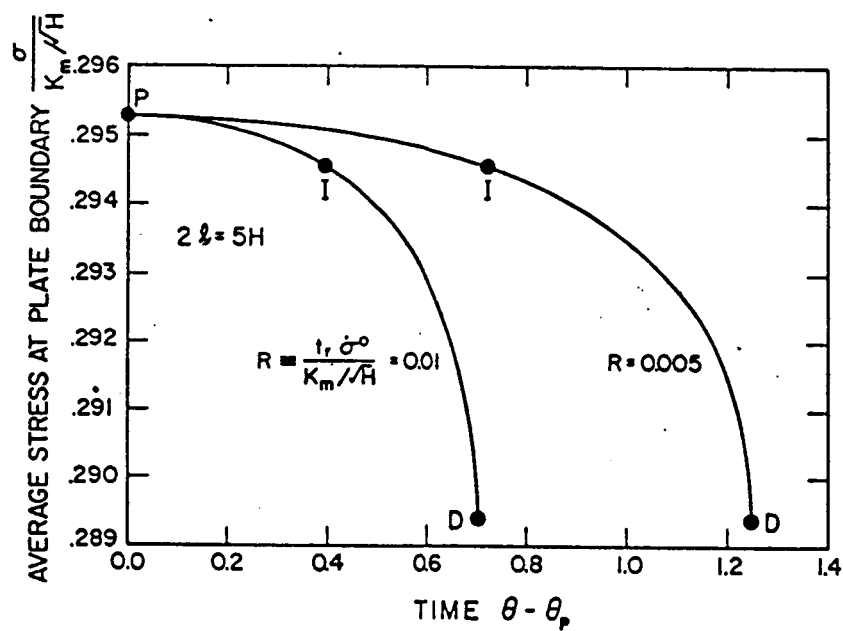


(b)

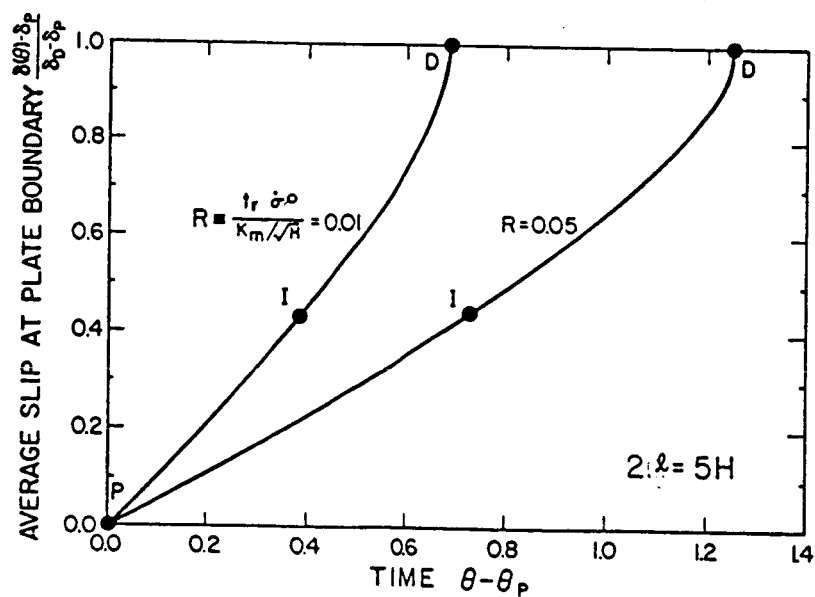
Figure 17



(a)



(b)



(c)

Figure 18

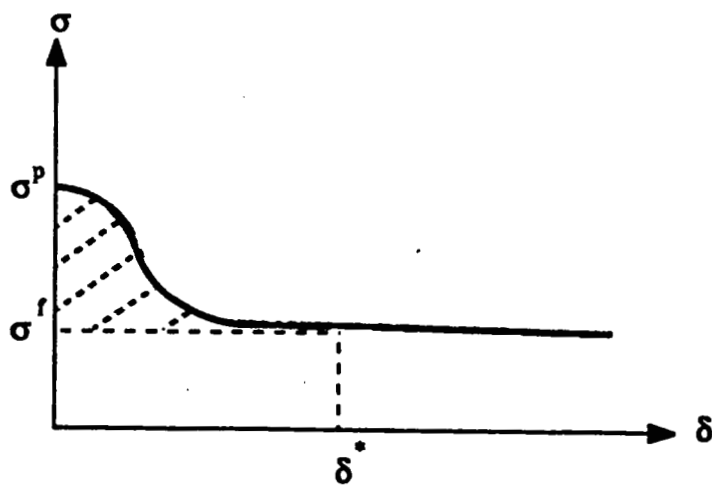
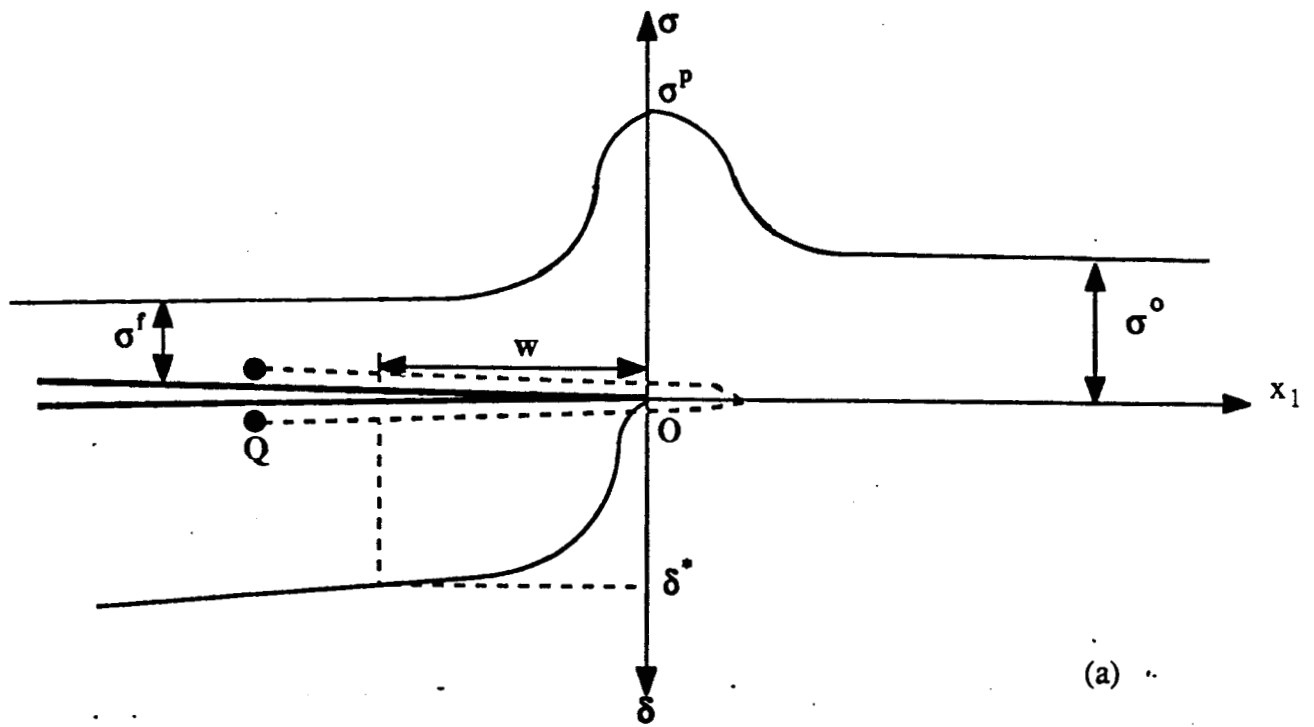


Figure 19

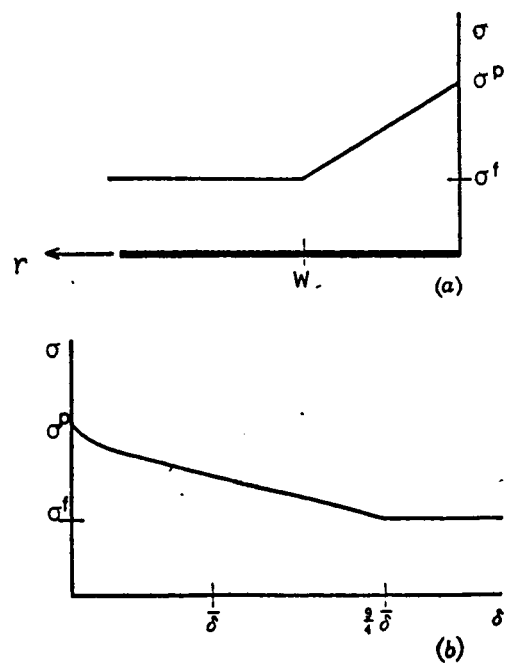


Figure 20

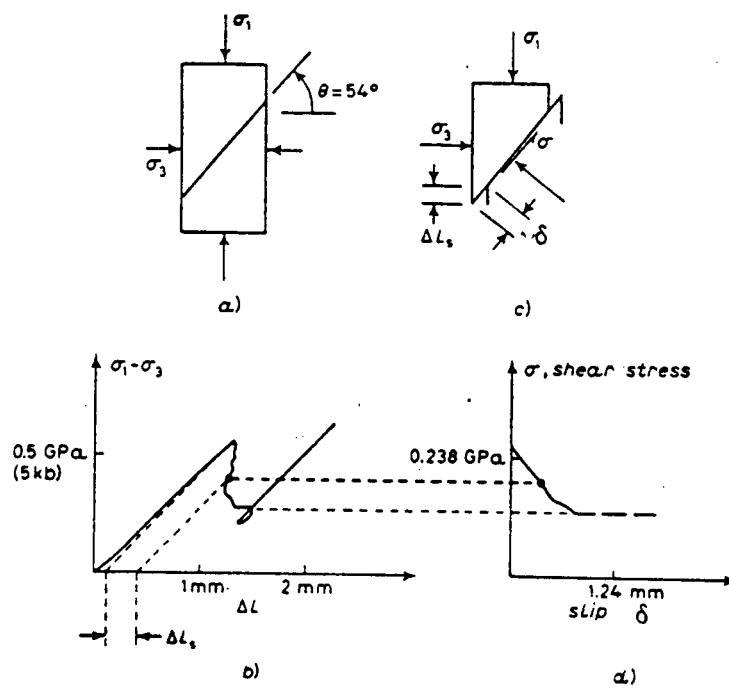


Figure 21

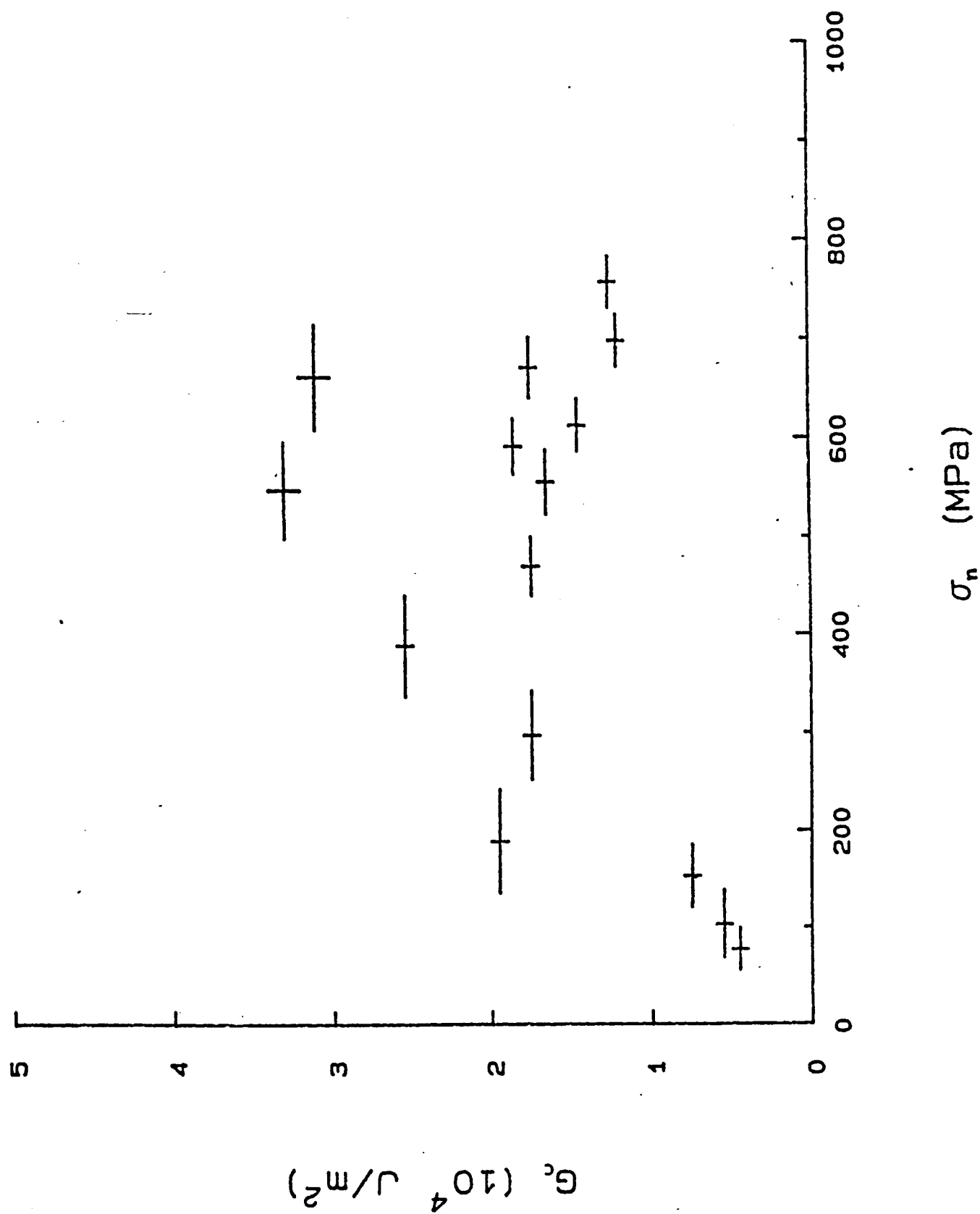


Figure 22

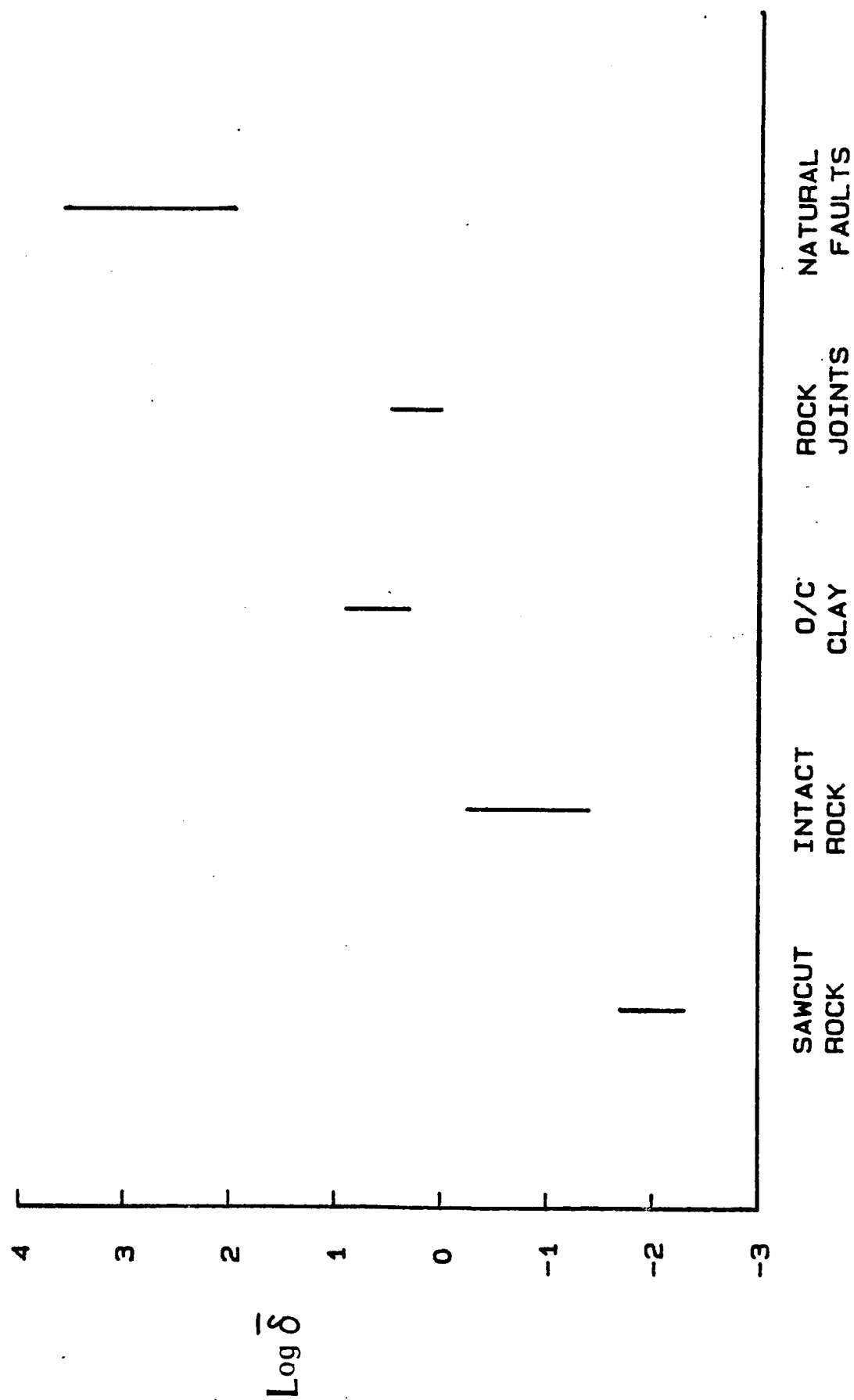


Figure 23a

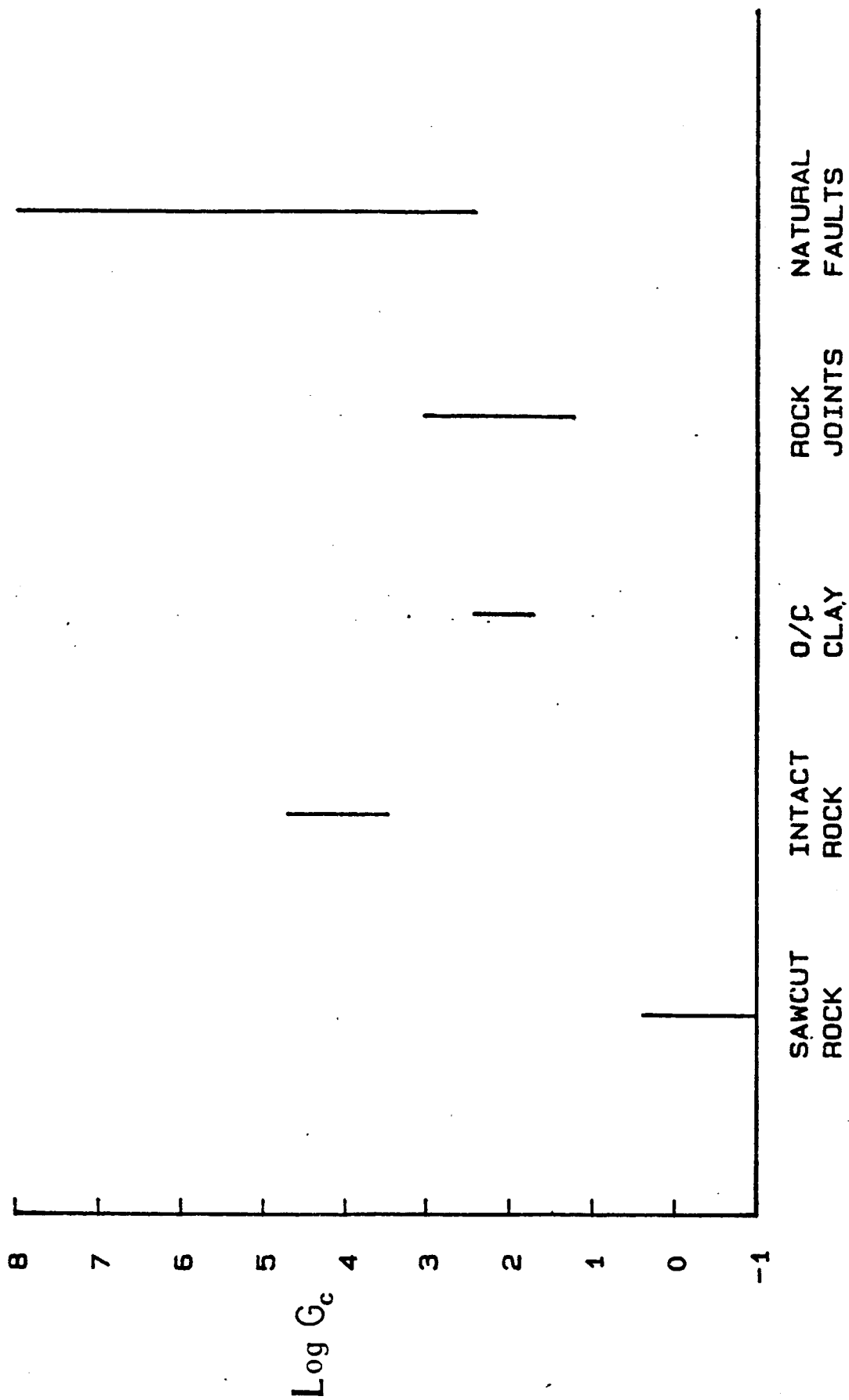


Figure 23b

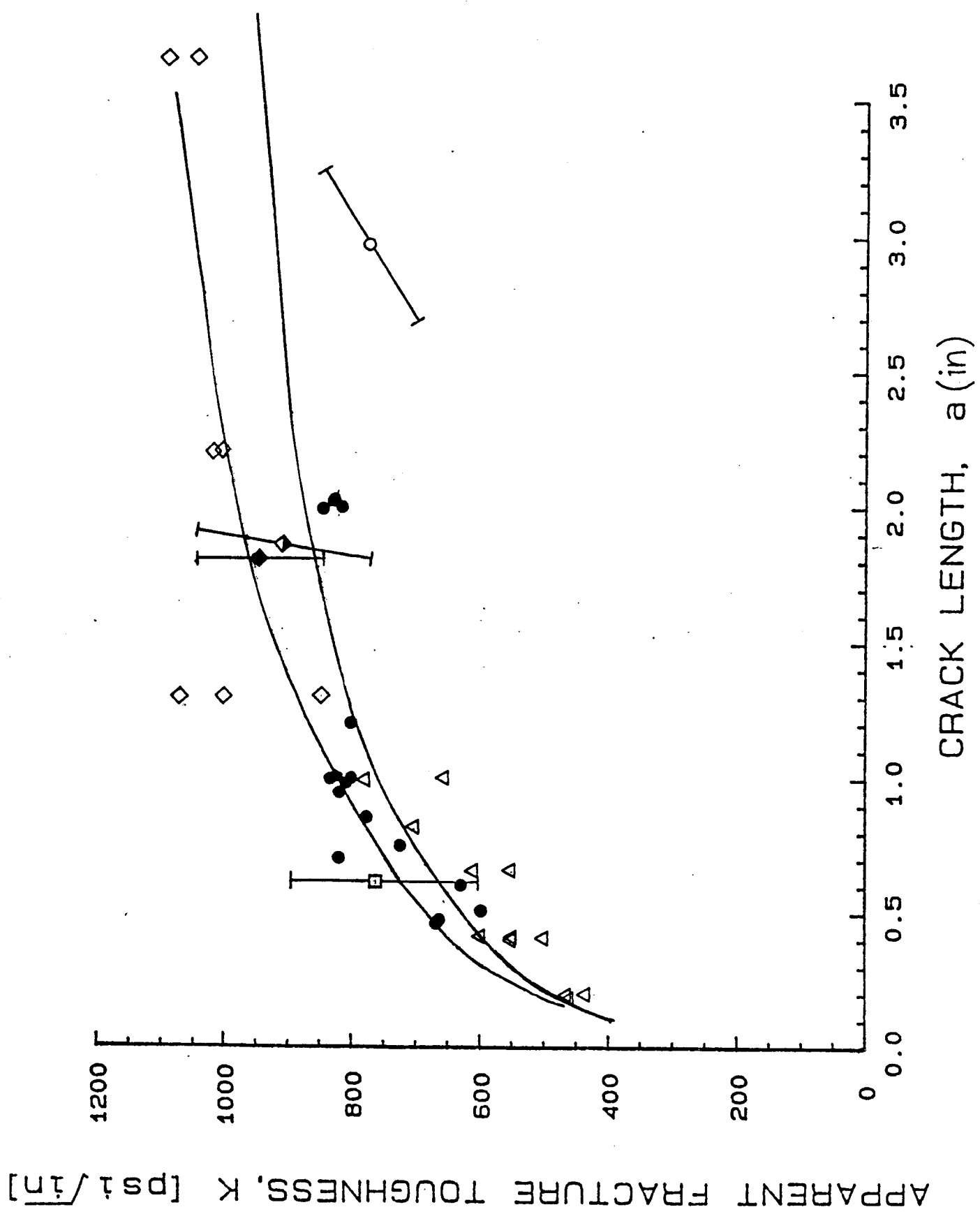


Figure 24

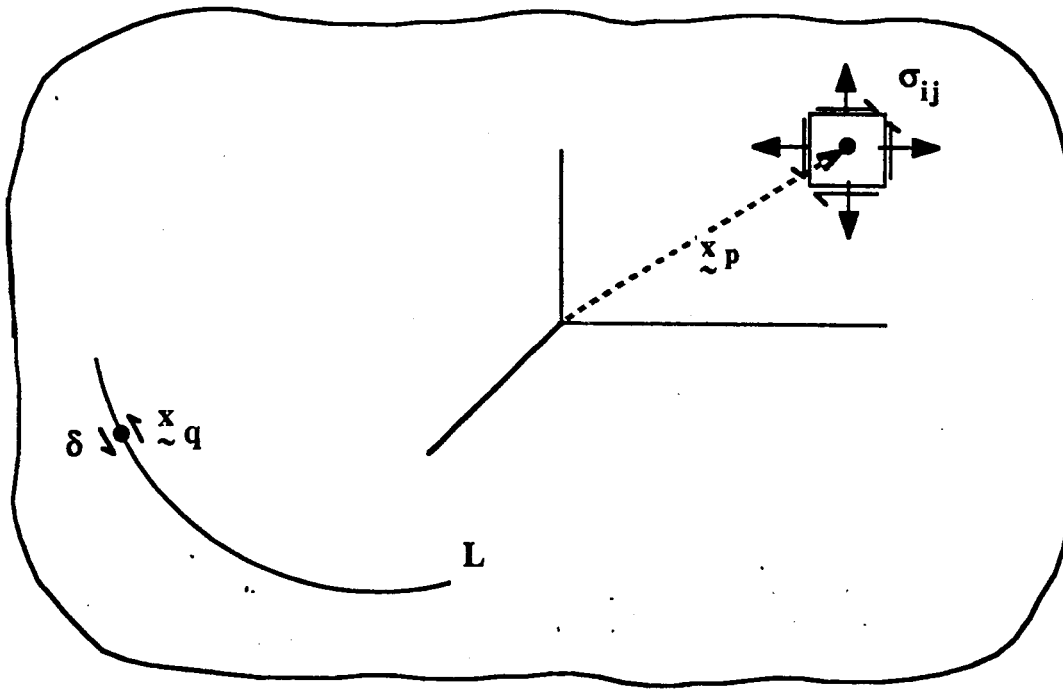


Figure 25

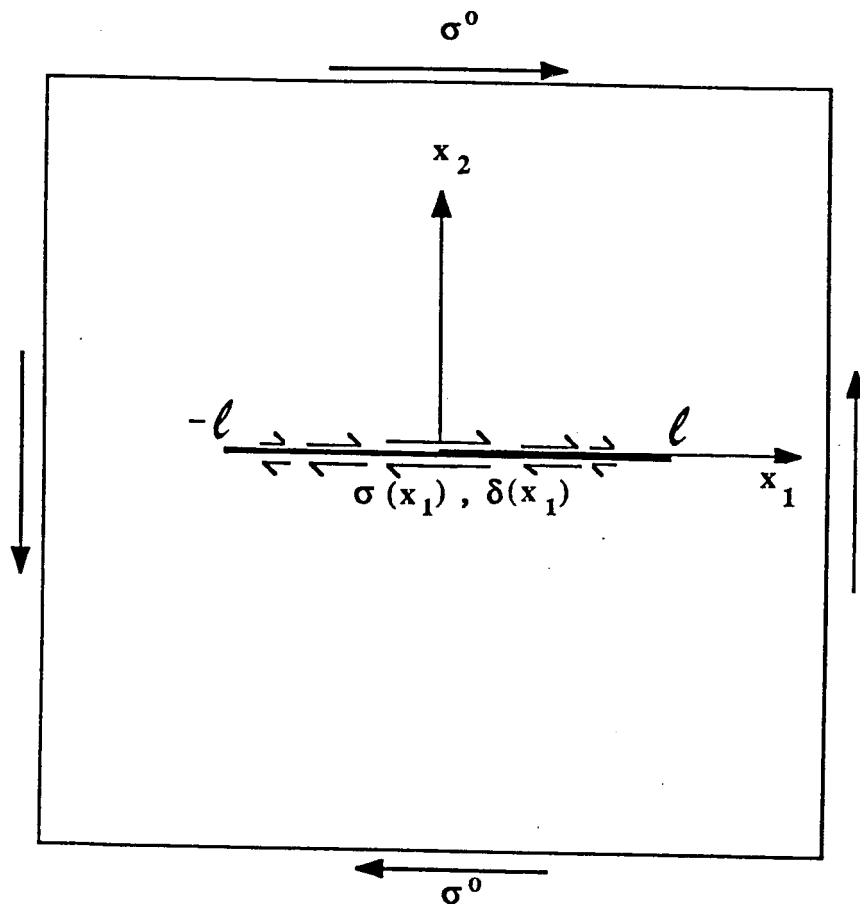


Figure 26

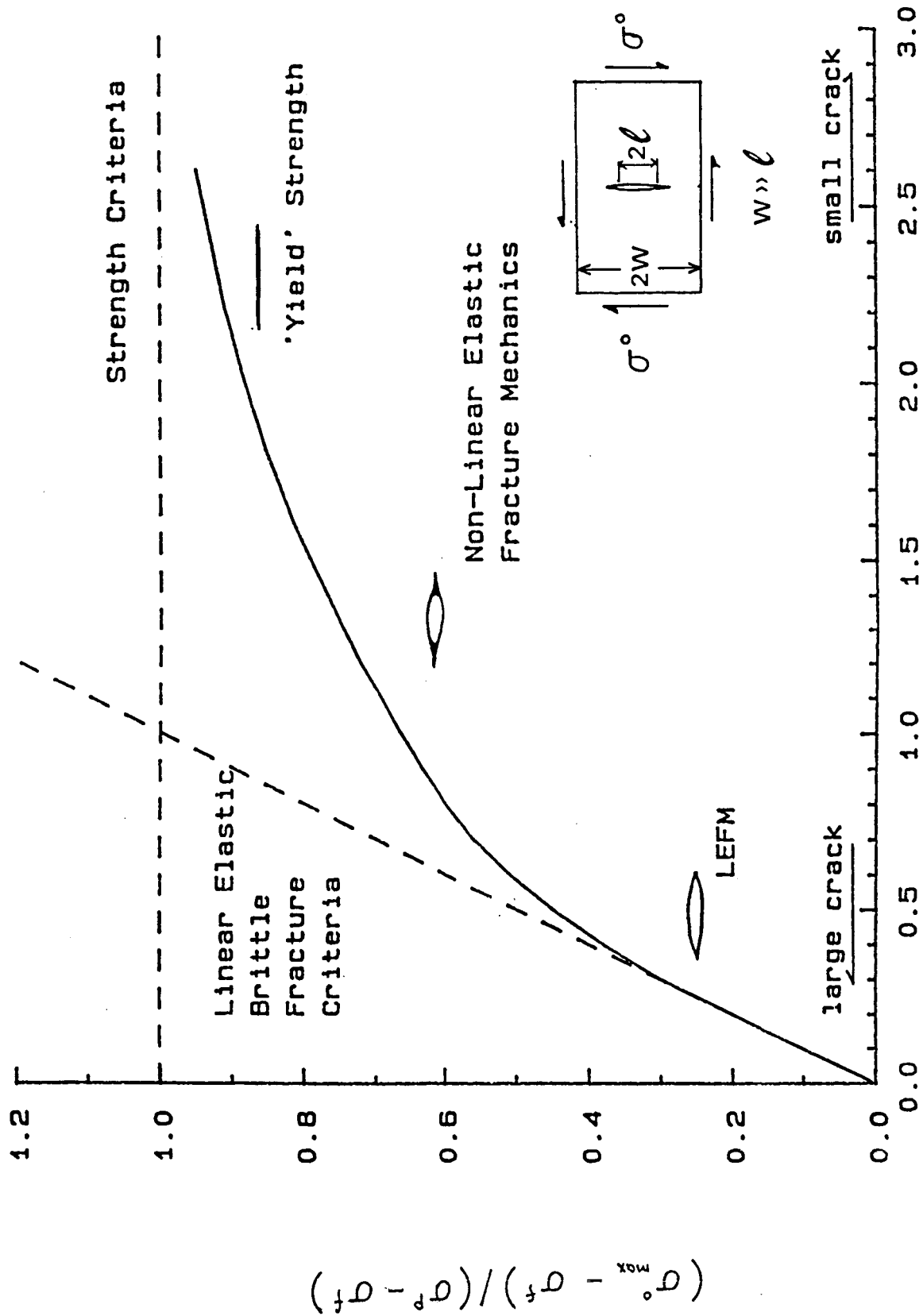


Figure 27

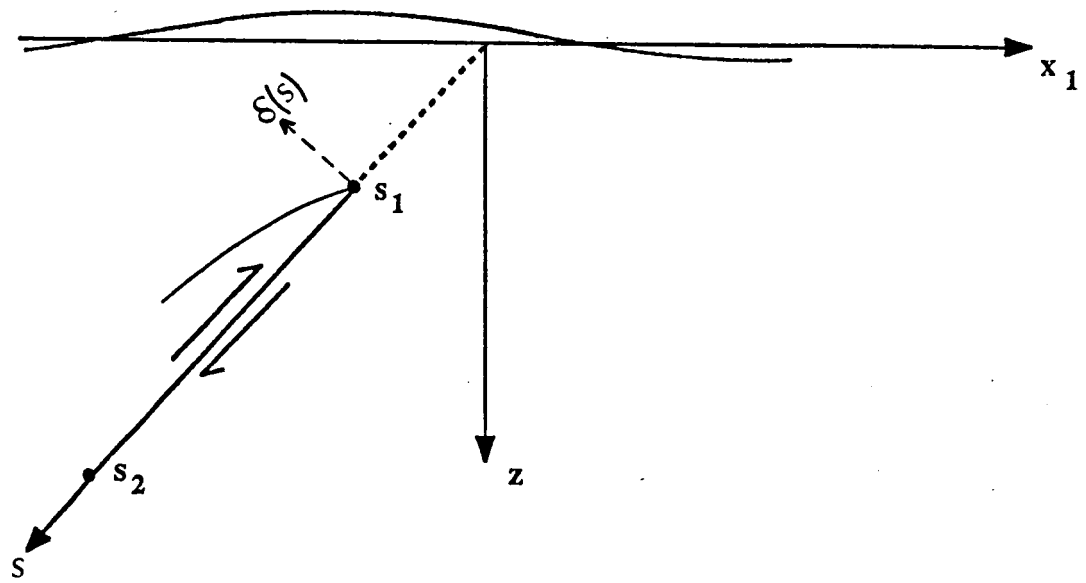


Figure 28

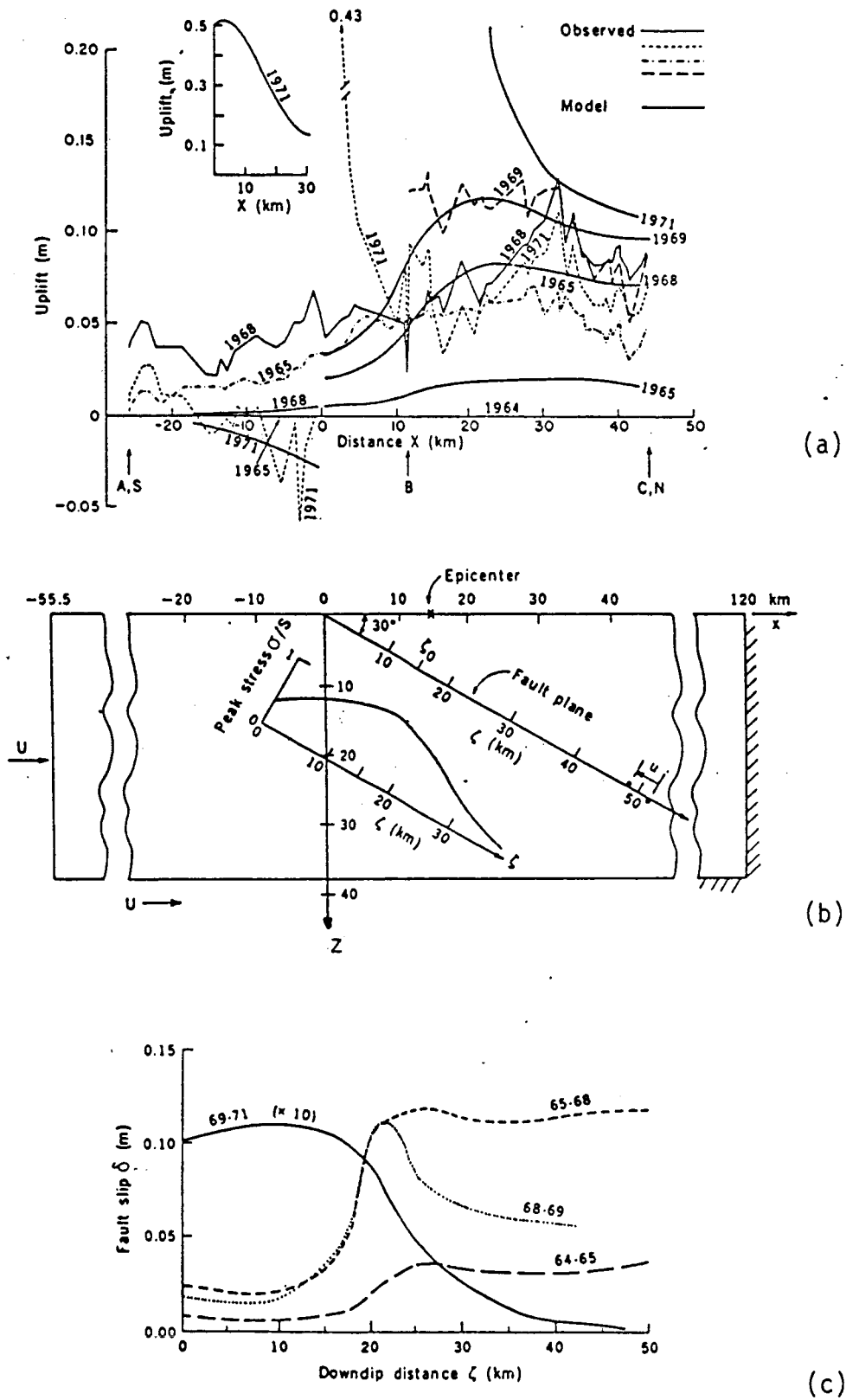


Figure 29

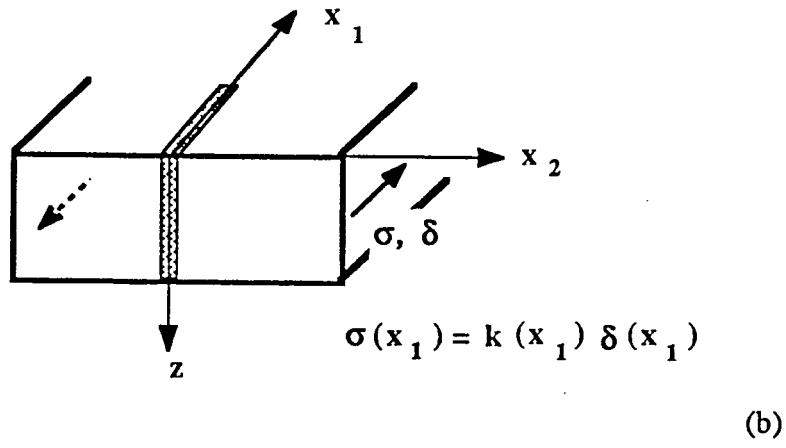
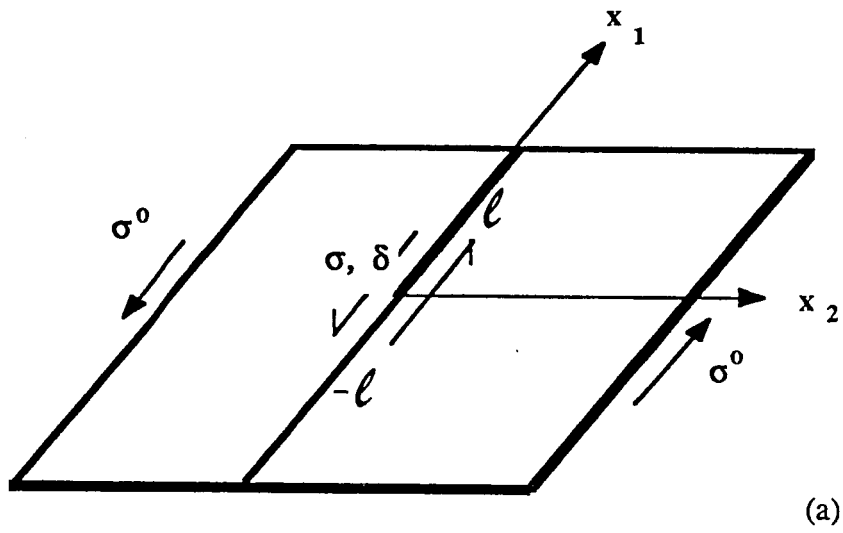


Figure 30

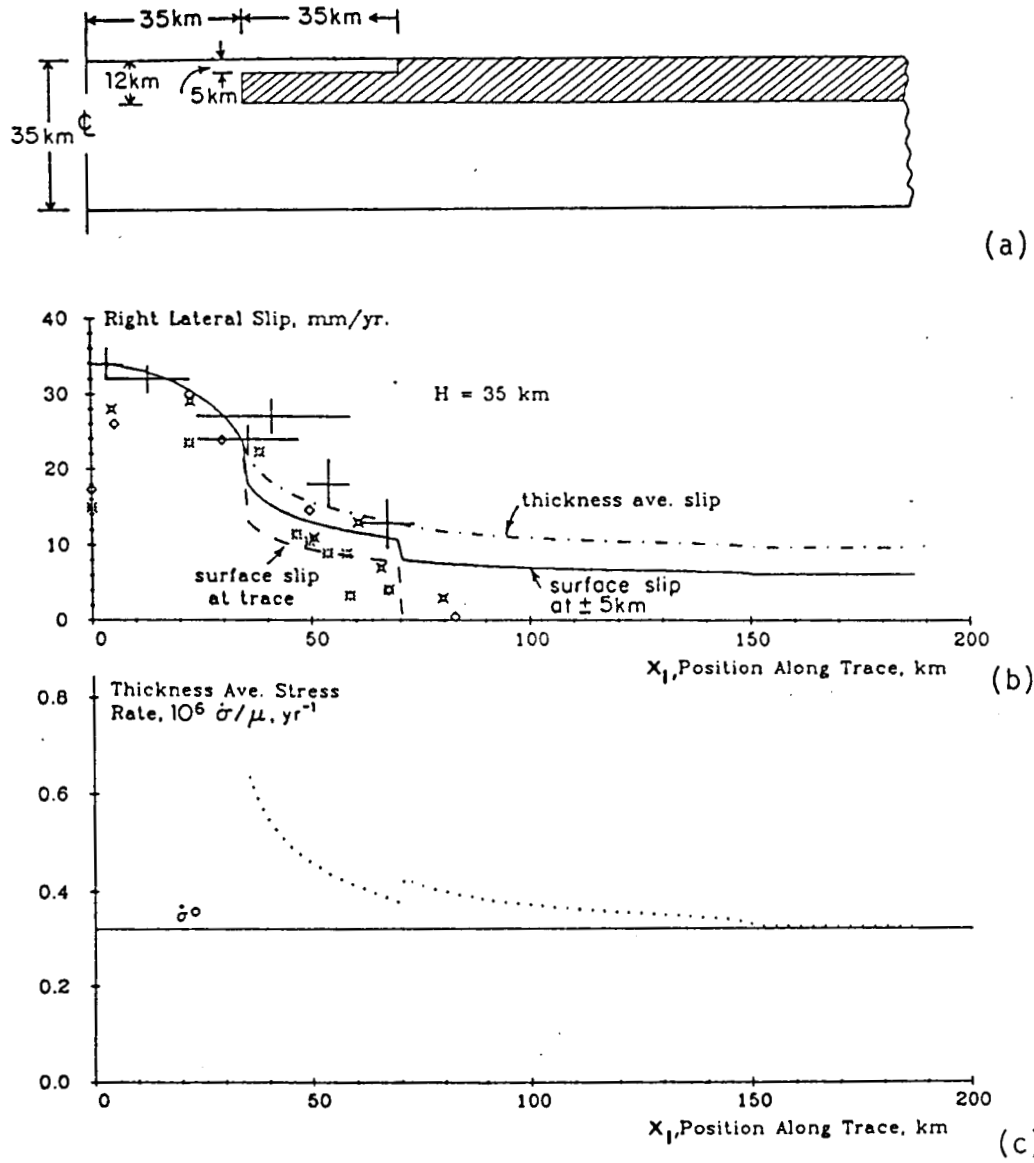


Figure 31

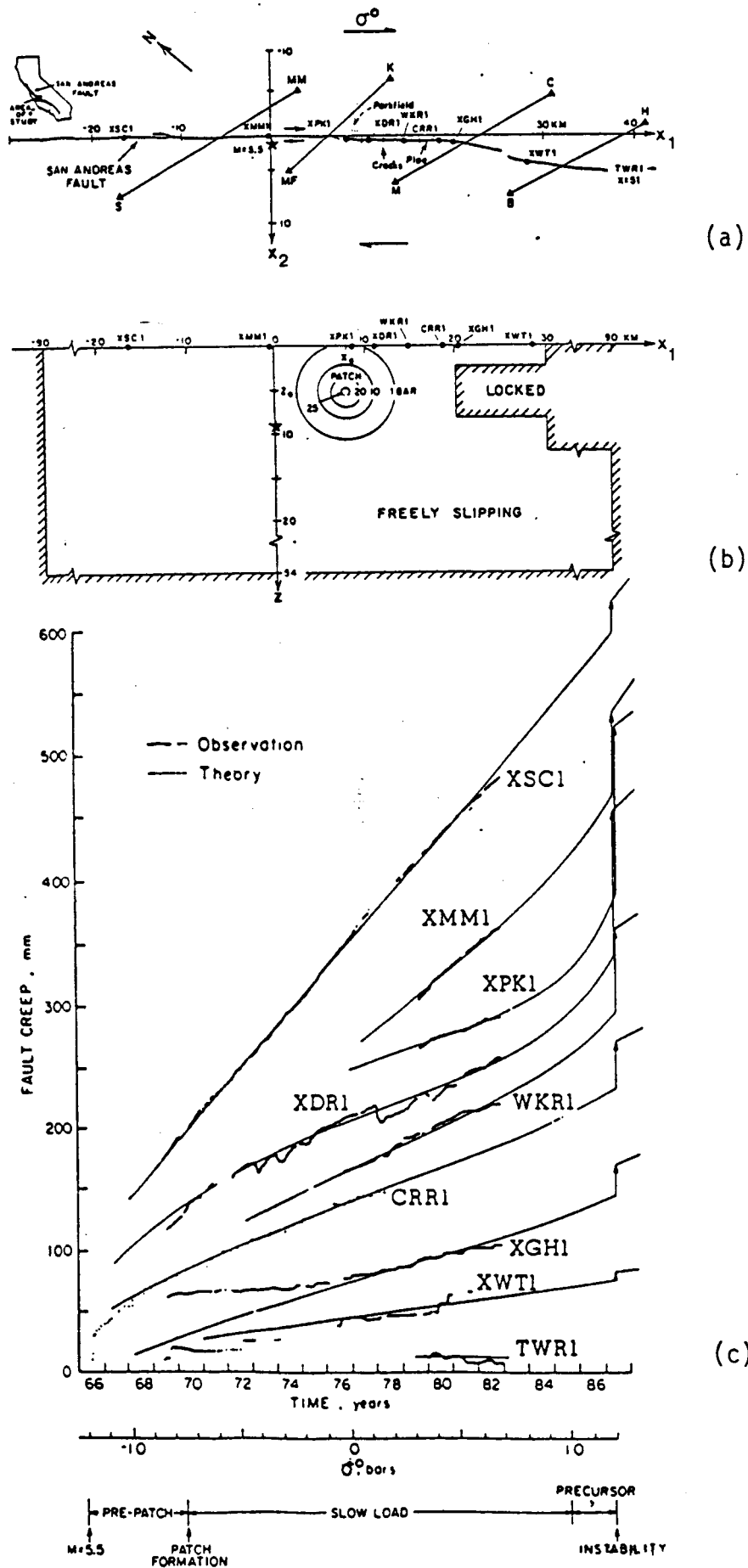


Figure 32

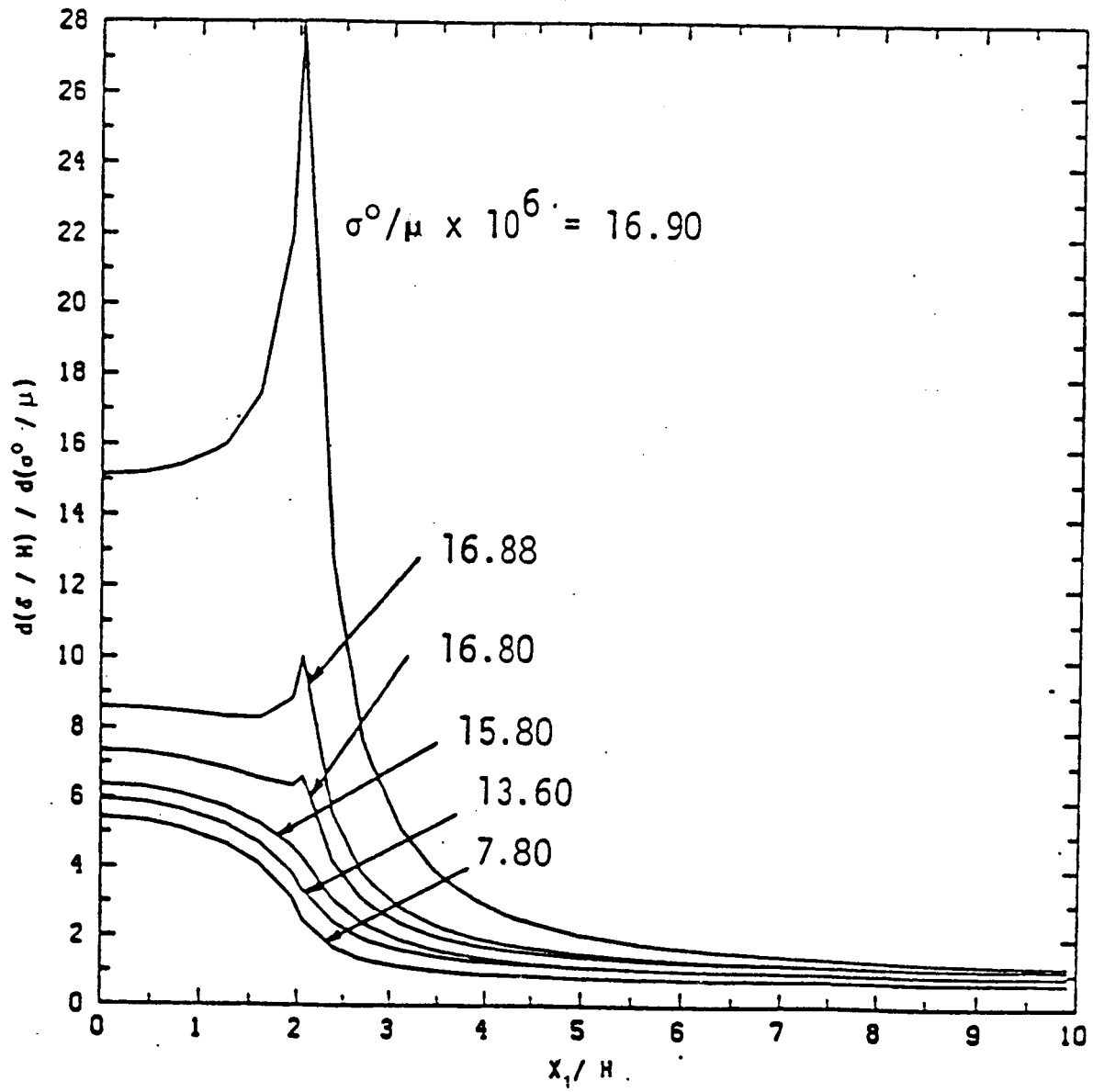


Figure 33